MAX-PLANCK-INSTITUT FÜR QUANTENOPTIK

Multi-particle entanglement on an atomchip

Max Fabian Riedel

MPQ-Report
335

September 2010

Max-Planck-Institut für Quantenoptik
Hans-Kopfermann-Str. 1
D-85748 Garching, Bundesrepublik Deutschland

Multi-particle entanglement on an atom chip

Dissertation
an der Fakultät für Physik
der Ludwig–Maximilians–Universität München

vorgelegt von

Max Fabian Riedel

Max Fabian Riedel

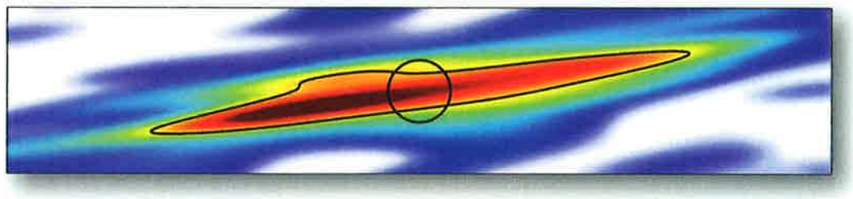

München, September 2010

Meinen Eltern

Erstgutachter: Prof. Dr. Theodor W. Hänsch
Zweitgutachter: Prof. Dr. Philipp Treutlein

Tag der mündlichen Prüfung: 18. November 2010

Zusammenfassung

Die kontrollierte Erzeugung von Verschränkung bildet die Grundlage für den noch jungen Forschungszweig der ,,Quantentechnologien", zu denen neben der Quanten-Metrologie auch die -Simulation und -Informationsverarbeitung zählen. In der Quanten-Metrologie wird untersucht, ob vielteilchenverschränkte Zustände – wie z. B. gequetschte Spinzustände – dazu verwendet werden können, das so genannte Standard-Quantenlimit zu unterschreiten. Dieses hat seinen Ursprung im Quantenrauschen, das jeder Messung an einer endlichen Anzahl unverschränkter Teilchen innewohnt und die Genauigkeit der besten heutigen Atomuhren begrenzt. Atomchips verbinden hervorragende kohärente Kontrolle ultrakalter Atome mit einem kompakten und robusten Versuchsaufbau; sie scheinen daher ideal geeignet für Quanten-Metrologie mit transportablen Atomuhren und -interferometern. Bisher bestand ein Nachteil von Atomchips jedoch darin, dass Techniken zur Kontrolle von zwischenatomaren Wechselwirkungen, die zur Erzeugung von Verschränkung nötig sind, experimentell nicht verfügbar waren.

In der vorliegenden Arbeit beschreibe ich Experimente, mit denen wir zum ersten Mal Vielteilchenverschränkung auf einem Atomchip generieren. Wir erreichen dies, indem wir elastische atomare Kollisionen mit Hilfe eines zustandsabhängigen Potentials kontrollieren. Mit dieser Technik erzeugen wir gequetschte Spinzustände eines zweikomponentigen Bose-Einstein Kondensates. Ich zeige, dass die Verwendung solcher Zustände es ermöglicht, die Genauigkeit einer interferometrischen Messung um 2,5 dB im Vergleich zum Standard-Quantenlimit zu verbessern.

In unserem Chip ist ein coplanarer Wellenleiter integriert, in dessen Umgebung das zustandsabhängige Potential mit Hilfe eines Mikrowellennahfeldes aufgebaut wird. Wenn ein Bose-Einstein Kondensat aus ^{87}Rb-Atomen in dieses Nahfeld gebracht wird, verschieben sich aufgrund des AC-Zeeman-Effektes die atomaren Hyperfein-Energieniveaus. Die starken Feldgradienten können dann dazu verwendet werden, das Minimum einer statischen magnetischen Atomfalle zustandsselektiv zu verschieben und so ein Ensemble von Atomen, die in einer Superposition zweier Hyperfeinzustände präpariert wurden, kohärent aufzuspalten.

Während dieses Prozesses führen nichtlineare atomare Wechselwirkungen zur Entstehung des gequetschten Spinzustandes. Ich analysiere diesen Zustand tomographisch, rekonstruiere seine Wignerfunktion und zeige, dass er eine Verschränkung von mindestens vier Teilchen aufweist.

Gute Übereinstimmung zeigt der Vergleich unserer experimentellen Resultate mit einer dynamischen Multimodensimulation, welche nicht nur die atomare Bewegung und die Dynamik der internen Zustände, sondern auch Teilchenverluste berücksichtigt. Darüber hinaus verwende ich die Ergebnisse, um technische Rauschquellen in unserem Experiment aufzuspüren, welche die Reduktion des Quantenrauschens begrenzen. Ich zeige dadurch Wege auf, wie in zukünftigen Versuchsanordnungen noch stärker gequetschte Spin-Zustände erzeugt werden können.

Da durch unser Verfahren im Prinzip eine sehr starke Verschränkung generiert werden kann, stellt es ein wertvolles Werkzeug für weitere grundlegende Experimente dar. Es kann in einer Vielzahl atomarer Systeme Anwendung finden, insbesondere bei Zustandspaaren, für die keine Feshbach-Resonanz existiert. Technologische Umsetzungen sind in transportablen Atomuhren und hochempfindlichen Interferometern ebenso denkbar wie in der Entwicklung von Quantengattern zur Quanteninformationsverarbeitung auf Atomchips.

Abstract

The controlled generation of entanglement forms the basis for currently emerging 'quantum technologies', such as quantum simulation, computation and metrology. In the field of quantum metrology, multi-particle entangled states, such as spin-squeezed states, are investigated as a means to improve measurement precision beyond the 'standard quantum limit'. This limit arises from the quantum noise inherent in measurements on a finite number of uncorrelated particles and limits today's best atomic clocks. Atom chips combine exquisite coherent control of ultracold atoms with a compact and robust setup, suggesting their use for quantum metrology with portable atomic clocks and interferometers. A severe limitation of atom chips, however, is that techniques to control atomic interactions and to generate entanglement have not been experimentally available so far.

In this thesis, I present experiments where we generate for the first time multi-particle entanglement on an atom chip. We achieve this by controlling elastic collisional interactions with a state-dependent potential. We employ this novel technique to generate spin-squeezed states of a two-component Bose-Einstein condensate and show that they are a useful resource for quantum metrology, as they could be used to improve an interferometric measurement by 2.5 dB over the standard quantum limit.

The state-dependent potential is created with the help of a coplanar microwave guide, which is integrated on our atom chip. In the vicinity of this waveguide a microwave near-field is formed. When a Bose-Einstein condensate of ^{87}Rb is brought into this near-field, the hyperfine energy levels of the atoms are shifted differentially due to the AC Zeeman effect. The strong gradients in the field can be used to state-selectively shift the minimum of a static magnetic atom trap and thus coherently split an ensemble of atoms which have been prepared in a superposition of two internal states.

During this process, nonlinear atomic interactions lead to the formation of a spin-squeezed state. I tomographically analyze the produced state, reconstruct its Wigner function, and deduce that it is at least four-particle entangled.

I compare our results with a dynamical multi-mode simulation which takes not only the atomic motion and internal state dynamics but also particle losses into account and find good agreement. Moreover, I use this comparison to identify technical noise sources in our experiment, which currently limit the achieved amount of squeezing, and make suggestions on how to eliminate them in future experiments.

Our method can in principle create a very large amount of squeezing and entanglement and is applicable to a wide variety of atomic systems, in particular to those for which no convenient Feshbach resonance exists. We envisage the implementation of this technique in portable atomic clocks and interferometers operating beyond the standard quantum limit. Furthermore, it is a valuable tool for experiments on many-body quantum physics and could enable quantum information processing on atom chips.

Contents

The most exciting phrase to hear in science, the one that heralds new discoveries, is not 'Eureka!' but 'That's funny...'

Isaac Asimov

Introduction

Some outstanding technological advances have the power to bring about radical changes in society: think, for example, of the transistor that ushered in the digital age in which we live today. But technological progress is always a result of long years of diverse and thorough scientific research. Naturally, this research has to start with investigating fundamental questions before attention can be directed to possible applications, and in its early stages its impact is difficult to foresee. In 1931, in two seminal papers, Alan H. Wilson applied the band theory to explain the difference between insulators, metals, and semiconductors and to elucidate the mechanism of conduction in semiconductors [1, 2]. The foundation for today's technological marvels was laid only sixteen years later when Bardeen, Brattain, and Shockley made their breakthrough discovery of the transistor [3]. How could any of them have imagined a world where we call our friends on their iPhones to arrange a visit to the newest computer-animated 3 D blockbuster movie?

Fifteen years have passed, since the experimental realization of Bose-Einstein condensation [4, 5, 6] has opened up a new chapter in atomic physics, allowing the study of a broad range of quantum mechanical phenomena on a macroscopic scale. While in the first years fundamental questions, e. g. on long-range phase coherence [7] or vortex formation [8], were investigated, we are currently experiencing a gradual shift of research interest to possible applications of coherent matter waves. Although far be it from me to evoke an impact of cold atoms similar to that of semiconductors, these are clearly exciting times for our field.

Quantum metrology

One direction researchers are pursuing is to find ways to exploit the quantum nature of ultracold atoms. Entanglement – one of the most intriguing concepts of quantum mechanics – lies at the heart of newly emerging technologies such as quantum simulation, computation, and metrology. Particularly, the field of quantum metrology [9, 10] has recently gotten a lot of attention from theorists and experimentalists alike. Here, multi-particle entangled states,

such as spin-squeezed states, are investigated as a means to improve measurement precision beyond the *standard quantum limit* [11]. This limit arises from the quantum noise inherent in measurements on a finite number of uncorrelated particles and limits today's best atomic clocks [12].

The concept of *spin-squeezed states* was introduced in 1993 by Kitagawa and Ueda [13], along with the *one-axis-twisting Hamiltonian*, which can be used to produce them. The name 'spin squeezing' originates from the fact that N two-level atoms can be described by an $N/2$ pseudo-spin, and the fluctuations of one spin component can be reduced at the cost of increasing the fluctuations of an orthogonal one – a concept similar to that of squeezed light [14]. A year later, Wineland et al. [15] introduced a criterion to experimentally identify spin squeezed states as a useful resource for metrology. In 2001, Sørensen et al. [16] proved that the same criterion is also an entanglement witness and showed how squeezing can be generated in Bose-Einstein condensates.

Many experiments on spin squeezing have been performed in a variety of atomic systems since the late nineties [e. g. 17, 18, 19, 20, 21], but until recently, none could satisfy Wineland's criterium. Finally, in 2008, three groups independently produced spin squeezed states in ensembles of neutral atoms and proved that they were a useful resource for quantum metrology. The group around Eugene Polzik performed two different experiments, in one of which entanglement was generated between the atom's nucleus and electrons [22]. In the other, a quantum non-destructive (QND) measurement was used to generate useful spin squeezing on an internal state pair of thermal atoms [23]. At about the same time, a different kind of QND measurement was employed by the group around Vladan Vuletic, attaining a comparable amount of squeezing [24]. The group around Markus Oberthaler, on the other hand, used nonlinear atomic interactions in a BEC, splitting a small condensate with an optical lattice potential. They showed that not only the relative number fluctuations between neighboring wells was reduced below the shot noise limit, but also the phase coherence between the wells remained sufficiently high. Parallel to the work in our group [25], which is presented in this thesis, the Oberthaler group recently also showed useful spin squeezing in a BEC on an internal state pair using a Feshbach resonance and demonstrated a short interferometric measurement using the produced state [26]. Similarly, the Vuletic group measured the lifetime of their squeezed state and operated a rudimentary atomic clock with it [27].

Currently, it is still an open question as to how much spin squeezing can improve actual interferometric measurements, but being still in the beginning, it surely shows great potential. Compared to experiments on squeezed light for example, where it took decades to achieve 10 dB of squeezing,

progress is made much faster. Many groups are setting up new experiments and the recent results have sparked a renewed interest of theorists, making quantum metrology a rapid growing field in atomic physics. The knowledge gained by this research will also be beneficial to related entanglement-based technologies and might even provide new insights into entanglement itself.

Atom chips

Another big area of research is driven by the desire to reduce the complexity, size, and ultimately also the cost of cold atom experiments. Only if this is achieved will such experiments become attractive for real-life applications. The most promising candidates today are so called *atom chips* [28, 29, 30, 31], where magnetic fields produced by microfabricated wires on a substrate are used to trap the atoms. Microfabrication allows for compact, robust and scalable setups with tailor-made trap geometries. The strong atom confinement possible on atom chips facilitates evaporative cooling and thus allows shorter cycle times and relaxed vacuum requirements. Portable and extremely robust atom chip setups that can withstand accelerations of up to 50 g have been demonstrated [32, 33] and key components are now commercially available [34].

Besides these technological advantages, the ability to create complex traps close to the chip surface has also enabled a broad range of new research. Atom chips have been used in experiments on diverse topics such as low-dimensional quantum gases [35], cavity quantum electrodynamics [36], atom-surface interactions [37, 38, 39], and chip-based atomic clocks [40, 41] and interferometers [42, 43]. The high degree of control over quantum states in a compact setup makes atom chips thus perfect candidates for the implementation of quantum technologies. A severe limitation of atom chips, however, is that techniques to control atomic interactions and to generate entanglement have not been experimentally available so far.

This thesis

In this thesis, I present experiments where we generate for the first time multi-particle entanglement on an atom chip. This is achieved by controlling elastic collisional interactions with a state-dependent microwave near-field potential. We employ this technique to generate spin-squeezed states of a two-component Bose-Einstein condensate and show that they could be used to improve an interferometric measurement by 2.5 dB over the standard quantum limit. We also prove that the produced state is at least four particle entangled and reconstruct its Wigner function. Thus, the work described in

this thesis lies at the intersection of the two endeavors of harvesting entanglement for new technologies and bringing cold atom physics closer to real-life applications.

The technological workhorse of our experiments is a coplanar microwave guide which is integrated on our atom chip [44, 45]. In the vicinity of this waveguide a microwave near-field is formed. When a Bose-Einstein condensate of ^{87}Rb is brought into this near-field, the hyperfine energy levels of the atoms are shifted differentially due to the AC Zeeman effect. By tuning the microwave frequency and power, the strong gradients in the field can be used to state-selectively shift the minimum of a static magnetic atom trap. Combined with good control over the internal state of the atoms, this is used to realize a trapped atom interferometer with internal state labeling of the interferometer arms.

While the BEC is split, atomic interactions lead to one-axis-twisting and thus the formation of a spin-squeezed state [25]. The splitting distance and duration are adjusted to achieve the maximum amount of squeezing possible for our chosen experimental trap. We tomographically analyze the produced state, reconstruct its Wigner function, and deduce the amount of entanglement [46].

Since our scheme involves atomic motion as well as internal state dynamics, a simple two-mode model is insufficient to describe it quantitatively. Our theoretical collaborators Alice Sinatra and LI Yun from the Laboratoire Kastler Brossel in Paris have developed a many-body theory [47] taking both motion and internal dynamics as well as particle losses into account and have simulated our experiments. We compare our results with their simulations and find good agreement. Moreover, we use the results to identify technical noise sources in our experiment which currently limit the achieved amount of squeezing.

Our method can in principle create a very large amount of squeezing and entanglement and is applicable to a wide variety of atomic systems, in particular to those for which no convenient Feshbach resonance exists. We envisage the implementation of this technique in portable atomic clocks and interferometers operating beyond the standard quantum limit and it could be directly applied in chip-based atomic clocks which are currently being set up [41]. Furthermore, it is a valuable tool for experiments on many-body quantum physics and could enable quantum information processing on atom chips [48].

The thesis is organized in the following way: In the **first chapter**, I outline the theoretical concepts behind the tools which we use to state-selectively

manipulate atoms on the chip. This includes the interaction of atoms with static and oscillating magnetic fields, the standard methods to magnetically trap atoms with microfabricated wires, and some theory on two component Bose-Einstein condensates.

The **second chapter** covers the theory of atomic clocks and spin squeezing. I start with the basic working principles of atomic interferometers and clocks and derive the standard quantum limit. I then turn to the 'one-axis-twisting scheme' in the two mode model and how we evolve coherent spin states into spin-squeezed states using the state-selective potentials to tune the wave function overlap of our two states. Finally, I briefly cover our collaborator's advanced theory which takes into account motion and internal state dynamics as well as atom losses and technical noise.

Our experimental setup is described in the **third chapter**, with a special emphasis on the imaging system which enables the high atom number resolution needed for the detection of fluctuations at and below the standard quantum limit.

In the **fourth chapter**, I present our results and compare them with theoretical predictions. From this comparison, combined with detailed measurements of technical noise in our experiment, I derive modifications of our setup which should be implemented to improve future measurements.

Finally, I provide an **outlook** on future experiments possible with our setup and our technique in general.

Publications of thesis work

- *Atom-chip-based generation of multi-particle entanglement for quantum metrology.*
  M. F. Riedel, P. Böhi, Y. Li, A. Sinatra,
  T. W. Hänsch, and P. Treutlein,
  Nature **464**, 1170-1173 (2010).

- *Coherent manipulation of Bose-Einstein condensates with state-dependent microwave potentials on an atom chip.*
  P. Böhi, M. F. Riedel, J. Hoffrogge, J. Reichel,
  T. W. Hänsch, and P. Treutlein,
  Nature Physics **5**, 592-597 (2009)

- *Imaging of microwave fields using ultracold atoms.*
  P. Böhi, M. F. Riedel, T. W. Hänsch, and P. Treutlein,
  Applied Physics Letters **97**, 051101 (2010)

- *Method and device for sensing microwave magnetic field polarization components.*
  P. Böhi, M. F. Riedel, T. W. Hänsch, and P. Treutlein,
  U. S. patent pending

Chapter 1

Bose-Einstein condensates on atom chips

This chapter covers the basic theoretical concepts lying behind the techniques we use to manipulate ultracold atoms in our experiment. I start with the interaction between atoms and electromagnetic fields, then briefly cover the basic principles of the atom chip, and finally discuss Bose-Einstein condensation of a two-component gas.

1.1 Atom-field interaction

In our experiment, we use light, static magnetic fields, and high frequency oscillating magnetic fields to manipulate the atoms. A solid understanding of how the atom interacts with external electromagnetic fields is therefore required. In this section, I provide a basic outline of the theory of atom-field interaction. For a detailed derivation, see [49] and references therein.

As in most experiments on atom chips, the atomic species used in our experiment is ^{87}Rb in the $5S_{1/2}$ electronic ground state. For the scope of this thesis, we are mostly interested in the description of an atom in a static magnetic field $\mathbf{B}$ and a microwave field

$$\mathbf{B}_{\mathrm{mw}}(t) = \frac{B_{\mathrm{mw}}}{2}(\boldsymbol{\epsilon} e^{-i\omega t} + \boldsymbol{\epsilon}^* e^{i\omega t}). \tag{1.1}$$

The electric part of the microwave field only shifts the energy of the complete electronic ground state which results in a constant offset for all sub levels and can be neglected for our purpose. The Hamiltonian describing the coupled

atom-field system is

$$\begin{aligned} \hat{H} &= \hat{H}_{\mathrm{BR}} + \hat{H}_{\mathrm{mw}} \\ \text{with} \quad \hat{H}_{\mathrm{BR}} &= A_{\mathrm{hfs}}\,\hat{\mathbf{I}}\cdot\hat{\mathbf{J}} + \mu_B(g_J\hat{\mathbf{J}} + g_I\hat{\mathbf{I}})\cdot\mathbf{B} \\ \hat{H}_{\mathrm{mw}} &= \mu_B(g_J\hat{\mathbf{J}} + g_I\hat{\mathbf{I}})\cdot\hat{\mathbf{B}}_{\mathrm{mw}} + \hbar\omega(\hat{a}^\dagger\hat{a} + \frac{1}{2}), \end{aligned} \tag{1.2}$$

where μ_B is the Bohr magneton, $\hat{\mathbf{J}}$ and $\hat{\mathbf{I}}$ are the electron's and the nucleus' angular momentum operators, respectively, $g_J \approx 2$ and $g_I \approx -1\cdot 10^{-3}$ their Landé factors, $\hat{\mathbf{B}}_{\mathrm{mw}} = \sqrt{\frac{\hbar\omega\mu_0}{2V}}(\epsilon\hat{a} + \epsilon^*\hat{a}^\dagger)$ is the quantized microwave field operator, and $\hat{a}^\dagger$ ($\hat{a}$) is the creation (annihilation) operator of the microwave field mode of frequency ω in a quantization volume V. $\hat{H}_{\mathrm{BR}}$ is the *Breit-Rabi* Hamiltonian for an atom in a static magnetic field and $\hat{H}_{\mathrm{mw}}$ describes the interaction with the microwave. In the following, I will cover the individual terms in more detail.

1.1.1 Hyperfine structure of ^{87}Rb

Without any external field ($\hat{H} = A_{\mathrm{hfs}}\,\hat{\mathbf{I}}\cdot\hat{\mathbf{J}}$), the atom can be described in the basis of Eigenstates $|F, m_F\rangle$ of $\hat{\mathbf{F}}^2$ and $\hat{F}_z$, where $\hat{\mathbf{F}} = \hat{\mathbf{J}} + \hat{\mathbf{I}}$ is the total angular momentum of the atom. The nuclear spin of $I = 3/2$ and the angular momentum $J = \frac{1}{2}$ of the single valence shell electron result in two hyperfine manifolds $F = 1$ and $F = 2$ which are separated by $E_{\mathrm{hfs}} = 2A_{\mathrm{hfs}} = \hbar\omega_{\mathrm{hfs}} = h\cdot 6.834\,682\,611\,\mathrm{GHz}$ [50].

The influence of a weak magnetic field $\mathbf{B}$ on the atom can be treated pertubatively. It results in an energy shift of the hyperfine states, the first order magnetic Zeeman shift

$$E_{\mathrm{Z}} = \mu_B m_F g_F, \tag{1.3}$$

where g_F is the total angular momentum Landé factor. The Zeeman shift has the same magnitude but opposite sign for the two hyperfine manifolds with $g_{F=2} \approx \frac{1}{2}$ and $g_{F=1} \approx -\frac{1}{2}$. It leads to a splitting of adjacent m_F levels by 0.7 MHz/G. The resulting term scheme of ^{87}Rb in a weak magnetic field is shown in figure 1.1.

1.1.2 Breit Rabi formula

For high precision measurements, such as spectroscopy or interferometry, the first order Zeeman shift is not sufficient to describe the states' nonlinear energy dependence in a magnetic field and we have to return to the Breit-Rabi Hamiltonian of equation 1.2. It can be analytically solved for $J = \frac{1}{2}$

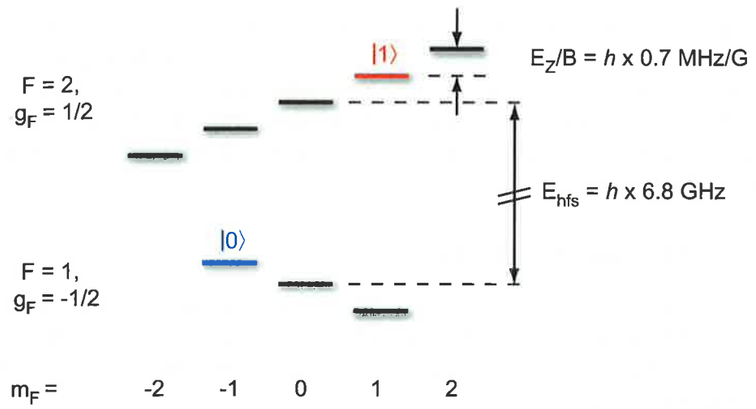

Figure 1.1: Term scheme of ^{87}Rb. The electronic ground state of ^{87}Rb has two hyperfine levels with $F = 1$ and $F = 2$ separated by $E_{\mathrm{hfs}} = h\cdot 6.8\,\mathrm{GHz}$. In a weak magnetic field $\mathbf{B}$ the m_F-sublevels are split by the Zeeman energy $E_{\mathrm{Z}}/B = h\cdot 0.7\,\mathrm{MHz/G}$. The clock-states $|0\rangle$ and $|1\rangle$ are indicated.

and arbitrary I and B. We will restrict ourselves to small magnetic fields, so that the Breit-Rabi Eigenstates are nearly identical to the unperturbed states $|F, m_F\rangle$. In the following, $|F, m_F\rangle$ will thus be used to label the Eigenstates of H_{BR}. Diagonalizing H_{BR} yields the Eigenenergies given by the Breit-Rabi formula [50, 51]

$$\begin{aligned} E_{F,m_F} &= -\frac{E_{\mathrm{hfs}}}{8} + \mu_B g_I m_F B \pm \frac{E_{\mathrm{hfs}}}{2}\left(1 + m_F\xi + \xi^2\right)^{1/2}, \\ \text{where} \quad \xi &= \frac{\mu_B(g_J - g_I)B}{E_{\mathrm{hfs}}}. \end{aligned} \tag{1.4}$$

The + sign is for the $F = 2$ manifold whereas the − sign is for the $F = 1$ manifold. Neglecting the coupling of the nucleus to the magnetic field (because $|\frac{g_I}{g_J}| < 10^{-3}$) and expanding equation 1.4 to first order recovers the Zeeman shift of equation 1.3 with $E_{F,m_F} = -\frac{E_{\mathrm{hfs}}}{8} \pm \frac{E_{\mathrm{hfs}}}{2} + E_Z$.

The Breit Rabi formula predicts a small differential energy shift between the magnetically trapable states

$$\begin{aligned} |0\rangle &\equiv |F = 1, m_F = -1\rangle \\ \text{and} \quad |1\rangle &\equiv |F = 2, m_F = +1\rangle, \end{aligned} \tag{1.5}$$

which vanishes at a magnetic field of $B_\diamond = 3.229\,\mathrm{G}$ and scales as [52]

$$E_{|1\rangle} - E_{|0\rangle} = h\cdot 431\frac{\mathrm{Hz}}{\mathrm{G}^2}(B - B_\diamond)^2 + E_{\mathrm{BR}}, \tag{1.6}$$

where $E_{\mathrm{BR}} = 6.834\,678\,114\,\mathrm{GHz}$. As a consequence, a coherent superposition of states $|0\rangle$ and $|1\rangle$ can be very robust against magnetic field fluctuations. Coherence times of up to one minute have been observed [41] which makes $|0\rangle$ and $|1\rangle$ ideally suited for atomic clocks on a chip [40, 49, 41, 53] or for quantum information processing [48]. In this thesis, I will refer to these states as the two *clock states*.

1.1.3 Microwave fields

The interaction of the atom with a microwave magnetic field is described by $\hat{H}_{\mathrm{mw}}$. The first term in $\hat{H}_{\mathrm{mw}}$ describes the coupling of the atom to the microwave field whereas the second term describes the energy of the field in second quantization.

For an approximate solution (for details, see chapter 5.1 of [49]), we consider only the first order Zeeman shift and again neglect the coupling of the nucleus to the field. Furthermore, because $(\mu_B B_{\mathrm{mw}}, \hbar\Delta) \ll \hbar\omega_{\mathrm{hfs}}$, with $\Delta \equiv \omega - \omega_{\mathrm{hfs}}$, we make the rotating wave approximation and get

$$\begin{aligned}\hat{H} &= \sum_{m_2}\left(-\frac{1}{2}\hbar\Delta + \hbar\omega_L m_2\right)|2,m_2\rangle\langle 2,m_2| \\ &+ \sum_{m_1}\left(\frac{1}{2}\hbar\Delta - \hbar\omega_L m_1\right)|1,m_1\rangle\langle 1,m_1| \\ &+ \sum_{m_1,m_2}\left(\frac{1}{2}\hbar\Omega^{2,m_2}_{1,m_1}|2,m_2\rangle\langle 1,m_1| + c.c.\right), \\ \text{with}\quad \Omega^{2,m_2}_{1,m_1} &= \frac{2\mu_B}{\hbar}B_{\mathrm{mw}}\langle 2,m_2|\boldsymbol{\epsilon}\cdot\hat{\mathbf{J}}|1,m_1\rangle. \end{aligned} \tag{1.7}$$

The first two sums describe the *bare states* of an uncoupled system which are identical to the atomic Eigenstates $|F,m_F\rangle$ but energetically shifted because the field energy is taken into account. Here, $\omega_L = \mu_B|g_F|B/\hbar$ is the Larmor frequency.

The last sum describes the coupling of the atom to the field. Ω^{2,m_2}_{1,m_1} is the *Rabi frequency* for a transition coupling the states $|1,m_1\rangle$ and $|2,m_2\rangle$ and a measure for the strength of this transition. The angular momentum matrix elements $\langle 2,m_2|\boldsymbol{\epsilon}\cdot\hat{\mathbf{J}}|1,m_1\rangle$ are generally complex valued and can be calculated with the help of Clebsch-Gordan coefficients (see appendix B).

Dressed states

Diagonalizing the complete Hamiltonian $\hat{H} = \hat{H}_{\mathrm{BR}} + \hat{H}_{\mathrm{mw}}$ one obtains the new Eigenstates of the coupled system, the so called *dressed states* $|K\rangle$. In

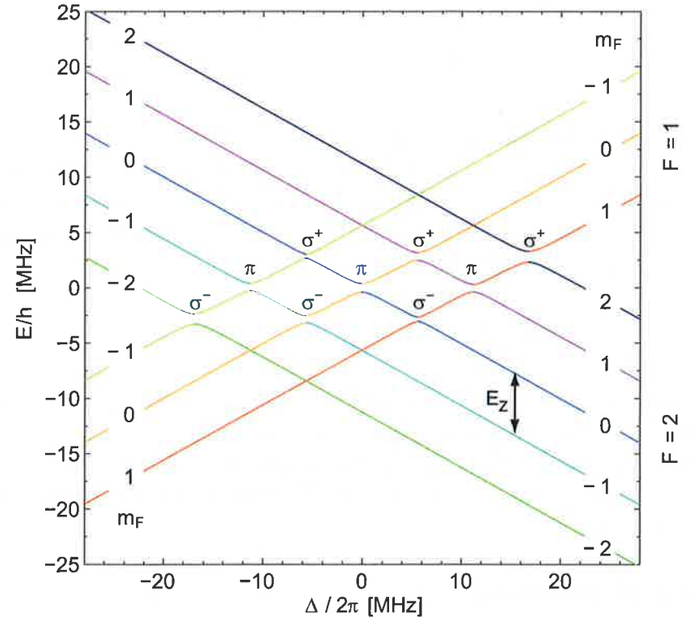

Figure 1.2: Dressed state energies. Eigenenergies E_K of the dressed states as a function of the detuning Δ, calculated by diagonalizing the Hamiltonian of equation 1.7 for $B = 8\,\mathrm{G}$, $B_{\mathrm{mw}} = 1\,\mathrm{G}$ and $\boldsymbol{\epsilon} = \frac{1}{\sqrt{3}}(1,1,1)$. Line colors indicate the dominating bare state $|F,m_F\rangle$ of each dressed state. The avoided crossings are labeled with their associated microwave polarization component. Figure adapted from [49].

figure 1.2 the Eigenenergies E_K are plotted as a function of the microwave detuning Δ for a microwave field with equally strong polarizations. The dressed states can be expressed as a linear combination of the bare states $|F,m_F\rangle$ and the color indicates which bare state is dominant in each dressed state for a given detuning.

Far away from a resonance, each dressed state is nearly identical to one of the bare states. An anticrossing between two states occurs if the corresponding Rabi frequency Ω^{2,m_2}_{1,m_1} is non vanishing, i. e. if $(m_2 - m_1) = (1,-1,0)$ for a (σ^+,σ^-,π) polarized microwave. Near such an anticrossing, the dressed states are essentially a linear combination of the involved bare states and the description can be reduced to that of a two-level system. The energy

splitting between the states is then given by

$$E_+ - E_- \approx \hbar\sqrt{|\Omega_{1,m_1}^{2,m_2}|^2 + |\Delta_{1,m_1}^{2,m_2}|^2}, \tag{1.8}$$

where $+$ $(-)$ denotes the upper (lower state).

By smoothly turning on a microwave far off resonance and then sweeping its frequency slowly over the resonance one can transfer one bare state into another with close to 100% efficiency. This technique is called *rapid adiabatic passage* and the adiabaticity criterion is [54]

$$\frac{1}{2}|\dot{\Omega}\Delta - \Omega\dot{\Delta}| \ll (\Omega^2 + \Delta^2)^{3/2}, \tag{1.9}$$

where I used a simplified notation $\Omega \equiv \Omega_{1,m_1}^{2,m_2}$ and $\Delta \equiv \Delta_{1,m_1}^{2,m_2}$, and the dot symbolizes the derivative with respect to time.

On the other hand, if the microwave is switched on abruptly close to the resonance the atom undergoes *Rabi oscillations*, which are treated in more detail in section 2.1.1.

Far detuned microwave

If the microwave is far detuned from all transitions, $|\Delta_{1,m_1}^{2,m_2}| \gg |\Omega_{1,m_1}^{2,m_2}|$ for all m_1, m_2, the microwave field can be treated pertubatively. The dressed states are nearly identical to the unperturbed states and their energies are AC Zeeman shifted by an Energy E_{mw}. For the $F = 1$ manifold

$$|K\rangle \approx |1, m_1\rangle \mp \sum_{m_2} \frac{\Omega_{1,m_1}^{2,m_2}}{2\Delta_{1,m_1}^{2,m_2}}|2, m_2\rangle, \qquad E_{\mathrm{mw}}^{1,m_1} = \hbar\sum_{m_2} \frac{|\Omega_{1,m_1}^{2,m_2}|^2}{4\Delta_{1,m_1}^{2,m_2}}, \tag{1.10}$$

while for the $F = 2$ manifold

$$|K\rangle \approx \pm|2, m_2\rangle + \sum_{m_1} \frac{\Omega_{1,m_1}^{2,m_2}}{2\Delta_{1,m_1}^{2,m_2}}|1, m_1\rangle, \qquad E_{\mathrm{mw}}^{2,m_2} = -\hbar\sum_{m_1} \frac{|\Omega_{1,m_1}^{2,m_2}|^2}{4\Delta_{1,m_1}^{2,m_2}}, \tag{1.11}$$

where the top sign is for all $\Delta_{1,m_1}^{2,m_2} < 0$ and the bottom sign for all $\Delta_{1,m_1}^{2,m_2} > 0$. The dressed states have small admixtures of other states which are connected to them by microwave transitions and the total energy shift of a state is the sum of the individual shifts caused by these transitions. For an intuitive understanding of the experiments described in this thesis, this level of approximation is usually sufficient. For a quantitative analysis, as required for the simulation of our potentials, however, we numerically solve the dressed state Hamiltonian 1.7.

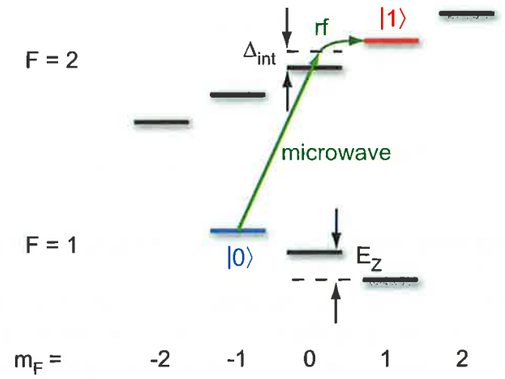

Figure 1.3: Two-photon drive. The states $|0\rangle$ and $|1\rangle$ can be coupled via a two-photon transition, consisting of a microwave and a radio frequency oscillating magnetic field. The microwave is detuned by Δ_{int} from the transition $|0\rangle \leftrightarrow |2, 0\rangle$.

By choosing the microwave frequency and polarization appropriately, the energy shifts for states $|0\rangle$ and $|1\rangle$ can be different or even opposing. For example, for a highly blue detuned microwave ($\Delta \gg 0$), state $|0\rangle$ will be shifted upward in energy while state $|1\rangle$ will be shifted downward. Combined with strong microwave intensity gradients this leads to a state selective potential as described in section 1.3.

1.1.4 Two-photon transition

The two states $|0\rangle$ and $|1\rangle$ can be coupled using a combined microwave and radio frequency two-photon transition (see figure 1.3). It consists of a microwave of frequency ω_{mw}, blue detuned by Δ_{int} with respect to the transition $|0\rangle \leftrightarrow |2, 0\rangle$ and a radio wave of frequency ω_{rf} such that $\omega_{\mathrm{mw}} + \omega_{\mathrm{rf}} = (E_{|1\rangle} - E_{|0\rangle} + E_{\mathrm{ls}})/\hbar$. Here, $E_{|0\rangle}$ and $E_{|1\rangle}$ are the energies of the unperturbed states and E_{ls} takes into account level shifts induced by the off-resonant microwave of the two-photon drive described by equations 1.10 and 1.11. Level shifts due to the linearly polarized radio frequency radiation are common mode for $|0\rangle$ and $|1\rangle$ and are neglected in the following [49].

For $(|\Omega_{\mathrm{mw}}|^2, |\Omega_{\mathrm{rf}}|^2) \ll \Delta_{\mathrm{int}}^2$, the population of the intermediate state $|2, 0\rangle$ is small and the three-level system can be treated as an effective two-level

system with the two-photon Rabi frequency [55]

$$\Omega_{2p} = \frac{\Omega_{\mathrm{mw}}\Omega_{\mathrm{rf}}}{2\Delta_{\mathrm{int}}}, \tag{1.12}$$

with $\Omega_{\mathrm{mw}} \equiv \Omega^{2,0}_{1,-1} = \sqrt{\frac{1}{8}}\frac{\mu_B}{\hbar}B_{\mathrm{mw}}$ and $\Omega_{\mathrm{rf}} = \sqrt{\frac{3}{8}}\frac{\mu_B}{\hbar}B_{\mathrm{rf}}$.

1.2 The atom chip – a quantum lab on a chip

The achievements of cooling and trapping of neutral atoms [56, 57], which culminated in the generation of Bose-Einstein condensates (BECs) of dilute atomic gases [4, 5, 6], have given us – more than half a century after the formulation of quantum mechanics – a powerful tool to study the very basis of this theory. Things like the particle in a box, pure quantum states, or the quantum harmonic oscillator are no longer only theoretical concepts but can be investigated experimentally. Moreover, we can now engineer complex quantum systems in simplified and controlled environments to gain an understanding of few- and many-body physics which could not have been reached by pure observation of natural phenomena.

Standard BEC apparatus are highly complex machines which fill up complete laboratories, often require more than one person to run them, and typically produce BECs at a rate of one per minute or less. The desire to simplify and speed up cold atom experiments led to the development of atom chips [28, 29, 30, 31]. On atom chips, the magnetic fields used to trap atoms are created by current carrying micro-fabricated wires (less commonly also by structured permanent magnetic materials on the chip [58, 59, 60] or superconducting wires [61]) instead of large current coils. Thus, more versatile traps can be realized. Trap frequencies of up to several kHz increase thermalization rates significantly and therefore shorten the time needed for evaporative cooling from minutes to seconds [33]. Besides enabling high repetition rates, the requirements on ultra high vacuum are thus greatly reduced so that experiments can be done in compact and robust [32] single-chamber setups.

In addition to these technical advantages, atom chips also open up new areas of physics. Trap geometries can be varied from nearly isotropic to very elongated traps, which enables the study of ultra-cold atoms in one dimension [35, 62]. The traps can be positioned with a few nanometer precision [39], even close to the chip surface [37]. The atoms can then be used as highly sensitive, high resolution probes for weak electromagnetic fields [63, 64] or surface forces [65, 37, 39]. Also, more complex trap geometries such as double-wells [66, 43], magnetic lattices [60], conveyor belts [67, 68],

atom guides, beam splitters [69, 66, 43] and state-selective beam splitters [44] for atom optics and atom interferometry have been realized, using dc [70], radio frequency [43], and microwave frequency [44] currents on the chip. In addition to the supreme control over external degrees of freedom, the internal state of the atoms can be manipulated with coherence times of up to a minute [40, 41]. Recently, single atom preparation and detection [71] using an integrated fiber cavity has been demonstrated, and in this thesis, a method to produce entanglement on a chip [25] is presented.

In recent years, we have entered a new phase in ultra-cold atoms research. Experiments are not anymore only aimed at gaining deeper insight into fundamental physics, but also at developing new technologies which harness the peculiar features of quantum mechanics for more precise measurements, faster computation, more secure communication, and the simulation of quantum effects in other physical systems. The wide range of sophisticated methods to manipulate atoms, combined with the scalability of micro-fabrication processes, and their simple, compact, and robust experimental setups makes atom chips ideal candidates for the implementation of such quantum technologies. Over the years, atom chips have developed from technological playgrounds to full grown quantum labs.

1.2.1 Magnetic trapping on atom chips

The basic building block of our (and almost all other atom chip experiments) is the wire trap, which is described in detail in several atom chip reviews [28, 29, 30, 31] or in [72] and [49]. In the following, I will briefly outline the general methods to trap atoms with on-chip wires. I assume that the reader is familiar with the basic principles of magnetic trapping of neutral atoms (for a review, see for example [56]).

In short, in a magnetic field $\mathbf{B}(\mathbf{r})$, an atom with magnetic moment $\mu = \mu_B g_F m_F$ experiences a Zeeman shift $E_Z = \mu_B g_F m_F B$ (see eq. (1.3)). A spatially varying field thus exerts a force $\mathbf{F}_Z(\mathbf{r}) = -\nabla E_Z(\mathbf{r})$ on the atom which then can be trapped in a magnetic field minimum if it is a so called *low field seeker*, i. e. if $g_F m_F > 0$.

The wire guide

Consider an infinitely long, infinitely thin wire which carries a current I (figure 1.4). The current produces a circular magnetic field around the wire which falls off radially like $1/r$. Applying a homogeneous magnetic field $\mathbf{B}_e$ perpendicular to the wire leads to a line parallel to the wire with vanishing

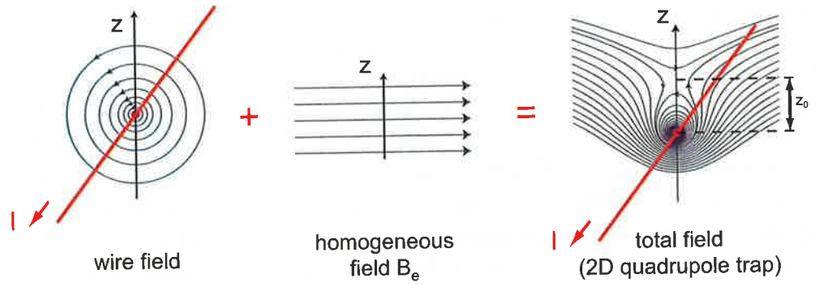

Figure 1.4: Principle of the wire guide. The superposition of a circular magnetic field around a current carrying wire and a homogeneous magnetic field leads to a magnetic field minimum above the wire. Figure adapted from [28].

magnetic field at a distance

$$z_0 = \frac{\mu_0 I}{2\pi B_e}. \tag{1.13}$$

The magnetic field around the minimum can be approximated by a two-dimensional quadrupole with gradient

$$B' = -\frac{\mu_0 I}{2\pi z_0^2} = -\frac{2\pi B_e^2}{\mu_0 I}. \tag{1.14}$$

Thus, by varying I and B_e, one can in principle produce atom guides with any desired transversal confinement at any desired distance from the wire. On an atom chip, the wire is usually lithographically patterned on the substrate and has a finite width w and thickness d which limit the maximum current that can be applied due to resistive heating. As long as $z_0 \gg w, d$ the field is well approximated by that of an infinitely thin wire, but more complicated analytical formulas, which take into account the actual wire dimensions, exist for traps close to the surface [72]. To close the guide in its axial direction and transform it into a three dimensional trap one either bends the wire or crosses it with a second wire to form a so called *dimple trap*.

'U'- and 'Z'-shaped wires

When bending the wire to a 'U'-shape (figure 1.5) the fields of the lead wires compensate each other in the trap center and form a quadrupole field along the x-direction. The uncompensated component in the z-direction results in a small shift of the trap along y. The vanishing field in the trap center can

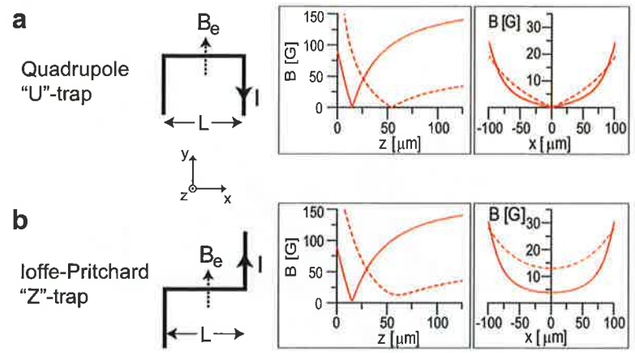

Figure 1.5: Quadrupole and Ioffe-Pritchard wire trap. **a**, Bending the wire in a 'U'-shape results in a quadrupole trap with vanishing magnetic field in the trap center. **b**, Bending the wire in a 'Z'-shape leads to a Ioffe-Pritchard trap with finite magnetic field in the center. Here, length $L = 250\,\mu$m, wire-width $w = 50\mu$m, current $I = 2\,$A, and homogeneous magnetic field $B_e = 54\,$G (dashed lines) and $162\,$G (solid lines). Figure adapted from [30].

lead to atom losses due to Majorana spin flips (see section 1.4.3) which is why quadrupole traps are only used for relatively hot atom clouds where the atoms spend only very little time in the trap center. Bending the wire in a 'Z'-shape solves this problem and a Ioffe-Pritchard trap [73] is formed with a finite magnetic field in the center along x.

Dimple trap

A dimple trap essentially results from crossing two magnetic guides (figure 1.6). The first guide along x with a wire carrying a current I_0 and a field $B_{e,y}$ determines the distance of the trap from the chip surface $z_0 \approx \frac{\mu_0 I_0}{2\pi B_{e,y}}$ and the magnetic field gradient B' in the yz-plane. The second guide, with a current $I_1 \ll I_0$ and a magnetic field $B_{e,x}$, raises the field in the trap center and determines the axial confinement. The resulting trap is of Ioffe-Pritchard type with [72]

$$\mathbf{B} = B_0 \begin{pmatrix} 1 \\ 0 \\ 0 \end{pmatrix} + B' \begin{pmatrix} 0 \\ -y \\ z \end{pmatrix} + \frac{B''}{2} \begin{pmatrix} x^2 + (y^2 + z^2)/2 \\ -xy \\ -xz \end{pmatrix} \tag{1.15}$$

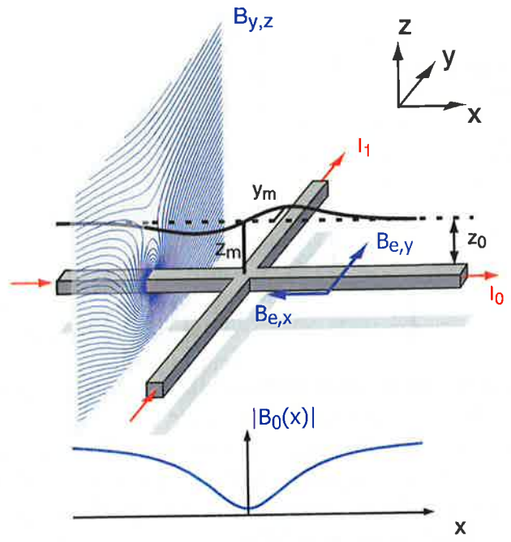

Figure 1.6: Dimple trap. Two crossing waveguides form a dimple trap. The solid black line indicates a trace through the magnetic field minimum which is twisted with respect to the unperturbed quadrupole line (dashed line). Figure adapted from [28].

and

$$B_0 = |B_{e,x} + \mu_0 I_1/2\pi z_0| \quad (1.16)$$
$$B' = \mu_0 I_0/2\pi z_0^2 \quad (1.17)$$
$$B'' = \mu_0 I_1/\pi z_0^3. \quad (1.18)$$

The trap frequencies are then approximately

$$\omega_x = \sqrt{\frac{\mu}{m}\frac{\mu_0 I_1}{\pi z_0^3}} \quad \text{and} \quad \omega_\perp = \sqrt{\frac{\mu}{m}\frac{\mu_0^2 I_0^2}{4\pi^2 z_0^4 \cdot |B_{e,x} + \mu_0 I_1/2\pi z_0|}}, \quad (1.19)$$

where μ and m are the atomic magnetic moment and mass (note, that $B_{e,x}$ has the opposite sign to I_1). Raising I_1 results in a twisting of the trap; if desired, one can thus turn the main trap axis from x to y by adjusting the currents and fields accordingly [28]. Using several crossing wires, more complex double- and multi-well traps can be created.

1.3 Microwave near-field potentials

The generation of entanglement in a BEC requires good control not only over the motional and internal degrees of freedom but also over collisional interactions (see section 2.2.6). In particular, for our experiment, exact control over the wave function overlap between state $|0\rangle$ and $|1\rangle$ is required, thus a state selective potential is needed.

Since the clock states have the same magnetic moment, such a potential cannot be produced by static magnetic fields. A well known technique is the use of optical dipole traps [74], which make use of the AC Stark effect. Here, state selectivity is achieved by tuning the frequency and/or the polarization of the trapping laser. However, a far detuned laser does not provide the needed state selectivity for our states whereas light close to a resonance can easily be absorbed and heats the atoms through photon scattering. Additionally, optical traps are hard to integrate on an atom chip because of diffraction on the chip surface and the required high light intensities. Also, versatile, non-periodic trapping geometries are hard to achieve. In section 1.1.3 it was shown that microwave radiation leads to a differential AC Zeeman shift of hyperfine states very similar to the AC Stark effect in dipole traps. Microwave potentials generated by far-field radiation were already studied in the 1990s [75, 76], but hundreds of kilowatts of circulating microwave power inside a cavity were necessary, because the centimeter wavelength of the microwave prevents tight focusing and thus limits the attainable potential gradients.

Atom chips present a natural solution to this problem. Using microwave near-fields, generated by micrometer-sized waveguides, it is possible to realize much stronger gradients with only milliwatts of power. This is because near-field gradients do not depend on the wavelength, but instead on the transverse waveguide dimensions and the distance from the waveguide. In addition, this enables tailoring of the potentials on the micrometer scale. In a similar way, radiofrequency fields were used to generate potentials on atom chips [77]. By comparison, microwave potentials have the important advantage that the different transitions are split by the Zeeman effect, which we make use of to adjust the state dependence of the potentials simply through the microwave frequency.

State selective potentials

To state selectively manipulate the atoms, we have integrated a coplanar waveguide (CPW) on our atom chip [45]. The microwave field amplitude falls off rapidly around the waveguide and the strong gradient is used to state selectively shift the position of a magnetic trap above it. A schematic of this

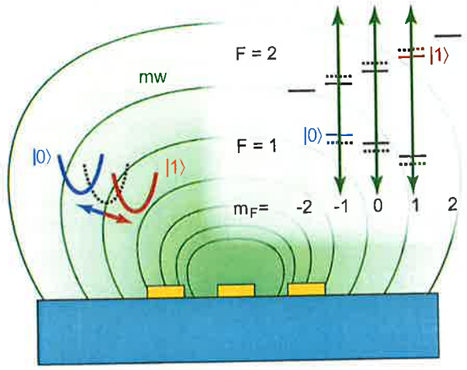

Figure 1.7: Schematic of the state-selective microwave potential. The combination of a static magnetic trap (black dotted) with a microwave near field (green) around the CPW (not to scale) results in a state selective shift of the trap. The inset shows the ^{87}Rb term scheme with a π polarized and strongly blue-detuned microwave, leading to opposite energy shifts of the clock states. The dotted lines represent the unperturbed energy levels. The trap for state $|0\rangle$ (blue) is pushed away from the waveguide while the trap for state $|1\rangle$ (red) is pulled toward it. Note that in the experiment, all mw polarizations are present.

technique is shown in figure 1.7. The microwave frequency for the squeezing experiments reported in this thesis is strongly blue detuned ($\Delta \equiv \Delta_{1,0}^{2,0} = 2\pi \times 12\,\mathrm{MHz}$) with respect to the transition $|1,0\rangle \leftrightarrow |2,0\rangle$. The energy shift of the clock states can thus be described in good approximation by (1.10) and (1.11), taking into account that all three polarization components are present in the microwave near-field. In this configuration, both states experience a microwave potential of opposite sign, and with different magnitude due to the different hyperfine transition strengths. State $|0\rangle$ is a low-microwave-field-seeker and is pushed away from the coplanar waveguide while state $|1\rangle$ is a high-microwave-field-seeker and pulled toward the waveguide. For details on the resulting shifted traps and the atomic motion, see chapter 4.

1.4 Two component Bose-Einstein condensates

1.4.1 Bose-Einstein condensation

Bose-Einstein condensation (BEC) was predicted in 1925 by Einstein [78], based on ideas by Bose, for a system of a fixed number of indistinguishable and non-interacting bosonic particles. It is characterized by a macroscopic occupation of the single-particle ground state below a certain temperature and arises solely from statistical considerations. BEC was first thought of as a purely theoretical construct since no non-interacting particles were known (except photons, where number is not a conserved quantity) and it was hard to imagine how any ensemble of interacting particles should undergo BEC before regular condensation. However, when superfluidity in (strongly interacting) ^{4}He was discovered, London soon suggested that it was a manifestation of BEC. Today, we know that the two phenomena are closely related, as are also BCS superconductivity and the laser. It took more than 70 years until BEC in its original sense was realized for the first time in dilute atomic gases [4, 5, 6], which led to an explosion of research in the field of cold atoms and quantum physics in general. The breakthrough was achieved with alkali atoms where elastic collisions (so called 'good collisions', as they are needed for thermalization) dominate over inelastic ('bad') collisions that lead to molecule formation and atom loss. There exist numerous reviews and text books on the historical and both the theoretical and experimental aspects of BEC of which only a few are listed in the references [79, 80, 81, 82].

For the understanding of BEC, the concept of indistinguishability plays a key role. Consider 10 balls (atoms) which we would like to distribute between 10 buckets (states). If the balls are distinguishable (as particles are in classical physics) there exist 10 possibilities to put all balls into one bucket but $10! = 3\,628\,800$ possibilities to fill each bucket with one ball. On the other hand, if the balls are indistinguishable (as quantum mechanical bosons are), there are still 10 possibilities to put all in one bucket but only *one* possibility to distribute them equally. The possibility that all balls are in the same bucket (all atoms in the same state) has a much larger relative weight. This so called *bunching* is a fundamental property of bosons. It becomes important when the number of particles N is equal to or larger than the number of accessible states p (the *degeneracy condition*) and eventually leads to BEC.

In a gas, each atom can be described as a quantum mechanical wave packet with an extent given by the de Broglie wavelength $\lambda_{dB} = h/\sqrt{2\pi m k_B T}$, where m is the atomic mass, and T is the temperature of the gas. λ_{dB} can be considered as the position uncertainty associated with the thermal velocity

of the atoms. When the gas is cooled below a critical temperature T_c, the wavelength becomes larger than the average particle separation $n^{-1/3}$, the indistinguishability of the atoms becomes relevant, and BEC sets in. For a uniform three-dimensional gas the transition temperature and the atomic density n are related as $n\lambda_{dB}^3 = 2.612$.

In a harmonic trap with $\omega_{ho} = (\omega_x\omega_y\omega_z)^{1/3}$, the critical temperature can be estimated in a simple way. The mean density of single particle states per unit energy ϵ is given by $\frac{dp}{d\epsilon} = \epsilon^2/(\hbar\omega_{ho})^3$. The degeneracy condition is reached when the number of particles N is about equal to the number of states p that can be thermally occupied

$$N \simeq p = \int_0^{k_B T_c} \epsilon^2/(\hbar\omega_{ho})^3 d\epsilon \quad \Leftrightarrow \quad k_B T_c \simeq \hbar\omega_{ho} N^{1/3}. \tag{1.20}$$

A full length calculation [79], including the Bose-Einstein distribution of non-interacting particles in thermal equilibrium and the Gaussian shape of the harmonic oscillator ground state, yields

$$k_B T_c = 0.94\,\hbar\omega_{ho} N^{1/3}. \tag{1.21}$$

The number of atoms in the ground state as a function of temperature is then

$$N_0(T) = N(1 - (T/T_c)^3). \tag{1.22}$$

These results are obtained for $k_B T \gg \hbar\omega_{ho}$ and $N \gg 1$ in three dimensions. Finite size effects ($N \nrightarrow \infty$) reduce the condensate fraction, lower the transition temperature, and make the transition less sharp [83].

It should be noted that in lower dimensions ultra cold bosons behave in general differently than described here. For example, in very elongated 1D-traps, the atoms first undergo a transition to a so called quasi-condensate [84] with a density profile known from the 3D-case but phase fluctuations along the long axis. At lower temperatures and low density they can even enter the regime of the so called Tonks gas where they behave as impenetrable Bosons, in many ways similar to Fermions.

1.4.2 The Gross-Pitaevskii equation

So far, we have mainly discussed non-interacting particles. However, for many phenomena the inter-particle interactions play a decisive role. In our experiment, we produce very cold ensembles with $T \ll T_c$ and undetectable thermal occupation. We can therefore in most cases approximate them as pure BECs at $T = 0$ which have been shown to be well described by the *Gross-Pitaevskii* or *mean-field* theory [79, 81].

Spinless GPE

The mean field theory is a Hartree-Fock theory where the many-body wave function $\Phi_N(\mathbf{r}_1...\mathbf{r}_N)$ of the BEC is simply the product of normalized single particle states. To find the ground state of the condensate (for now neglecting that the atoms can be in different hyperfine states) we write it as

$$\Phi_N(\mathbf{r}_1...\mathbf{r}_N) = \prod_{i=1}^{N} \phi(\mathbf{r}_i), \tag{1.23}$$

where $\phi(\mathbf{r})$ is the single-particle wave function (or *mode function* of the condensate) to be determined. The mean expectation value of the energy in an external potential V_{ext} is then given by

$$\begin{aligned}\langle H\rangle_N &= N\int d\mathbf{r}\left(\frac{\hbar^2}{2m}|\nabla\phi(\mathbf{r})|^2 + V_{\text{ext}}(\mathbf{r})|\phi(\mathbf{r})|^2\right)\\ &\quad + \frac{1}{2}N(N-1)g\int d\mathbf{r}|\phi(\mathbf{r})|^4\end{aligned} \tag{1.24}$$

with effective interaction constant $g = 4\pi\hbar^2 a/m$ and a the s-wave scattering length. The first term corresponds to the kinetic and potential energy of N single particles in the external potential. The second term takes into account the interaction *between* the condensate atoms. Despite complicated interatomic potentials, the mean-field interaction is well described by s-wave scattering. Each of the N atoms can interact with $(N-1)$ other atoms raising the total energy by the elastic scattering energy g (the factor $\frac{1}{2}$ arises from the indistiguishability of the scattering partners). For large atom number $N(N-1) \approx N^2$.

Minimizing the functional 1.24 with respect to ϕ, subject to the constraint of the normalization of ϕ, and dividing by N yields:

$$\left(-\frac{\hbar^2}{2m}\nabla^2 + V_{\text{ext}}(\mathbf{r}) + Ng|\phi(\mathbf{r})|^2\right)\phi(\mathbf{r}) = \mu\phi(\mathbf{r}) \tag{1.25}$$

where $\mu = \delta\langle H\rangle_N/\delta N$ is the chemical potential. In the literature, one finds this non-linear Schrödinger equation rewritten in terms of the condensate's order parameter $\Phi(\mathbf{r}) = \sqrt{N}\phi(\mathbf{r})$ as the famous Gross-Pitaevskii equation (GPE)

$$\left(-\frac{\hbar^2}{2m}\nabla^2 + V_{\text{ext}}(\mathbf{r}) + g|\Phi(\mathbf{r})|^2\right)\Phi(\mathbf{r}) = \mu\Phi(\mathbf{r}). \tag{1.26}$$

For non-interacting gases ($g = 0$) in a harmonic trap, the solution is simply the single-particle ground state wave function of that trap

$$\Phi(\mathbf{r}) = \sqrt{N}\left(\frac{m\omega_{ho}}{\pi\hbar}\right)^{\frac{3}{4}} \exp\left(-\frac{m}{2\hbar}(\omega_x x^2 + \omega_y y^2 + \omega_z z^2)\right), \tag{1.27}$$

with an average extent $a_{ho} = \sqrt{\frac{\hbar}{m\omega_{ho}}}$ which is independent of N.

Thomas-Fermi approximation

In interacting gases, especially in large condensates, the kinetic energy is often much smaller than both the potential and the interaction energy and can be neglected. This is the so called Thomas-Fermi approximation which directly gives the atom density distribution:

$$\begin{aligned} n(\mathbf{r}) = |\Phi(\mathbf{r})|^2 &= \frac{1}{g}\left(\mu - V_{\text{ext}}(\mathbf{r})\right) \qquad \text{for} \qquad V_{\text{ext}}(\mathbf{r}) < \mu \\ n(\mathbf{r}) &= 0 \qquad\qquad\qquad\qquad\quad \text{for} \qquad V_{\text{ext}}(\mathbf{r}) \geq \mu \end{aligned} \tag{1.28}$$

The density profile thus follows the inverse trapping potential, bounded by the surface on which $V_{\text{ext}}(\mathbf{r}) = \mu$. In a harmonic trap the normalization condition on $\int dr^3\, n(\mathbf{r}) = N$ yields

$$\mu = \frac{\hbar\omega_{ho}}{2}\left(\frac{15Na_s}{a_{ho}}\right)^{\frac{2}{5}} \tag{1.29}$$

and one finds the Thomas-Fermi radii to be $R_{\text{TF},i} = \sqrt{2\mu/(m\omega_i^2)}$ with $i \in \{x, y, z\}$.

For small condensates, the kinetic energy term can be taken into account perturbatively and the condensate radius lies between a_{ho} and R_{TF}. Also, for highly elongated traps, the Thomas-Fermi approximation has to be extended. An approximate analytical solution for small condensates in traps with arbitrary aspect ratio can be found in [85]. We use this approximation for analyzing our experiment in chapter 4.

Time dependence

It is not entirely straight forward to generalize the mean field theory to the time dependent case, and only possible when $N(t) = N(0)$ i. e. no particle losses are assumed [81]. The result however is – as one intuitively expects – that the chemical potential is simply replaced by the time derivative. The time dependent GPE is thus

$$i\hbar\frac{\delta\Phi(\mathbf{r},t)}{\delta t} = \left(-\frac{\hbar^2}{2m}\nabla^2 + V_{\text{ext}}(\mathbf{r},t) + g|\Phi(\mathbf{r},t)|^2\right)\Phi(\mathbf{r},t). \tag{1.30}$$

The two component GPE

If the atoms in the condensate can occupy two different internal states, the mean field theory has to be extended. In general, the interaction g_{ii} between two atoms in state $|i\rangle$ differs from the interaction g_{jj} of two atoms in state $|j\rangle$ which again differs from the inter-state interaction $g_{ij} = g_{ji}$. This leads to a pair of coupled GPEs

$$i\hbar\frac{\delta\Phi_i(\mathbf{r},t)}{\delta t} = \left(-\frac{\hbar^2}{2m}\nabla^2 + V_{\text{ext}}(\mathbf{r},t) + g_{ii}|\Phi_i(\mathbf{r},t)|^2 + g_{ij}|\Phi_j(\mathbf{r},t)|^2\right)\Phi_i(\mathbf{r},t). \tag{1.31}$$

with $i \neq j$.

For the states $|0\rangle$ and $|1\rangle$ of ^{87}Rb the inter- and intra-state scattering lengths are equal within 5%: $a_{00} : a_{01} : a_{11} = 100.40\,a_0 : 97.66\,a_0 : 95.00\,a_0$ [86] where $a_0 = 0.53$ Å is the Bohr radius. Nevertheless, this small difference can have considerable consequences. In a mixture or superposition of the two states, state $|0\rangle$ tends to form a lower density shell around a higher density core of state $|1\rangle$ to minimize the total energy. While in large condensates this can lead to almost complete phase separation [87], the effect in small ensembles ($N \sim 1000$) is that of a slight broadening of the wave function of state $|0\rangle$ and a compression for state $|1\rangle$ by a few percent.

1.4.3 Atom losses

The duration of an experimental cycle, i. e. how long an ensemble of atoms can be held in a magnetic trap, is limited by several loss mechanisms. Namely, they are Majorana spin flips and inelastic collisions between the atoms and with thermal background gas. Losses due to interaction with the surface can be neglected for our traps (distance from surface $z_0 \approx 40\,\mu$m). Besides limiting the lifetime of the trapped atoms, losses also cause a change of the differential collisional energy shift between the clock states over time. Since loss is a random process, it is thus a source for phase noise (see section 4.4.2).

Majorana spin flips

An atom moving in a magnetic trap traverses over time different regions of the trap with varying magnetic field magnitude B and direction θ. The atom's spin precesses around the trap field and follows small changes adiabatically if the rate of change of the magnetic field is smaller than the atom's Larmor frequency

$$\frac{d\theta}{dt} \ll \omega_L = \mu_B|g_F|B/\hbar. \tag{1.32}$$

If, on the other hand, the magnetic field changes too fast, the atom can be transferred into a different magnetic sublevel m_F. It then becomes either untrapped or experiences a sudden change of the trapping potential which results in heating and subsequent loss. This process is called Majorana spin flip [88, 89] and happens in regions with small or vanishing magnetic field. It is the main reason why magnetic traps are almost always Ioffe-Pritchard traps and not quadrupole traps which have a 'magnetic hole' in the center. An upper limit for the rate of change of the magnetic field is the trap frequency, so that tighter traps require a larger magnetic field in the center. The traps used in our experiments have sufficiently large magnetic fields, such that Majorana spin flips can be neglected.

Collisional losses

Elastic collisions in a BEC lead to an additional mean field potential, which is well described by the Gross-Pitaevskii theory (see previous section). Inelastic collisions, however, can change the state of the involved collision partners and thus lead to trap loss. For a single state ensemble of N atoms, collisional loss is well described by the following rate equation

$$\frac{1}{N}\frac{dN}{dt} = -\gamma_{bg} - K\langle n\rangle - L\langle n^2\rangle, \tag{1.33}$$

where $n(\mathbf{r})$ is the density of the atom cloud.

The first term describes losses due to collisions with the background gas and is proportional to the pressure in the vacuum cell but independent of n. The background gas molecules are at room temperature and one molecule impinging on the ultra-cold cloud can kick several atoms out of the trap. These losses lead to an exponential decay of the atom number over time.

The second and third terms describe losses due to inelastic collisions of two and three atoms within the cloud, respectively. For a BEC in the Thomas-Fermi regime the loss rates are

$$\gamma_2 = K\langle n\rangle \overset{\text{TF}}{\propto} \omega_{ho}^{6/5} N^{2/5} \tag{1.34}$$

$$\gamma_3 = L\langle n^2\rangle \overset{\text{TF}}{\propto} \omega_{ho}^{12/5} N^{4/5}. \tag{1.35}$$

It is noteworthy that the loss constants for a thermal gas are 2! times higher in the case of two-body collisions and even 3! times higher for three-body collisions [90]. This is due to the bunching of atoms in a thermal gas which is not present in a BEC.

Two-body collisions Two processes contribute to losses in two-body collisions. The dominant one is spin exchange interaction, the other is spin-dipole interaction, which is about two orders of magnitude smaller and can be neglected [82]. Since total m_F has to be conserved, spin exchange of the type $|2,1\rangle + |2,1\rangle \Rightarrow |2,0\rangle + |2,2\rangle$ can only occur for state $|1\rangle = |2,1\rangle$ but not for state $|0\rangle = |1,-1\rangle$, because there is no state with $m_F < -1$ in the $F = 1$ manifold and transfer of one collision partner into the $F = 2$ manifold is energetically forbidden. The two-body rate constant for state $|1\rangle$ is $K_1 = 1.194(19) \times 10^{-13}\,\mathrm{cm^3 s^{-1}}$ [86]. Two-body collisions are the dominant loss mechanism for this state.

Three-body collisions Momentum conservation prevents molecule formation in two-body collisions. In three-body collisions on the other hand, two atoms can form a molecule and the released binding energy is converted into kinetic energy of the molecule and the third atom. Usually, this energy is larger than the trap depth so that both are lost from the trap. This process is dominant for state $|0\rangle$ with the loss constant $L_0 = 5.8(1.9) \times 10^{-30}\,\mathrm{cm^6 s^{-1}}$ [90].

Superposition In a superposition of the two states, collisions of the type $|0\rangle + |1\rangle \Rightarrow |1,0\rangle + |2,0\rangle$ are possible which leads to additional two-body losses. The rate constant for this process is $K_{01} = 0.780(19) \times 10^{-13}\,\mathrm{cm^3 s^{-1}}$ [86].

Chapter 2

Spin squeezing theory

Long-living atomic states, such as the hyperfine states of the electronic ground state, have well defined energies. In principle, the energy of such a state is an intrinsic property of the atom and only depends on natural constants. The energy difference $\Delta E = \hbar\omega_0$ between two states is thus – leaving aside the possibility that the natural constants themselves might change over time – constant. In an atomic clock, a local oscillator with frequency ω is locked to the atomic frequency ω_0, so that $\delta = \omega - \omega_0 = const.$ Thereby, the atomic stability is transfered to the local oscillator.

Of course, in a real experiment, the atomic energy levels are influenced by external fields (see section 1.1) and other effects, such as collisional, gravitational, or rotational shifts. Atom interferometers are used to measure these effects with extremely high precision [91]. In atomic clock experiments on the other hand, one tries to minimize their influence on the atomic energies because technical fluctuations then lead to clock instabilities. Today's best atomic clocks have reduced this technical noise to such a low level that their stability is now limited by a more fundamental effect, the *quantum projection noise* [12]. The *standard quantum limit*, which is imposed by this effect, can only be overcome by the use of multi-particle entangled states, such as spin squeezed states.

2.1 Atomic clocks and interferometers

In this section, I describe the basic working principle of an atomic interferometer or atomic clock. I also explain the origin of the standard quantum limit, which lies at the very heart of quantum mechanics.

2.1.1 Rabi oscillations

Consider an atom with two internal states $|0\rangle$ and $|1\rangle$, separated by an energy difference $\Delta E = \hbar\omega_0$. Near resonant electromagnetic radiation couples the two states and can be used to prepare the atom in a superposition state $|\psi\rangle = c_0|0\rangle + c_1|1\rangle$. (The labels for the ^{87}Rb clock states introduced in section 1.1.2 are not by accident chosen as $|0\rangle$ and $|1\rangle$. However, the following considerations are much more generally applicable to any two-level system.)

The strength of the coupling is characterized by the Rabi frequency Ω_R, which depends on the field strength and the specific transition in question. For microwave transitions between magnetic sub-levels of the electronic ground state, the Rabi frequency is given by equation (1.7) for a one-photon or by (1.12) for a two-photon transition.

The atom can be prepared in any desired superposition by controlling Ω_R and the duration t of a pulse of electromagnetic radiation of frequency ω. In a frame, rotating with ω, the atom's state after the pulse is $|\psi(t)\rangle = c_0(t)|0\rangle + c_1(t)|1\rangle$ with [14]

$$\begin{aligned} c_0(t) &= c_0(0)\left[\cos\left(\frac{\Omega t}{2}\right) - \frac{i\delta}{\Omega}\sin\left(\frac{\Omega t}{2}\right)\right] + \frac{i\Omega_R^*}{\Omega}c_1(0)\sin\left(\frac{\Omega t}{2}\right) \\ c_1(t) &= c_1(0)\left[\cos\left(\frac{\Omega t}{2}\right) + \frac{i\delta}{\Omega}\sin\left(\frac{\Omega t}{2}\right)\right] + \frac{i\Omega_R}{\Omega}c_0(0)\sin\left(\frac{\Omega t}{2}\right), \end{aligned} \tag{2.1}$$

with the detuning δ and the effective Rabi frequency Ω

$$\begin{aligned} \delta &= \omega - \omega_0 \\ \Omega &= \sqrt{|\Omega_R|^2 + \delta^2}. \end{aligned} \tag{2.2}$$

Starting with an atom in the ground state $|\psi(0)\rangle = |0\rangle$, the probabilities for finding it in either state are

$$\begin{aligned} p_1(t) &= |c_1(t)|^2 = \frac{|\Omega_R|^2}{\Omega^2}\sin^2\left(\frac{\Omega t}{2}\right) \\ p_0(t) &= |c_0(t)|^2 = 1 - |c_1(t)|^2. \end{aligned} \tag{2.3}$$

On resonance, the atom thus coherently oscillates in time between its two states and by adjusting Ωt, i. e. the power and length of the electromagnetic pulse, any desired superposition can be prepared. Particularly, $\Omega t = \frac{\pi}{2}$ (a $\frac{\pi}{2}$-*pulse*) which results in an equal superposition of the type $|\psi\rangle = \frac{1}{\sqrt{2}}(|0\rangle + e^{i\varphi}|1\rangle)$ will be of further importance.

2.1.2 The Bloch sphere

A useful tool to visualize the atom's state is a vector operator $\hat{\mathbf{s}}$ defined by

$$\begin{aligned} \hat{s}_x &= (|0\rangle\langle 1| + |1\rangle\langle 0|)/2 \\ \hat{s}_y &= (|1\rangle\langle 0| - |0\rangle\langle 1|)/2i \\ \hat{s}_z &= (|1\rangle\langle 1| - |0\rangle\langle 0|)/2. \end{aligned} \tag{2.4}$$

It is equivalent to a spin-$\frac{1}{2}$ angular momentum operator, since it acts on a two dimensional complex vector space and the commutators satisfy the same algebra

$$[\hat{s}_i, \hat{s}_j] = i\epsilon_{ijk}\hat{s}_k, \tag{2.5}$$

where ϵ_{ijk} is the Levi-Civita symbol. The z-component of $\hat{\mathbf{s}}$ is proportional to the internal energy operator and its eigenstates with eigenvalues $m = \mp\frac{1}{2}$ are the states $|0\rangle$ and $|1\rangle$, respectively. Any pure state $|\psi\rangle$ of the two-level system can be depicted using the expectation value $\langle\psi|\hat{\mathbf{s}}|\psi\rangle$ as a vector with length $\frac{1}{2}$ and components

$$\begin{aligned} s_x = \langle\hat{s}_x\rangle &= (c_0^*c_1 + c_1^*c_0)/2 = \frac{1}{2}\sin\upsilon\cos\varphi \\ s_y = \langle\hat{s}_y\rangle &= (c_1^*c_0 - c_0^*c_1)/2i = -\frac{1}{2}\sin\upsilon\sin\varphi \\ s_z = \langle\hat{s}_z\rangle &= (|c_1|^2 - |c_0|^2)/2 = \frac{1}{2}\cos\upsilon. \end{aligned} \tag{2.6}$$

This is the so called *Bloch vector* of the state and the set of all pure states spans the *Bloch sphere* (figure 2.1). The angles υ and φ represent the relative weight and phase of the two states $|0\rangle$ and $|1\rangle$ in a superposition.

Operations on the state can be depicted by defining a second vector, the *Rabi vector*

$$\mathbf{\Omega} = \begin{pmatrix} -\mathrm{Re}(\Omega_R) \\ \mathrm{Im}(\Omega_R) \\ -\delta \end{pmatrix}, \tag{2.7}$$

which acts as a torsional moment with $\dot{\mathbf{s}} = \mathbf{\Omega}\times\mathbf{s}$. For example, for $\delta = 0$ and an atom initially in the ground state, the Rabi vector lies on the equator and the atom's Bloch vector points to the south pole. When switching on the Rabi drive, the state vector is turned northward, after a time corresponding to a $\frac{\pi}{2}$-pulse it lies on the equator and forms a right angle with $\mathbf{\Omega}$, after a π-pulse it points to the north pole, and for longer pulses it is turned back south. It can easily be seen that if $\delta \neq 0$, the north pole is never reached and

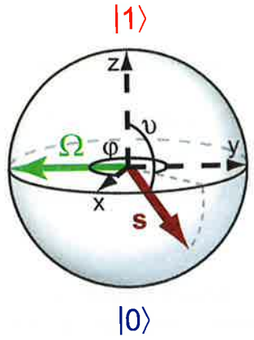

Figure 2.1: Bloch sphere. with an Bloch vector $\mathbf{s}$ and a Rabi vector $\mathbf{\Omega}$ with $\delta = 0$ and $\Omega_R = -i/2$. The angles υ and φ characterizing the state are indicated.

the Rabi oscillations have a diminished contrast, as expected from equation 2.3.

In the lab frame, both the Rabi vector and the Bloch vector precess around the z-axis at a rate ω and ω_0, respectively. Throughout this thesis, transformation into a frame rotating with the frequency ω is made, such that the Rabi vector is stationary on the Bloch sphere and the azimuth angle between the Bloch vector and the Rabi vector changes at the rate δ. The atomic state in the lab frame, expressed using the coefficients of the rotating frame from equation (2.1), is

$$|\psi(t)\rangle_{\text{lab}} = c_0(t)e^{-i(\frac{E_0}{\hbar}-\frac{\delta}{2})t}|0\rangle + c_1(t)e^{-i(\frac{E_1}{\hbar}+\frac{\delta}{2})t}|1\rangle, \tag{2.8}$$

where E_0 and E_1 are the states' eigenenergies.

2.1.3 Ramsey interferometry

Rabi oscillations can in principle be used to lock the local oscillator frequency to the atom's frequency and thus realize an atomic clock. However, the flopping rate Ω is a function not only of the detuning but also of the electromagnetic field amplitude. Thus, intensity gradients over the atomic cloud lead to a dephasing of the oscillation in time (an inhomogeneous broadening of the resonance). Also, the total power of the irradiated field must be kept extremely stable throughout the measurement. More importantly, systematic shifts of ω_0 during the pulses prohibit the use of Rabi-spectroscopy for accurate clocks. In our case, when the two-photon drive is applied, the states

$|0\rangle$ and $|1\rangle$ become dressed by the off-resonant driving fields and thus are not only shifted in energy, but also loose their excellent coherence properties.

To avoid these problems, an atomic clock commonly uses *Ramsey interferometry*, where the drive is pulsed on only for short times, and the interferometer signal is sensitive to the free atomic evolution between the pulses. A Ramsey interferometer [92] consists of two $\frac{\pi}{2}$-pulses, separated by a time T_R. Starting with the atom in state $|0\rangle$, the first pulse has the role of a beam splitter in a light interferometer and prepares an equal superposition $|\psi\rangle = \frac{1}{\sqrt{2}}(|0\rangle + |1\rangle)$. In the Bloch-picture, the Bloch vector is turned from the south pole to the equator and forms a right angle with the Rabi vector. The frequency ω is adjusted such that during the pulses $\delta = 0$, i. e. $\omega = \omega_0 + \omega_{\text{ls}}$ (see section 1.1.4). Between the pulses, when the drive is off, $\delta \approx \omega_{\text{ls}} \neq 0$. Therefore, a phase $\varphi = \delta T_R$ between the local oscillator phase and the atomic phase is accumulated during the Ramsey time T_R. The state now reads $|\psi(t = T_R)\rangle = \frac{1}{\sqrt{2}}(|0\rangle + e^{i\varphi}|1\rangle)$. In the Bloch picture, keeping the Rabi vector fixed, the Bloch vector rotates at a rate δ in the equatorial plane. A second $\frac{\pi}{2}$-pulse converts the phase difference into a difference in detection probabilities for $|0\rangle$ and $|1\rangle$. The outcome depends on the phase of the second pulse; for $\Omega_R \in \mathbb{R}^+$, the result is:

$$\begin{aligned} |\psi(T_R)\rangle &= \frac{1}{2}\left((1+ie^{i\varphi})|0\rangle + (i+e^{i\varphi})|1\rangle\right) \\ \Rightarrow \quad p_0(T_R) &= \frac{1}{2} - \frac{1}{2}\sin(\varphi) \\ p_1(T_R) &= \frac{1}{2} + \frac{1}{2}\sin(\varphi) \end{aligned} \tag{2.9}$$

Using an ensemble of N atoms, φ is thus read out by detecting the atom number difference $n = \frac{1}{2}(N_1 - N_0)$ with $N_0 = p_0 N$ atoms in the ground state and $N_1 = p_1 N$ atoms in the excited state (see figure 2.2). The Ramsey signal is most sensitive to variations in φ on the slope of the fringe, where $\frac{\delta n}{\delta \varphi} = \frac{N}{2}$ is maximal. Atomic clocks therefore operate at this point.

The standard quantum limit

The state of an atom collapses upon measurement with a probability p_0 into state $|0\rangle$ and with a probability $p_1 = 1 - p_0$ into state $|1\rangle$. In an ensemble with N *independent* atoms, which have all been prepared in the same state, one measures on average $\overline{n} = \frac{N}{2}(p_1 - p_0) = N(p_1 - \frac{1}{2})$. Repeating the experiment several times, one finds a binomial distribution of n with

$$\Delta n^2 = \Delta N_0^2 = \Delta N_1^2 = N p_0 p_1, \tag{2.10}$$

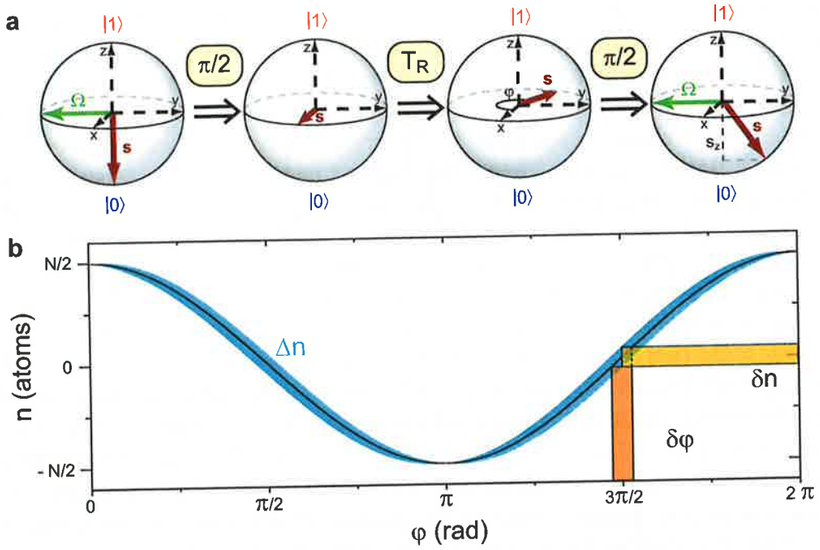

Figure 2.2: Ramsey Interferometry. a, The different steps of a Ramsey interferometer visualized for a single atom on the Bloch sphere. A $\frac{\pi}{2}$-pulse turns the state vector into the equatorial plane. During the Ramsey time T_R it accumulates a phase which is read out with a second $\frac{\pi}{2}$-pulse. **b**, Relative atom number n as a function of the Ramsey phase φ for an ensemble of $N = 100$ atoms. The highest phase sensitivity is reached where $n = 0$ and $\frac{\delta n}{\delta \varphi} = \frac{N}{2}$. The blue shaded area is the standard deviation of n due to quantum projection noise.

where Δx^2 denotes the variance of the quantity x. Specifically, on the slope of a Ramsey fringe, with $p_0 = p_1 = \frac{1}{2}$, one measures $\overline{n} = 0$ and $\Delta n^2 = \frac{N}{4}$. This is known as *quantum projection noise* [11] and is closely related to shot noise in a laser.

The best achievable phase sensitivity in a Ramsey interferometer operating with independent atoms is thus

$$\Delta\varphi^2 = \Delta n^2 \left(\frac{\delta\varphi}{\delta n}\right)^2 = \frac{1}{N}. \tag{2.11}$$

This so called *standard quantum limit* limits today's best atomic clocks [12]. It arises from the very basic axiom of quantum mechanics that the outcome of a measurement can only be predicted with a certain probability. However, it can be overcome by entangling the atoms, thus making the outcome of the measurement on one atom dependent on the other atoms.

2.2 Spin squeezing

As described in the previous section, an atomic clock employing independent atoms is limited to the standard quantum limit by quantum projection noise. However, by entangling the atoms, it is possible to reduce the quantum noise in the phase quadrature φ at the cost of increasing it in the perpendicular quadrature, the relative atom number n. To understand this process, it is useful to treat the N particles as a combined quantum system.

2.2.1 Stationary two-mode model

The internal state of a BEC of N atoms can be described by a collective spin operator $\hat{\mathbf{S}} = \sum_{i=1}^{N} \hat{\mathbf{s}}_i$, the sum of the individual spin operators of each atom [11]. The direct summation is the only way to combine the individual spins having the same external wave function such that the resulting total wave function is symmetric. It is thus unaffected by particle exchange, and is valid for indistinguishable (Bose-Einstein condensed) bosonic atoms. In second quantization, the spin operator components can be defined as [16]

$$\begin{aligned}
\hat{S}_x &= \frac{1}{2}\int d^3r(\hat{\Psi}_1^\dagger\hat{\Psi}_0 + \hat{\Psi}_0^\dagger\hat{\Psi}_1) \\
\hat{S}_y &= \frac{1}{2i}\int d^3r(\hat{\Psi}_1^\dagger\hat{\Psi}_0 - \hat{\Psi}_0^\dagger\hat{\Psi}_1) \\
\hat{S}_z &= \frac{1}{2}\int d^3r(\hat{\Psi}_1^\dagger\hat{\Psi}_1 - \hat{\Psi}_0^\dagger\hat{\Psi}_0),
\end{aligned} \tag{2.12}$$

where $\hat{\Psi}_j \equiv \hat{\Psi}_j(\mathbf{r})$ is the bosonic annihilation operator for an atom in state $|j\rangle$ at position $\mathbf{r}$. In a stationary two mode model, we assume that the spatial degrees of freedom can be described by one spatial wave function for each component

$$\hat{\Psi}_0(\mathbf{r}) = \hat{b}\phi_0(\mathbf{r}) \qquad \text{and} \qquad \hat{\Psi}_1(\mathbf{r}) = \hat{a}\phi_1(\mathbf{r}), \tag{2.13}$$

where $\phi_j(\mathbf{r})$ is the normalized spatial mode function (see 1.4.2) of state $|j\rangle$ and $\hat{a}$ and $\hat{b}$ are the bosonic anihilation operators obeying the usual commutation relations $[\hat{a}, \hat{a}^\dagger] = 1$, $[\hat{b}, \hat{b}^\dagger] = 1$, $[\hat{a}, \hat{b}] = 0$, and $[\hat{a}, \hat{b}^\dagger] = 0$. For spatially completely overlapping states, equation 2.12 reduces to

$$\begin{aligned}
\hat{S}_x &= (\hat{a}^\dagger\hat{b} + \hat{b}^\dagger\hat{a})/2 \\
\hat{S}_y &= (\hat{a}^\dagger\hat{b} - \hat{b}^\dagger\hat{a})/(2i) \\
\hat{S}_z &= (\hat{a}^\dagger\hat{a} - \hat{b}^\dagger\hat{b})/2.
\end{aligned} \tag{2.14}$$

As in the single atom case in section 2.1.2, the atomic ensemble can be represented by a Bloch vector $\mathbf{S} = \langle\Psi|\hat{\mathbf{S}}|\Psi\rangle$ where $|\Psi\rangle$ is the many-particle wave function. $S_z = (N_1 - N_0)/2$ is half the atom number difference between the states (which was already introduced and called n in section 2.1.3) and thus directly measurable.

2.2.2 Coherent spin states

Applying the two-photon drive to a BEC in $|\Psi_{\text{ini}}\rangle = |0,\phi\rangle^{\otimes N}$ (all atoms in the internal state $|0\rangle$ and in the spatial mode ϕ), prepares it in a so called coherent spin state (CSS)

$$|\Psi_\varphi\rangle = (c_0|0,\phi\rangle + c_1|1,\phi\rangle)^{\otimes N}, \tag{2.15}$$

where c_0 and c_1 are in general complex coefficients with $|c_0|^2 + |c_1|^2 = 1$, and the index φ denotes the phase between c_0 and c_1, as for the single atom (see equation 2.6). A useful property of a CSS is

$$e^{-i\alpha\hat{S}_z}|\Psi_\varphi\rangle = |\Psi_{\varphi+\alpha/2}\rangle. \tag{2.16}$$

From this, it can be seen that a Hamiltonian containing $\hat{S}_z$ leads to a precession of the state around the z-axis.

Expanding a CSS into Fock states $|N_0 : \phi, N_1 : \phi\rangle$ with well defined atom numbers in state $|0\rangle$ and $|1\rangle$ results in:

$$|\Psi_\varphi\rangle = \sum_{N_0=0}^{N} \left(\frac{N!}{N_0!N_1!}\right)^{1/2} c_0^{N_0} c_1^{N_1} |N_0 : \phi, N_1 : \phi\rangle \tag{2.17}$$

where $N_1 = N - N_0$ and

$$|N_0 : \phi_0, N_1 : \phi_1\rangle = \frac{(\hat{b}^\dagger_{\phi_0})^{N_0}}{\sqrt{N_0!}} \frac{(\hat{a}^\dagger_{\phi_1})^{N_1}}{\sqrt{N_1!}} |\text{vac}\rangle, \tag{2.18}$$

where $\hat{b}^\dagger_{\phi_0}$ ($\hat{a}^\dagger_{\phi_1}$) creates an atom in internal state $|0\rangle$ ($|1\rangle$) and spatial mode ϕ_0 (ϕ_1). The spatial modes generally depend on N_0 and N_1 so that after the state preparation pulse, a time evolution of the condensates spatial mode sets in. This is treated in 2.2.7. For simplicity, we assume for now that the spatial mode is unchanged due to the internal state preparation $\phi_0 = \phi_1 = \phi$.

The variances of the spin components of a CSS can be calculated directly using $\Delta S_i^2 = \langle S_i^2\rangle - \langle S_i\rangle^2$. However, since the preparation constitutes only a rotation of the initial state, it is much easier to calculate the variances for

$|\Psi_{\text{ini}}\rangle = |N : \phi, 0 : \phi\rangle$ and then simply apply a coordinate transformation. The results for $|\Psi_{\text{ini}}\rangle$ are:

$$\begin{aligned}
\Delta S_z^2 &= \frac{1}{4}\left(\langle(\hat{a}^\dagger\hat{a} - \hat{b}^\dagger\hat{b})^2\rangle - \langle\hat{a}^\dagger\hat{a} - \hat{b}^\dagger\hat{b}\rangle^2\right) \\
&= \frac{1}{4}\left(\langle\hat{a}^\dagger\hat{a}\hat{a}^\dagger\hat{a} + \hat{b}^\dagger\hat{b}\hat{b}^\dagger\hat{b} - \hat{a}^\dagger\hat{a}\hat{b}^\dagger\hat{b} - \hat{b}^\dagger\hat{b}\hat{a}^\dagger\hat{a}\rangle - \langle\hat{a}^\dagger\hat{a} - \hat{b}^\dagger\hat{b}\rangle^2\right) \\
&= \frac{1}{4}\left((0^2 + N^2 - 0\cdot N_0 - N_0\cdot 0) - (0 - N)^2\right) \\
&= 0
\end{aligned} \tag{2.19}$$

and

$$\begin{aligned}
\Delta S_x^2 &= \frac{1}{4}\left(\langle(\hat{a}^\dagger\hat{b} + \hat{b}^\dagger\hat{a})^2\rangle - \langle\hat{a}^\dagger\hat{b} + \hat{b}^\dagger\hat{a}\rangle^2\right) \\
&= \frac{1}{4}\left(\langle\hat{a}^\dagger\hat{b}\hat{a}^\dagger\hat{b} + \hat{a}^\dagger\hat{b}\hat{b}^\dagger\hat{a} + \hat{b}^\dagger\hat{a}\hat{b}^\dagger\hat{a} + \hat{b}^\dagger\hat{a}\hat{a}^\dagger\hat{b}\rangle - \langle\hat{a}^\dagger\hat{b} + \hat{b}^\dagger\hat{a}\rangle^2\right) \\
&= \frac{1}{4}\left((0 + 0\cdot(N+1) + 0 + N\cdot(0+1)) - (0+0)^2\right) \\
&= \frac{N}{4}.
\end{aligned} \tag{2.20}$$

Similarly, $\Delta S_y^2 = \frac{N}{4}$.

If $|\Psi_{\text{ini}}\rangle$ is rotated by a $\frac{\pi}{2}$-pulse, a state of the form $|\Psi_\varphi\rangle = 2^{-N/2}(|0\rangle + e^{i\varphi}|1\rangle)^{\otimes N}$ is prepared. For $\varphi = 0$, the mean spin is $\langle S_x\rangle = N/2$ and $\langle S_y\rangle = \langle S_z\rangle = 0$, and the variances are $\Delta S_x^2 = 0$ and $\Delta S_y^2 = \Delta S_z^2 = N/4$. The quantum noise is evenly distributed among the spin components orthogonal to the mean spin, satisfying the Heisenberg uncertainty relation $\Delta S_y \Delta S_z = |\langle S_x\rangle|/2$. We have just derived in a more formal way the quantum projection noise, which leads to the standard quantum limit.

On the Bloch sphere, a CSS is often depicted as a vector with a fuzzy area around its tip (see e. g. figure 2.3). This area depicts the uncertainty of a measurement of the spin components orthogonal to the mean spin.

2.2.3 Squeezing factor

Quantum correlations between the atoms can reduce the variance of one spin quadrature at the cost of increasing the variance of the orthogonal one, resulting in a spin-squeezed state [13]. To quantify its usefulness for metrology, one introduces the squeezing parameter [15] $\xi^2 = N\Delta S^2_{\perp,\text{min}}/\langle S\rangle^2$, where $\Delta S^2_{\perp,\text{min}}$ is the minimal variance of the spin components perpendicular to

the mean spin $\langle \mathbf{S} \rangle$. In case $\langle \mathbf{S} \rangle$ lies along the x-axis (as for $|\Psi_0\rangle$), the squeezing parameter is

$$\xi^2 = \frac{N \Delta S^2_{\theta,\min}}{\langle S_x \rangle^2}. \tag{2.21}$$

The index θ implies that the minimal variance might not lie along the y- or z-direction but under an angle $\theta_{\min}$ with the equator. The normalization by $\langle S_x \rangle^2$ takes into account that improving interferometric sensitivity requires not only reducing noise but also maintaining high interferometer contrast $C = 2|\langle S_x \rangle|/N$.

A state with $\xi^2 < 1$ allows one to overcome the standard quantum limit in a Ramsey interferometer by a factor ξ with respect to the use of an uncorrelated ensemble of atoms [15]. Furthermore, ξ^2 is an entanglement witness, with $\xi^2 < 1$ indicating at least bipartite entanglement between the condensate atoms (see 2.2.8). In the next section, I describe how such a squeezed state can be generated through nonlinear evolution on the Bloch sphere.

2.2.4 One-axis-twisting scheme

The internal state evolution of the BEC can be described in good approximation [47] by the so called 'one-axis twisting' Hamiltonian [13]:

$$\hat{H}/\hbar = \delta \hat{S}_z + \Omega \hat{S}_\varphi + \chi \hat{S}_z^2. \tag{2.22}$$

The first term in (2.22) describes spin precession around z at the detuning δ, including BEC mean field corrections (see 2.2.6). The second term describes spin rotations around an axis $S_\varphi = (\cos\varphi)\, S_x - (\sin\varphi)\, S_y$ due to a coupling of $|0\rangle$ and $|1\rangle$ with Rabi frequency Ω and phase φ (during the pulse $\delta = 0$). It vanishes when the two-photon drive is off. The third, nonlinear term of strength χ arises due to elastic collisional interactions in the BEC. It 'twists' the state on the Bloch sphere, resulting in spin squeezing and entanglement. An intuitive understanding of how this twisting comes about can be gained in the following way: the operator $\hat{S}_z$ generates a rotation around the z-axis. $\hat{S}_z^2$ therefore generates a rotation around the z-axis which is proportional to m_z. Thus, a Fock state with $N_1 > N_0$ ($S_z > 0$) rotates faster, while a state with $N_1 < N_0$ ($S_z < 0$) rotates slower, than a state on the equator.

To create a spin squeezed state, we prepare a CSS of the form $|\Psi_0\rangle = (|0\rangle + |1\rangle)^{\otimes N}/2^{N/2}$ (figure 2.3). This is a linear combination of Fock states with different relative atom numbers and thus, evolution in time with finite nonlinear parameter χ leads to a distorted state which has reduced variance along the angle $\theta_{\min}$. To detect this reduction, we turn the state around the direction of the mean spin by exactly that angle. This is done by applying

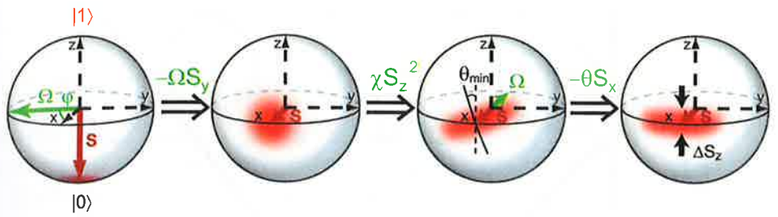

Figure 2.3: Squeezing sequence. Evolution of the BEC internal state on the Bloch sphere ($\delta = 0$ for illustration). Starting with all atoms in $|0\rangle$, a $\frac{\pi}{2}$-pulse prepares a coherent spin state with mean spin $\langle \mathbf{S} \rangle$ along x and isotropic quantum noise in the yz-plane (fuzzy red circle). Subsequent nonlinear evolution with χS_z^2 deforms the noise circle into an ellipse, creating a spin-squeezed state with reduced noise at an angle $\theta_{\min}$. To measure the spin quadrature $S_\theta = (\cos\theta)\, S_z - (\sin\theta)\, S_y$, a second pulse rotates the state around $-x$ by a variable angle θ, followed by detection of S_z.

a second pulse for a duration $\tau_\theta = \theta/\Omega$ and with a phase $\varphi = \pi$ ($\varphi = 0$) for turning clockwise (counterclockwise). Finally, we measure S_z by counting atoms in state $|0\rangle$ and $|1\rangle$. Repeating the experiment many times, one can measure $\langle S_z \rangle$ as well as ΔS_z^2.

Quantum phase diffusion. If the squeezed state is not turned prior to detection, one would measure no reduction in ΔS_z^2 but only an increase in ΔS_y^2, or equivalently in $\Delta\varphi^2$. This is sometimes referred to as *quantum phase diffusion* [93] and usually regarded as a negative effect for interferometry. Only turning the state into the correct orientation makes it useful for enhancing interferometry or atomic clocks beyond the standard quantum limit.

Oversqueezing. A typical evolution over time of the squeezing parameter ξ^2 for $\chi = const$ is shown in figure 2.4. The twisting of the Bloch sphere first results in a reduction of $\Delta S_{\theta,\min}$ and thus ξ^2. However, eventually the mean spin decreases faster than the spin noise is reduced because the uncertainty region starts to wind around the Bloch sphere (see insets in figure 2.4) and ξ^2 increases again. The state has become *oversqueezed*.

An essential feature of our experiment is therefore the control of the nonlinearity. It should be active only during a well chosen best squeezing time to avoid oversqueezing. This is described in section 2.2.6

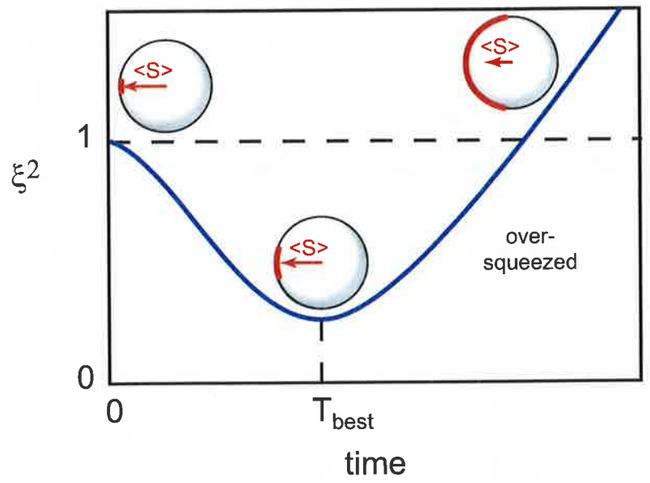

Figure 2.4: Oversqueezing. Typical evolution of a coherent spin state under a constant nonlinearity. The squeezing parameter ξ^2 decreases, reaches a minimum at the best squeezing time T_{best} and then increases again until it becomes larger than 1. The state is then oversqueezed. The insets show Bloch spheres for different times, looking from the north pole toward the sphere center, demonstrating the decrease of $\langle S \rangle$ over time.

2.2.5 Schrödinger cat state preparation

For long times, the quantized nature of the spin can no longer be neglected. In fact, it exists a revival time t_{rev} where the original coherent spin state is recovered [97]. To easily see this, let us for now consider $\Omega = \delta = 0$ (if $\delta \neq 0$ the coherent state is still recovered at t_{rev}, but with an overall phase shift); the Hamiltonian is then simply $\hat{H} = \hbar\chi\hat{S}_z^2$.

An initial CSS with $\varphi(t=0) = 0$ evolves during the time $t_{\text{rev}} = \pi/\chi$ into

$$|\Psi(t)\rangle = e^{-i\chi\hat{S}_z^2 t_{\text{rev}}}|\Psi_0\rangle = e^{-i\pi\hat{S}_z^2}|\Psi_0\rangle. \tag{2.23}$$

Suppose we have an even number of particles, then $m_z \in \{0, \pm1, \pm2, ..., \pm N/2\}$, and m_z^2 has the same parity as m_z. We can therefore replace $\hat{S}_z^2$ by $\hat{S}_z$ in equation (2.23) and get

$$|\Psi(t)\rangle = e^{-i\pi\hat{S}_z}|\Psi_0\rangle = |\Psi_{\frac{\pi}{2}}\rangle. \tag{2.24}$$

For an odd number of particles, however, $m_z \in \{\pm\frac{1}{2}, \pm\frac{3}{2}, ..., \pm N/2\}$ and we can replace $\hat{S}_z$ by $\hat{p} + \frac{1}{2}$ where $\hat{p}$ has eigenvalues $m_p \in \{0, \pm1, \pm2, ..., \pm\frac{N\mp1}{2}\}$.

We then get

$$|\Psi_\varphi(t)\rangle = e^{-i\pi\hat{S}_z^2}|\Psi_0\rangle = e^{-i\pi/4}e^{-i\pi(\hat{p}^2+\hat{p})}|\Psi_0\rangle = e^{-i\pi/4}|\Psi_0\rangle. \tag{2.25}$$

The last equality arises again because m_p^2 has the same parity as m_p, and therefore $m_p^2 + m_p$ is always even.

Both, for even and odd atom numbers, a coherent state is recovered at the time t_{rev}, but with a phase shift depending on the atom number. In a simple picture, the Fock states, which the CSS is composed of, rotate with a different precession rate, depending on m_z. However, at the time t_{rev}, all Fock states have rotated a multiple of 2π (plus an additional phase shift for even N) and a CSS is recovered.

At the time $t_{\text{cat}} = t_{\text{rev}}/2 = \pi/(2\chi)$, half of the Fock states have made one or several full rotations, while the other half ends up with an effective phase shift of π. The state at this time is a Schrödinger cat state of the form

$$|\Psi_{\text{cat}}\rangle = \frac{1}{2^{(N+1)/2}}\Big((|0\rangle + |1\rangle)^{\otimes N} + (|0\rangle - |1\rangle)^{\otimes N}\Big), \tag{2.26}$$

which means that either all atoms are in the symmetric or all atoms are in the anti-symmetric superposition. The same process responsible for spin squeezing can thus also produce a maximally entangled cat state [16]. However, already a few particles lost on average during the preparation time result in a collapse of the cat state into a statistical mixture of the two CSS of which it is composed. This is an example of the general rule that the more a state is entangled, the more it is sensitive to decoherence.

2.2.6 Interaction control via wave function overlap

In the stationary two-mode model the nonlinear coefficient [47]

$$\chi = \frac{1}{2\hbar}\left(\partial_{N_0}\mu_0 + \partial_{N_1}\mu_1 - \partial_{N_1}\mu_0 - \partial_{N_0}\mu_1\right)_{\langle N_0\rangle,\langle N_1\rangle} \tag{2.27}$$

depends on derivatives of the chemical potentials

$$\mu_j = \langle\phi_j|h_j|\phi_j\rangle + \sum_{k=0,1} g_{jk}N_k\int dr^3|\phi_j|^2|\phi_k|^2 \tag{2.28}$$

of the two BEC components with respect to the atom numbers, evaluated at the mean atom numbers $\langle N_0\rangle = \langle N_1\rangle = N/2$ after the $\frac{\pi}{2}$-pulse. Here, h_j is the single-particle Hamiltonian including kinetic energy and the trapping potential. The interaction strength $g_{jk} = 4\pi\hbar^2 a_{jk}/m$ between atoms in $|j\rangle$ and $|k\rangle$ depends on the corresponding s-wave scattering length a_{jk}.

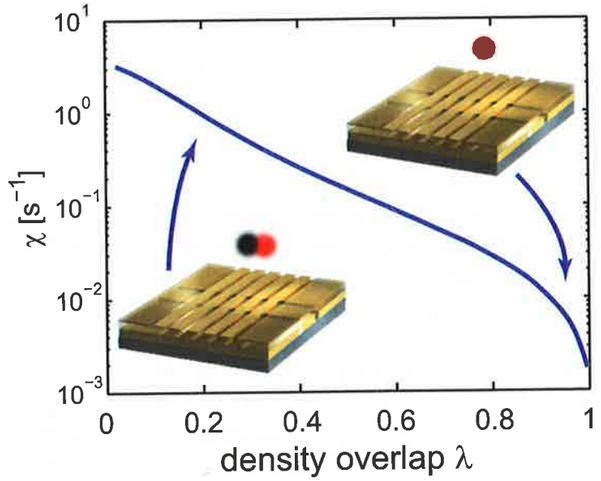

Figure 2.5: Control of the nonlinearity χ on the atom chip. χ depends on the difference of intra- and inter-state atomic interactions. Its dependence on the normalized density overlap λ of the two BEC components is shown, calculated from stationary mode functions in potentials of increasing separation.

If we neglect the dependence of the spatial wave functions on the atom numbers we end up with a simpler expression

$$\begin{aligned} \chi &= \frac{1}{2\hbar}\Big(U_{00} + U_{11} - 2U_{01}\Big) \\ \text{with} \qquad U_{jk} &= g_{jk}\int dr^3 |\phi_j|^2 |\phi_k|^2. \end{aligned} \tag{2.29}$$

As already mentioned in section 1.4.2, for our states, the three scattering lengths are close, $a_{00} : a_{01} : a_{11} = 100.4\,a_0 : 97.7\,a_0 : 95.0\,a_0$. If the two BEC modes overlap spatially, $\phi_1 = \phi_0$, the crossed terms in equations (2.27) and (2.29) with the minus sign compensate the direct terms with the plus sign. Thus, by default, $\chi \approx 0$.

There are two ways to increase χ: one can change the inter-state scattering length a_{01} with the help of a Feshbach resonance as was done parallel to our work in an experiment of M. Oberthaler's group in Heidelberg [26]. However, they used a different state pair and for our clock states no convenient Feshbach resonance exists. The second method – used in our experiment – is to control the overlap of ϕ_0 and ϕ_1 with a state-dependent trapping potential.

By spatially separating the two modes, the crossed terms $\partial_{N_1}\mu_0$ and $\partial_{N_0}\mu_1$ (the overlap integral (2.29) with $j \neq k$) are set to zero and thus $\chi > 0$. In figure 2.5, χ is shown as a function of the normalized density overlap

$$\lambda = \frac{\int dr^3 |\Phi_0|^2 |\Phi_1|^2}{\sqrt{\int dr^3 |\Phi_0|^4 \int dr^3 |\Phi_1|^4}}. \tag{2.30}$$

For this figure, we first solve the coupled two-component Gross-Pitaevskii equations in traps of increasing separation for our experimental parameters (see section 3.8). For the stationary mode functions thus obtained, λ and χ are calculated. Controlling the overlap allows us to tune χ in our experiment by three orders of magnitude.

Derivation of the nonlinear term χ

Expression (2.29) can be derived directly in the following way: We start with the stationary GPE (1.26) for a single-state BEC. Multiplying 1.26 with ϕ^*, integrating over space, and division by N results in

$$\mu = \int dr^3 \phi^* \Big(-\frac{\hbar^2}{2m}\nabla^2 + V_{\text{ext}}\Big)\phi + gN\int dr^3 |\phi^4| \tag{2.31}$$

Assuming once again that the wave function dependence on N is negligible and using $E = \int \mu\, dN$, we derive the Hamiltonian

$$\begin{aligned} H &= N\int dr^3 \phi^* \Big(-\frac{\hbar^2}{2m}\nabla^2 + V_{\text{ext}}\Big)\phi + \frac{1}{2}N^2 g\int dr^3 |\phi|^4 \\ &= Nh_0 + \frac{1}{2}N^2 U \end{aligned} \tag{2.32}$$

This calculation can be extended to a system with two internal states and yields

$$H = Nh_0 + \frac{1}{2}N_0^2 U_{00} + \frac{1}{2}N_1^2 U_{11} + N_0 N_1 U_{01} \tag{2.33}$$

The last term describes inter-state scattering between distinguishable scattering partners and therefore does not contain the factor $\frac{1}{2}$. We now replace $N_0 = \frac{N}{2} - S_z$ and $N_1 = \frac{N}{2} + S_z$ and get

$$\begin{aligned} H &= Nh_0 + \frac{1}{2}\Big(\frac{N^2}{4} - NS_z + S_z^2\Big)U_{00} \\ &\quad + \frac{1}{2}\Big(\frac{N^2}{4} + NS_z + S_z^2\Big)U_{11} + \Big(\frac{N^2}{4} - S_z^2\Big)U_{01} \\ &= Nh_0 + \frac{N^2}{8}\Big(U_{00} + U_{11} + 2U_{01}\Big) \\ &\quad + \frac{NS_z}{2}\Big(U_{11} - U_{00}\Big) + \frac{S_z^2}{2}\Big(U_{11} + U_{00} - 2U_{01}\Big). \end{aligned} \tag{2.34}$$

The first term in (2.34) is the kinetic and potential energy of the non-interacting condensate, the second term is a total energy offset depending on the total atom number N. The third term is a differential energy between states $|0\rangle$ and $|1\rangle$ which leads to an atom number dependent precession of the spin. In a Ramsey sequence, this term translates a fluctuation in N due to preparation fluctuations and losses into phase noise. The fourth term finally, is nonlinear and the same as in equation (2.29).

2.2.7 Beyond the stationary two-mode model

The stationary two-mode model provides physical insight into the origin of spin squeezing. However, since our method of controlling χ involves dynamically splitting and recombining the two states, quantitative predictions can not be made with this simple model and a theory which takes into account the external degrees of freedom is needed. Our collaborators Alice Sinatra and LI Yun from the Laboratoire Kastler Brossel at the ENS in Paris have developed such a theory and applied it to our experiment [47]. They have also considered the influence of losses [94, 47] and technical noise on the squeezing. In the following, I briefly outline their theory.

Dynamical model

For the dynamical two-mode model [47] we again decompose a condensate state into a superposition of Fock states

$$|\Psi(t)\rangle = \sum_{N_0=0}^{N} \left(\frac{N!}{N_0!N_1!}\right)^{1/2} c_0^{N_0} c_1^{N_1} |N_0 : \phi_0, N_1 : \phi_1\rangle. \tag{2.35}$$

Compared with (2.17) however, we now allow for different, time dependent spatial modes

$$|N_0 : \phi_0, N_1 : \phi_1\rangle \rightarrow e^{-iA(N_0,N_1,t)/\hbar} \times |N_0 : \phi_0(N_0, N_1, t), N_1 : \phi_1(N_0, N_1, t)\rangle. \tag{2.36}$$

The time evolution of each Fock state can be split into a phase evolution and an evolution of the spatial mode. The spatial wave functions solve the coupled Gross-Pitaevskii equations

$$i\hbar\frac{\partial\phi_j}{\partial t} = \left(h_j + N_j g_{jj}|\phi_j|^2 + N_k g_{jk}|\phi_k|^2\right)\phi_j \tag{2.37}$$

with $\phi_0(t=0) = \phi_1(t=0) = \phi_0$ and the phase factor solves

$$\frac{dA}{dt} = -\sum_{j,k=0,1} \frac{1}{2} N_j N_k g_{jk} \int d^3r |\phi_j|^2 |\phi_k|^2 \tag{2.38}$$

with $(j,k) = (0,1)$. This set of equations can be solved numerically and takes into account the spatial dynamics of the two modes as well as the internal state dynamics and specifically their dependence on atom numbers. The approximation made here is that only the two condensate modes are occupied and thermal occupation of orthogonal modes is not included. This theory is therefore only strictly valid for $T = 0$.

Modulus-phase approach

Although solving equations (2.37) and (2.38) can in principle be done, for large atom numbers and in three dimensions it soon becomes a computationally demanding task. For an analytical solution one utilizes the fact that for a coherent spin state with large atom number, only Fock states around $|\overline{N_0}, \overline{N_1}\rangle$ contribute significantly. We split the spatial wave function into a modulus and phase and use the fact that the density distribution depends only weakly on atom number. Thus, the variation of $|\phi_j|$ over the distribution of N_j can be neglected:

$$\phi_j(N_0, N_1, t) = |\phi_j(\overline{N_0}, \overline{N_1}, t)|e^{i\varphi_j(N_0,N_1,t)}. \tag{2.39}$$

We approximate the variation of the phase by a linear expansion around $\overline{N_j}$:

$$\phi_j(N_0, N_1, t) \simeq \overline{\phi_j}(t) \exp\Big(i \sum_{k=0,1} (N_k - \overline{N_k}) \frac{\partial\varphi_j}{\partial N_k}\Big|_{(\overline{N_0},\overline{N_1},t)}\Big) \tag{2.40}$$

where $\overline{\phi_j}(t) = \phi_j(\overline{N_0}, \overline{N_1}, t)$. The modulus-phase approach thus takes into account the dependence of the condensate wave function phase on the particle number, which is exactly the origin of spin squeezing. The expectation values and variances of the spin operator (2.12) for the coherent state can now be expressed in terms of only six quantities: the two spatial mode functions for the mean atom numbers $\overline{\phi_j}$ and the four phase derivatives $\frac{\delta\varphi_j}{\delta N_k}$. For the simulations of our experiment it is sufficient to evolve a few (usually 5) coupled GPE (2.37) for different values of N_0 and N_1 around $\overline{N_0} = \overline{N_1} = N/2$ and then numerically calculate the phase derivatives.

Phase noise due to losses

Particle losses fundamentally limit the amount of squeezing which can be achieved. The 'experimentalist's reason' for this is simple: because losses are statistical processes they impose an additional shot noise of the order of

$$\Delta S_z^2(t) \sim N_0(t=0)p_0(t)[1-p_0(t)] + N_1(t=0)p_1(t)[1-p_1(t)], \tag{2.41}$$

where $N_j(t=0)p_j(t)$ is the number of lost atoms in state $|j\rangle$ at some time t with $p_j(t)$ the probability for loosing an atom during the time t.

In a more formal way [94, 47], one can evolve the density matrix with a Monte-Carlo wave function approach [95], where losses are modeled by quantum jump operators. In the interaction picture, where the jump operator depends on time, the effect of such a quantum jump at time t_{jmp} on a coherent spin state is a sudden transfer of the CSS into another with a reduced mean atom number and a random phase shift proportional to ςt_{jmp}, where ς is a function of U_{00}, U_{11}, and U_{01} (why a change in atom number results in a phase shift can be seen in equation (2.34)). This model can be solved analytically for one-body losses and for two- and three-body losses within a 'constant loss-rate approach', which is valid for times where only a small fraction of the atoms are lost. For a symmetric state ($\overline{N_0} = \overline{N_1}$) and equal loss rates $\Gamma^{(m)}$ (for the two states and for all m-body losses), the reduction of the squeezing factor, compared to the non-loss case ($\xi_0^2(t)$), is

$$\xi^2(t) = \xi_0^2(t)\Big(1 + \frac{\Gamma_{sq} t}{3\xi_0^2(t)}\Big), \tag{2.42}$$

with $\Gamma_{sq} = \sum_m m\Gamma^{(m)}$ and $\Gamma^{(m)} = (N/2)^{m-1} K_m \int d^3r |\phi|^{2m}$ where K_m is the m-body rate constant (see 1.4.3). $\Gamma_{sq} t$ is the lost fraction of atoms after a time t. This confirms our initial guess that the squeezing is limited by losses with $\xi^2 \geq \Gamma_{sq} t_{\text{best}}/3$, where t_{best} is the best squeezing time.

Finite temperature effects

The loss of phase coherence of a one-component homogeneous BEC due to finite temperature effects has been calculated in [96]. From this, one can estimate that the thermal contribution to the variance of the relative phase in a bimodal BEC grows quadratically in time $\Delta\varphi^2(t) = \Delta\varphi_0^2 + A_T t^2$, with $\Delta\varphi_0^2 = \Delta\varphi^2(t=0)$. The coefficient A_T depends on the temperature, on the interaction strength and on the number of particles. The phase spreading due to the nonlinear atomic interaction is also quadratical in time [97] $\Delta\varphi^2(t) = \Delta\varphi_0^2 + (2\Delta S_{z,0}\chi t)^2$, with $\Delta S_{z,0} = \Delta S_z(t=0)$ the uncertainty in S_z of the initial state. To estimate the relative importance of finite temperature, we can thus compare A_T with $2\Delta S_{z,0}\chi$.

In our squeezing experiment $\chi = 0.49\,\text{s}^{-1}$, $\Delta S_{z,0} = \sqrt{1250}/2 = 17.5$, and $k_B T \ll \mu$. In these conditions, we estimate that thermal effects are negligible. The theory of finite temperature effects on squeezing is still under development, for example A_T could be – at least quantitatively – different for trapped BECs. However, since we work with very pure condensates with

$k_B T \ll (k_B T_C, \mu)$, we are confident that phase spread due to temperature has only a minor effect in our experiments.

2.2.8 Relation between squeezing and entanglement

The density matrix of any non-entangled, separable state of N atoms can be written in the form

$$\rho = \sum_k p_k \rho_1^{(k)} \otimes \rho_2^{(k)} \ldots \otimes \rho_N^{(k)} \tag{2.43}$$

where $\rho_i^{(k)}$ is the density matrix of the i^{th} particle in the k^{th} therm of the weighted sum. A state is m-particle entangled if ρ cannot be decomposed into a sum where each density matrix involves less than m particles. In other words, the sum contains at least one m-particle density matrix $\rho_{i\ldots i+m}^{(k)}$.

It is shown in [16] that a spin state satisfying $\xi^2 < 1$ is at least bi-partite entangled. In [46], a more general method for the identification of m-particle entanglement through measurement of the collective variables $\Delta S_{\theta,\min}^2$ and $\langle S_x\rangle^2$ is deduced: using the Heisenberg uncertainty relation $\Delta S_y \Delta S_z \geq \langle S_x\rangle/2$ and $\langle S_x^2\rangle + \langle S_y^2\rangle + \langle S_z^2\rangle \leq S(S+1)$, one can derive

$$\Delta S_{\theta,\min}^2 \geq \frac{1}{2}\Big(S(S+1) - \langle S_x\rangle^2 - \sqrt{[S(S+1) - \langle S_x\rangle^2]^2 - \langle S_x\rangle^2}\Big). \tag{2.44}$$

For large S and $\langle S_x\rangle$ this inequality gives an approximate bound for the maximum squeezing achievable in a spin S system. The main result of [46] is that in a system of N spin-$\frac{1}{2}$ particles, for a measured set $\Big(\langle S_x\rangle, \Delta S_{\theta,\min}^2\Big)$, there is a minimum spin S satisfying equation (2.44) and the system is thus at least $(2S+1)$-particle entangled. For low entanglement (S small) the analytical formula (2.44) does not give a tight bound and a numerical calculation produces the corresponding limit (see figure 2.6).

2.3 State tomography

To measure the degree of spin squeezing for a given state, it is sufficient to measure its mean spin and the spin fluctuations along the angle $\theta_{\min}$. However, much more information about the state can be gained by measuring the mean spin and its variance not only along one direction but along many angles $\theta_0 \leq \theta < (\theta_0 + \pi)$. From such a state tomography one can gain a complete description of the state in the form of a quasi-probability distribution.

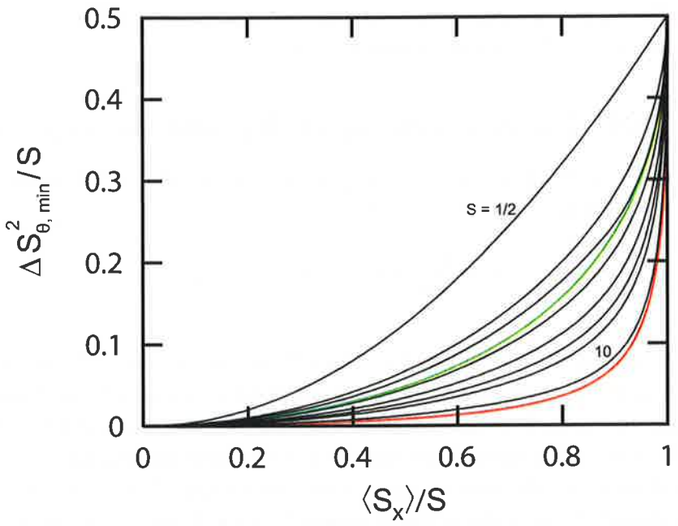

Figure 2.6: Maximal squeezing for different values of S. Curves indicating the maximal possible reduction in spin variance as a function of contrast $\langle S_x\rangle/S$ for different spins S. The black lines are numerical calculations for $S = (\frac{1}{2}, 1, \frac{3}{2}, 2, 3, 4, 5, 10)$ (top to bottom), the colored lines are the solutions of the analytical formula (2.44) for $S = \frac{1}{2}$ (green) and $S = 10$ (red). The analytical approximation is close to the numerical calculation only for large S. If a measured data point $\left(\langle S_x\rangle, \Delta S^2_{\theta,\min}\right)$ lies below a (black) S-line it implies that the ensemble is at least $(2S+1)$-particle entangled. Figure adapted from [46].

Wigner function

The description of mixtures and fluctuations usually requires the use of the density operator ρ which provides the most general description of a quantum system. There exists however a different but completely equivalent description in phase space in the form of the quasi-probability distributions such as the Glauber-Sudarshan P distribution or the Wigner distribution (or Wigner function) [14, 98, 99]. For an harmonic oscillator the Wigner function is defined as

$$W(q,p) = \frac{1}{\pi\hbar}\int_{-\infty}^{+\infty} \langle q-y|\rho|q+y\rangle e^{i2py/\hbar}dy, \tag{2.45}$$

where q and p are position and momentum quadratures, respectively. For a pure state $\rho = |\Psi\rangle\langle\Psi|$ it becomes

$$W(q,p) = \frac{1}{\pi\hbar}\int_{-\infty}^{+\infty} \Psi(x+y)\Psi^*(x-y)e^{i2py/\hbar}dy. \tag{2.46}$$

Its physical meaning is straight forward: although the Wigner function itself can have negative values, its marginals are always positive and correspond to probability distributions. To find the quadrature component distribution $p(x,\theta)$ along an angle θ one simply integrates the Wigner function along a direction perpendicular to θ [100]:

$$p(x,\theta) = \int_{-\infty}^{+\infty} W(x\cos\theta - y\sin\theta, x\sin\theta + y\cos\theta)dy. \tag{2.47}$$

On the other hand, when the probability functions $p(x,\theta)$ for all angles within a π-interval are known, the Wigner function can be calculated as [100]

$$W(q,p) = \frac{1}{4\pi^2}\int_{-\infty}^{+\infty} dx \int_{-\infty}^{+\infty} d\eta \int_{\theta_0}^{\theta_0+\pi} d\theta\, p(x,\theta)|\eta| \exp\left(i\eta(x - q\cos\theta - p\sin\theta)\right). \tag{2.48}$$

This is the inverse Radon transform [101], which is well known from classical tomography (for example from image reconstruction in X-ray tomographs). It was for example employed to reconstruct the Wigner function of squeezed light using optical homodyne detection [102].

The continuous Wigner function, as described above, is defined in a 2-dimensional, continuous variable phase space. To describe a quantized spin 'living' on the Bloch sphere, one generally needs to utilize a discrete Wigner formalism [103, 104]. However, for large atom numbers and coherent or mildly squeezed spin states (as it is the case in our experiment), the Bloch sphere can locally be approximated by a plane and the spin components as continuous variables (see figure 2.7) so that equation (2.48) is suitable to reconstruct the approximate Wigner functions.

After we have produced the squeezed spin state we can thus not only measure $\Delta S^2_{\theta,\min}$ but the probability distribution $p(S_\theta)$ along many angles θ in the yz-plane and use this information to reconstruct the Wigner function

$$W(S_y,S_z) = \frac{1}{4\pi^2}\int_{-\infty}^{+\infty} dS_\theta \int_{-\infty}^{+\infty} d\eta \int_{\theta_0}^{\theta_0+\pi} d\theta\, p(S_\theta)|\eta| \exp\left(i\eta(S_\theta - S_y\cos\theta - S_z\sin\theta)\right). \tag{2.49}$$

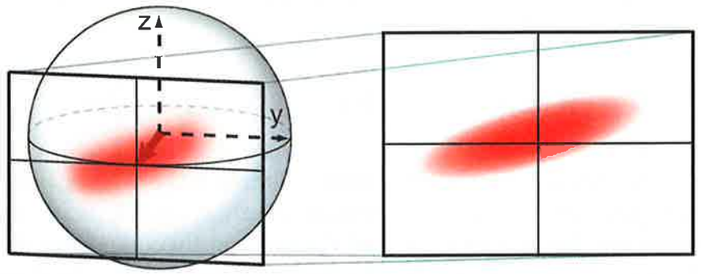

Figure 2.7: Local Bloch sphere approximation. For large atom numbers and if the spin state does not 'wrap around' the Bloch sphere too much, the Bloch sphere can be locally approximated by a tangent plane and the spin components as continuous variables. In this plane the Wigner function can be reconstructed using the inverse Radon transformation (2.49).

In practice we measure $p(S_\theta)$ only for a discrete set of angles, with limited atom number resolution (thus limited resolution of S_θ), and with a limited amount of data per angle. This imposes limits on the reconstruction accuracy which will be discussed in chapter 4.

Quantum state tomography is of interest because it gives access to measures of entanglement, such as the quantum Fisher information [105, 106], which characterize a more general class of states (including states with $\xi^2 > 1$) that can be used to overcome the standard quantum limit [106].

Chapter 3

Experimental setup

Our experimental setup is similar to previous and existing atom chip experiments in the groups of Jakob Reichel and Philipp Treutlein. Many details can therefore be found in the PhD theses of previous group members. The fabrication and characterization of our microwave atom chip are covered in Philipp Treutlein's [49] and Pascal Böhi's [45] theses. The laser and vacuum systems are treated in great detail in the diploma thesis of Johannes Hofrogge [107], who built them together with myself. Pascal Böhi also describes the computerized control of our experiment and the hardware used to generate radiofrequency and microwave currents and radiation in our experiment. For completeness, I briefly cover all of these topics. The main part of this chapter is dedicated to the absorption imaging system used to achieve the high atom number resolution, needed to experimentally demonstrate spin squeezing. In the last part, I present a typical experimental sequence for the production of mesoscopic BECs and lifetime measurements in the trap used for the squeezing experiments.

3.1 Microwave atom chip

The atom chip used in our experiment was designed and built by Philipp Treutlein and Pascal Böhi. Two features, employed here for the first time, make it one of the technically most advanced atom chips in existence: first, two layers of gold, separated by a thin insulating layer, allow for crossing wires and thus more flexibility in trap design. Second, integrated coplanar waveguides (CPWs) allow us to inject microwave currents into the chip and use the CPW near-field for state-selective manipulation of the atoms.

A photograph of the chip is shown in figure 3.1 and a drawing of the wire layout in figure 3.2. An AlN base chip provides mechanical stability and

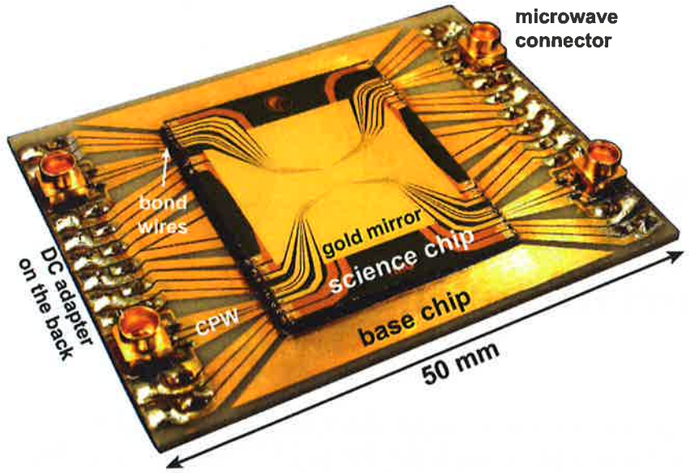

Figure 3.1: Microwave atom chip. Microwave atom chip assembly, including the base chip, the science chip, and electrical DC and microwave connectors, before it is glued to the vacuum glass cell.

easy connection to DC current sources through the socket adapters, which are soldered onto the chip from the back. Microwave sources are connected from the front. The electroplated gold wires have a height of 12 μm and can carry DC currents of up to 10 A.

A spacer chip is glued onto the base chip, and the so called *science chip* is glued onto this spacer chip. Both have the same dimensions and are cut from a 525 μm thick high-resistivity Silicon wafer. The science chip carries two layers of metalization, separated by a layer of polyimide which is 6 μm thick. The polyimide provides not only electrical insulation between the two gold layers but also planarization to reduce the bumpiness of the upper layer. The lower gold layer has a thickness of 5 μm and is fabricated in the same way as the wires on the base chip. The wires on this layer carry static currents for magnetic Ioffe-Pritchard and dimple traps. The upper layer is fabricated with a lift-off technique and has a thickness of only 1 μm. Some wires on this layer form CPWs but can also carry DC currents of up to about 100 mA. In the experiment reported here, we use a 5-wire structure. The central three wires form the CPW indicated in figure 3.2 while the outer two wires can be used for additional tuning of the position of the static magnetic trap. The upper layer also features a large gold mirror which is used for the mirror MOT in the first stages of the experimental cycle. Base and science chip are electrically connected through gold bond wires.

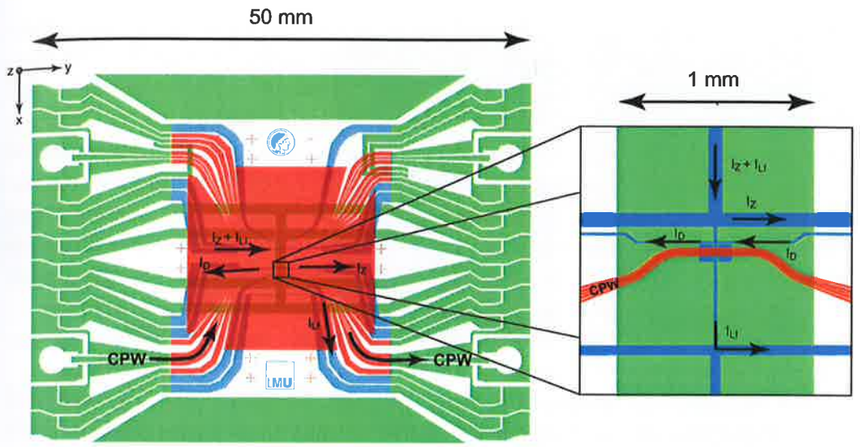

Figure 3.2: Wire layout. The wire layout on the base chip (green) and the lower (blue) and upper layer (red) of the science chip. The right panel shows a zoom into the experiment region, omitting the gold mirror. There are several waveguide structures on the chip, but for the experiments reported in this thesis, only the one indicated is used. The black arrows indicate the main DC currents used in our experimental sequence, as described in section 3.8.

3.1.1 Characterization of the microwave near-field

Using the Biot-Savart law, it is straightforward to calculate magnetic fields produced by static currents and thus simulate the expected magnetic trap positions and frequencies with high accuracy (within a few percent). The simulation of the microwave near-field proves to be much more difficult. Since the transverse CPW dimensions and the distance of the atoms from the wires are much smaller than the microwave wavelength ($\lambda = 4.4\,\mathrm{cm}$ for $f_{\mathrm{mw}} = 6.8\,\mathrm{GHz}$ in vacuum), we can neglect retardation effects and calculate the microwave field around the CPW from the microwave current distribution in the wires in a similar way to the static fields. The difficulty lies in determining the exact current distribution, since microwave currents can be induced in the adjacent wires or the wires on the lower layer of the science chip. This and the curvature of the CPW can furthermore lead to an asymmetric current distribution in the CPW itself. Also, the skin effect leads to an inhomogeneous current distribution in each wire.

We have devised a method to measure the microwave field distribution around the waveguide, using the cold atoms themselves as probes [64, 45].

Briefly, we release a cloud of thermal atoms in state $|0\rangle$ close to the waveguide and let it expand until it fills an extended region around the guide. We then apply a short microwave pulse in the CPW, resonant with an atomic transition. We thus coherently transfer some population into the $F = 2$ states. The transfer rate at any given point in space depends on the microwave field strength at that point which therefore can be deduced by state-selective detection of the atoms. The data quality can be improved by scanning the microwave amplitude to record Rabi oscillations in space. By repeating such measurements with a static magnetic quantization field pointing along each coordinate axis, and with the microwave frequency adjusted to drive the π, σ^+, or σ^- transition (for a total of 9 data sets), we can reconstruct the complete microwave field distribution in the region filled by the atoms.

We compare the measured field to the field calculated from the assumed current distribution, and adjust the latter to maximize agreement. A good match can be achieved by assuming a small asymmetry in the microwave currents on the CPW and small induced currents in the two adjacent wires as well as in the lower science chip layer. We have also simulated the microwave propagation on the CPW, including the lower science chip layer, using the software *Sonnet* and find good agreement between this simulation and the experimentally found current distribution. As an example, figure 3.3 shows the measured and simulated distributions of the x-component of the microwave magnetic field.

3.2 Vacuum system

Experiments with cold atoms require ultra-high vacuum (UHV) conditions to minimize atom loss due to collisions with background gas. The high trap frequencies achievable with atom chips allow for fast evaporative cooling and thus reduce the vacuum requirements compared to non-chip setups. Typically, pressures of $p < 10^{-9}$ mbar yield lifetimes of a few seconds.

Glass cell. Our atom chip is an integral part of the vacuum chamber. It is glued to a cubic glass cell (see figure 3.4) which in turn is glued to a glass-to-metal adapter. For best vacuum compatibility we use a UHV certified epoxy glue[1]. This configuration is very compact, since no additional electrical vacuum feedtroughs are needed. The atom chip is oriented upside-down so that released atoms can fall freely away from the chip surface. The glass cell is rotated slightly with respect to the science chip axis in order to reduce

[1]Epo-Tek 353ND

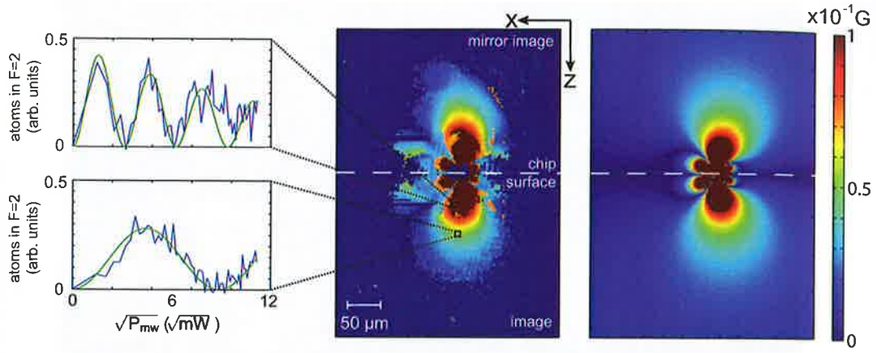

Figure 3.3: Measured (left) and simulated (right) microwave field distribution for the x-component of the microwave magnetic near-field around the waveguide (static quantization field in x-direction and a microwave resonant with the π-transition used). Since the images are recorded with a tilted imaging beam, the cloud is imaged directly (bottom) and as a reflection from the chip surface (top). The insets show the measured population in state $|2, -1\rangle$ as a function of the microwave power injected into the waveguide (blue: data, green: fit used to calculate left image). Figure adapted from [45].

interference fringes during the imaging of the atoms. Additionally, the glass cell is anti-reflection coated on the outside. A water cooled copper block is glued to the back of the base chip, containing a U-shaped copper wire which can carry several tens of amperes and is used for producing the magnetic quadrupole field for the first MOT.

Pumps and Gauge. The glass-to-metal adapter is connected through 35 mm tubing to a Ti-sublimation pump, a 40 l/s ion pump, and an extractor pressure gauge (see figure 3.5). During normal operation, the ion pump keeps the pressure at a level of a few times 10^{-10} mbar. The Ti-sublimation pump is used only rarely (every few months), when the pressure has built up above 8×10^{-10} mbar. The pressure gauge is switched off during the squeezing experiments since the light emitted by its glowing filament is detected by our camera and causes additional imaging noise.

Dispenser. As a rubidium source we use dispensers located in the glass part of the glass-to-metal adapter. We currently have two dispensers from

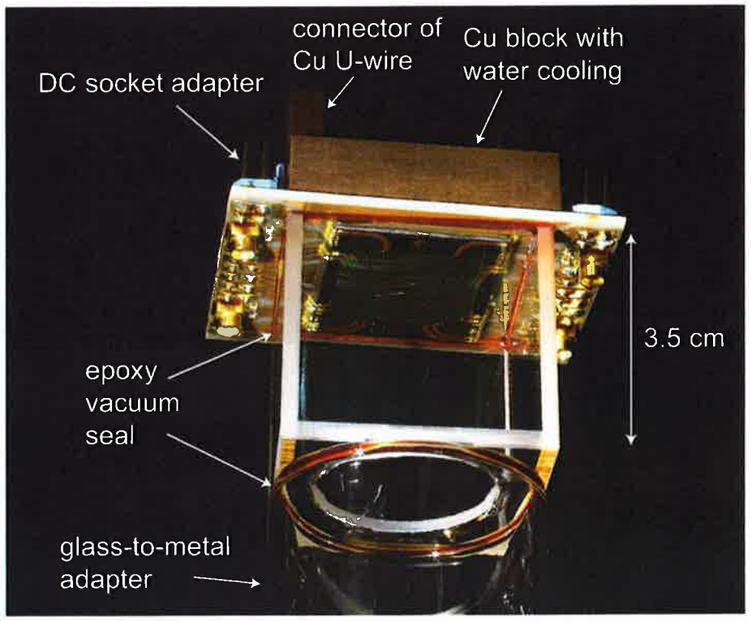

Figure 3.4: Glass cell with atom chip. The atom chip is glued to a glass cell, which in turn is glued to a glass-to-metal adapter. A copper block glued to the back of the base chip provides water cooling and a thick wire used for the first MOT. Figure adapted from [49]

SAES Getters[2] and one from Alvatec[3] built into the experiment. The dispensers contain rubidium chromate mixed with a reducing agent (SAES) or RbIn alloy (Alvatec), and release rubidium upon heating by sending a current of approximately four amperes through them. The dispensers are not isotope enriched, i. e. they contain only 28 % ^{87}Rb and 72 % ^{85}Rb [50]. Turning on a dispenser after a pause of more than a week causes the pressure in the vacuum chamber to rise briefly above 10^{-9} mbar because contaminations, which accumulated during this time on the dispenser, are released. However, since rubidium acts as a getter material, when the dispenser is regularly used, the pressure falls back to the usual level of a few times 10^{-10} mbar.

The two SAES dispensers are mounted such that the opening of one is facing toward the chip center whereas the opening of the other faces the wall

[2]SAES Getters RB/NF/3,4/12FT10+10
[3]Alvatec AS-RbIn-5-F

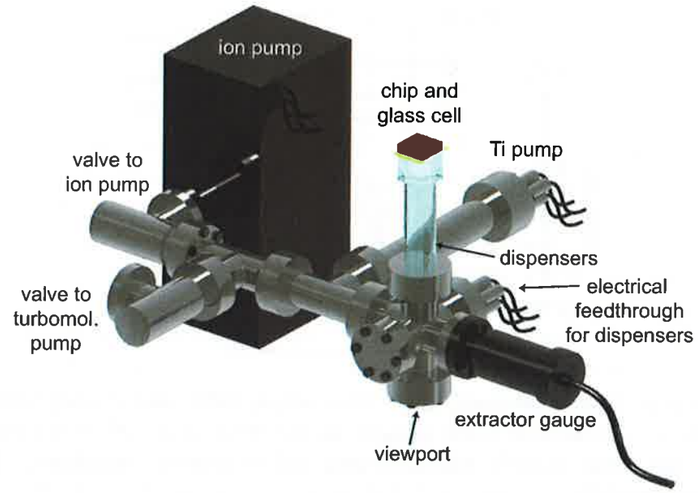

Figure 3.5: Vacuum system. The vacuum system is evacuated by a Ti-sublimation pump and an ion pump, the pressure is monitored through an extractor gauge. The front valve can be connected to a turbomolecular pump for initial evacuation and bakeout. Figure adapted from [49].

of the glass-to-metal adapter. We have used the latter at a current of 3.8 A for several hours daily in the last 3 years, and there is no sign of depletion, so far.

3.3 Laser system

In our experiments with cold ^{87}Rb atoms we use laser light close to the D_2 line ($\lambda = 780.2\,\text{nm}$, natural line width of $\Gamma = 2\pi \times 6.1\,\text{MHz}$) to cool, optically pump, and detect the atoms. For each of these steps, light with a different frequency, driving a different hyperfine transition, is required, as shown in figure 3.6. The cooling light for the MOT is red-detuned by $2\,\Gamma$ with respect to the $F = 2 \leftrightarrow F' = 3$ transition. In the molasses, the detuning is increased to $12\,\Gamma$. For imaging, the same hyperfine transition is driven resonantly. If during cooling or imaging atoms are off-resonantly excited into $F' = 2$ and fluoresce into an $F = 1$ state, they are repumped using the $F = 1 \leftrightarrow F' = 2$ transition until they fall back into $F = 2$, where they rejoin the cooling cycle. After optical cooling, in order to magnetically trap and manipulate the atoms, we optically pump them into the state $|F = 1, m_F = -1\rangle$, using

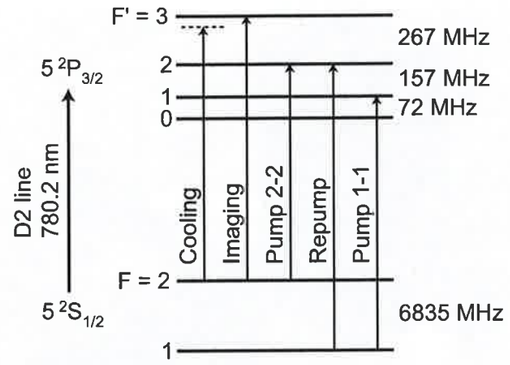

Figure 3.6: Laser frequencies. The cooling light used during MOT and molasses is red-detuned with respect to the $F = 2 \leftrightarrow F' = 3$ transition whereas all other light is resonant with the indicated transitions. Figure adapted from [49].

σ^- light on the $F = 2 \leftrightarrow F' = 2$ and $F = 1 \leftrightarrow F' = 1$ transitions (see also section 3.7).

We use three diode lasers, two of which are grating stabilized [108] and locked via Doppler-free saturation spectroscopy [109] to the D_2 line (see figure 3.7). The cooling, imaging, and 'Pump 2-2' light are derived from two lasers in a *master-slave* configuration. The *master* laser is locked to the $F = 2 \leftrightarrow F' = 2, 3$ crossover resonance and some light is branched off to be used for the 'Pump 2-2' light. This light is passed twice through an acousto-optic modulator (AOM) to decrease its frequency by 133.5 MHz and coupled into an optical fiber leading to the experiment. The remaining light is double passed through a second AOM to adjust its frequency by between $(220\,\text{MHz}+5\,\Gamma/(2\pi))$ and $(220\,\text{MHz}-14\,\Gamma/(2\pi))$ and then seeds the *slave* laser. Its light is split into a part for imaging and a second part for cooling. The imaging light is switched on and off with a dedicated AOM ($f = 86.5\,\text{MHz}$) and can be fed into two different fibers, for imaging along two different axes. The cooling light is switched on and off with another AOM ($f = 86.5\,\text{MHz}$), then split up and coupled into 4 different fibers for the horizontal and diagonal MOT beams.

A third laser is locked to the $F = 1 \leftrightarrow F' = 1, 2$ crossover line. It is split into two parts, which are both switched and frequency shifted ($f = 78.5\,\text{MHz}$) in opposite directions via separate AOMs. One part is the 'Pump 1-1' light, which is coupled into the same fiber as the 'Pump 2-2' light. The other is the repump light, which is fed into the two fibers carrying the diagonal MOT

beams.

An image of the glass cell with the surrounding laser outcouplers is shown in figure 3.8. We use a mirror MOT [110] which, in contrast to a regular MOT, requires only four laser beams by making use of light reflected from the chip surface. Because the gold mirror on the chip is corrugated by the underlying wire structure, the number of atoms which can be loaded by this mirror MOT is very sensitive to its position over the chip. When aligned correctly, the performance of the MOT is just slightly lower than that of mirror MOTs used in our group in previous experiments, where dielectric mirror coatings where employed. For magnetic trapping, the atoms are pumped by the two pump beams while a magnetic field in the x-direction is applied. We can image the atoms along two directions. For the squeezing experiments, we image along the y-direction, using a camera with high quantum efficiency and fast frame transfer, giving high spatial and atom number resolution. The camera in the x-direction has a much larger viewing angle and is used to image the first stages of the experiment. For more details on imaging, see section 3.7.

3.4 Current sources and magnetic shielding

The glass cell is enclosed in three pairs of Helmholtz coils which can create homogeneous magnetic offset fields in any direction (see figure 3.9). The coil wires are wound on a water cooled brass frame and generate fields of (6.6 G/A, 9.3 G/A, 1.3 G/A) in the (x, y, z) directions. For compensation of the earth's magnetic field we apply a small bias field with these coils.

For our experiments, we need to produce small BECs with high atom number stability. The stop frequency of the last radiofrequency evaporative cooling ramp defines the chemical potential and thus the atom number in the condensate. A fluctuating magnetic field results in a fluctuating Zeeman energy shift and thus in a fluctuation atom trap bottom, which in turn leads to an uncertainty in the effective trap depth defined by the rf stop frequency. As a result, the atom number in the trap fluctuates between experimental runs. For example, the chemical potential of a BEC with 1250 atoms in our condensation trap is $h \times 5.1\,\text{kHz}$ [85]. Correspondingly, a change in the magnetic field of only $5.1\,\text{kHz}/0.7\,\frac{\text{kHz}}{\text{mG}} = 7.3\,\text{mG}$ would lead to a loss of all atoms. Magnetic fields must therefore be much more stable than this.

We measure a fluctuation of the ambient magnetic field of up to 33 mG r. m. s. with a characteristic time scale of a few tens of seconds, which is mainly due to the subway line running close to our laboratory. We enclose the glass cell and the surrounding Helmholtz cage with a μ-metal shield which

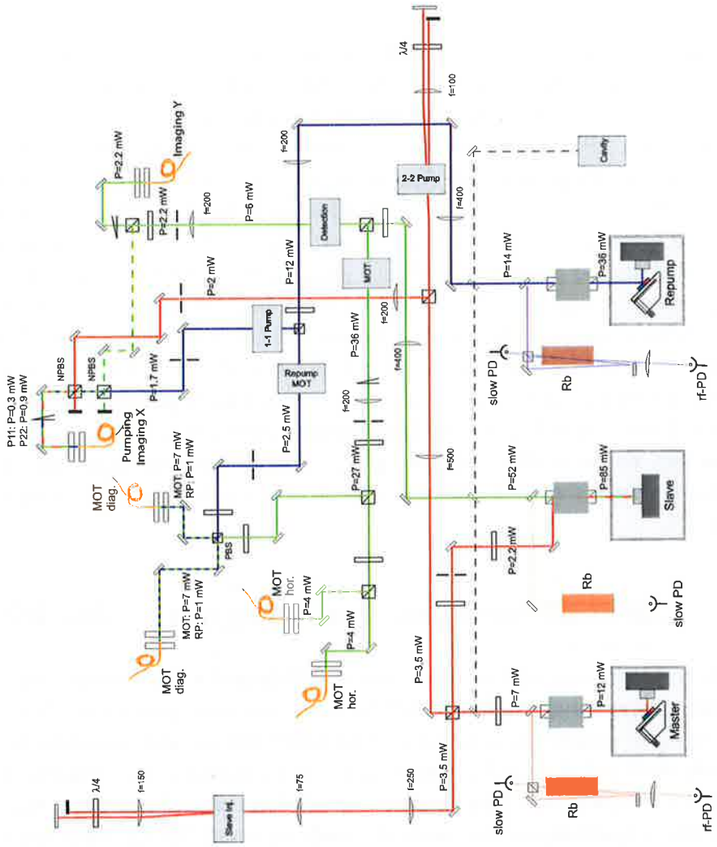

Figure 3.7: Beam paths in our laser system. The light originating from the master laser is drawn in red, from the slave laser in green and from the 'repump' laser in blue. White bars represent $\lambda/2$-plates, unless indicated otherwise, grey boxes represent AOMs, and the wedges represent mechanical beam shutters. The focal lengths of the lenses and the beam powers at various positions are indicated. The powers directly before the fiber couplers are measured in the corresponding phase of the experiment (for example P11 was measured during pumping) and are usually less than the maximally achievable powers.

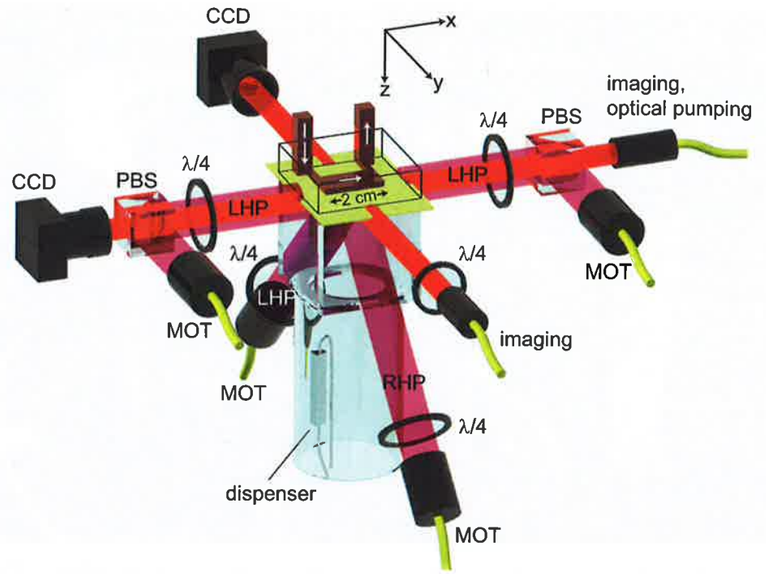

Figure 3.8: Glass cell with laser beams. Schematic drawing of the glass cell and the laser beams for MOT, molasses, optical pumping, and imaging in two directions. The polarizations of the MOT beams are indicated (LHP = left hand polarized, RHP = right hand polarized), polarizing beam splitters are marked with PBS. Figure adapted from [49].

reduces the fluctuations to about 220 μG r. m. s.

Furthermore, we use very stable current sources[4], both for the magnetic coils and for the chip wires, and disconnect all unused wires in the final stage of the experiment with mechanical or solid-state relays.

An exception is the current source used to produce the magnetic field in the y-direction[5]. It is needed to produce high magnetic fields for the first tight evaporation traps, but it shows a relatively strong residual modulation of 0.9 mA$\hat{=}$8 mG peak to peak at a total output of 590 mA$\hat{=}$5.2 G. To first order, the result of this is not a change of the magnetic field in the trap center, but a fluctuation of the magnetic trap position, which lead to phase noise in the squeezing experiments (see section 4.4.2). For the future, we plan to disconnect this source from the experiment after the second evaporation

[4] homebuilt bipolar current sources with a stability better than $\Delta I/I_{\max} < 10^{-5}$ and switching times of typically 15 μs (for more information see [107]) and *High Finesse* 20 mA/10 V bipolar current sources

[5] FUG NLN 350M-20

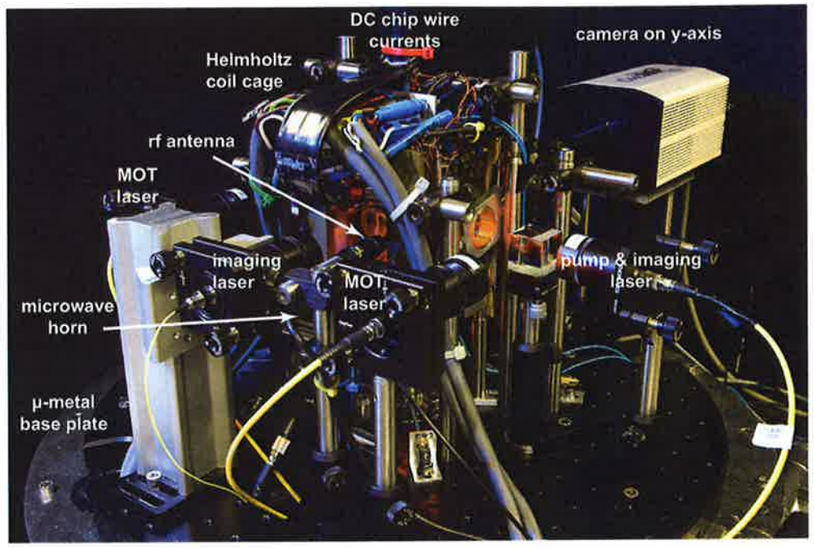

Figure 3.9: Experimental setup overview. The vacuum glass cell (not visible) is enclosed by three pairs of Helmholtz coils. The black ribbon cable carries all on-chip DC currents, and the other wires carry the magnetic coil currents. The complete setup (except the cameras) can be enclosed in a μ-metal shield, the base plate of which is visible in the photo.

ramp, using a solid state relay, and to replace it with a stable home built current source during the later stages.

3.5 High-frequency electronics

3.5.1 State preparation

The states $|0\rangle$ and $|1\rangle$ are coupled with a combined microwave and radiofrequency two-photon drive via an off-resonant intermediate state (see section 1.1.4). In our experiment, in order to achieve a homogeneous field over the entire atom cloud, both are applied through off-chip antennas.

The **radiofrequency** antenna is a wire loop, 2.5 cm in diameter and positioned approximately 2 cm from the glass cell. The polarization of the radiation is linear and perpendicular to the static magnetic field in the trap center, thus predominantly σ^- and σ^+ transitions are driven. The rf current

is produced by an Agilent 33250A function generator, fed through a separate switch, and amplified to 2 W over 50 Ω. The relative long-term stability of the rf amplitude in the $\frac{\pi}{2}$-pulses for state preparation is measured to be 1×10^{-3} r. m. s. The same hardware is also used for evaporative cooling.

The **microwave** source is a microwave horn, placed at a distance of about 7 cm from the glass cell. The microwave radiation is linearly polarized and perpendicular to the static magnetic field in the trap center. It thus drives predominantly σ^+ and σ^- transitions. The microwave radiation is provided by an Agilent E8257D generator which runs in continuous wave mode and is switched with an external switch before it is amplified to 4 W, which is radiated from the horn. We measure a relative pulse amplitude stability of 2×10^{-3} r. m. s.

All signal generators are phase locked to the oven controlled quartz oscillator of an Agilent E8257D microwave generator (equipped with the UNX ultra low phase noise option), or alternatively to an ultra stable reference quartz oscillator[6].

The Rabi frequency of the two-photon drive is $\Omega = 2\pi \times 2.1\,\mathrm{kHz}$ at an intermediate state detuning of $\Delta_{\mathrm{int}} = 2\pi \times 360\,\mathrm{kHz}$ – much faster than the motional dynamics in the trap. We find that the microwave radiation induces currents on the chip [64, 45] which lead to an inhomogeneous microwave intensity distribution over the trapped atoms. As a consequence, Rabi oscillations decay with a time constant of 15 ms. Nevertheless, we achieve an efficiency of a π-pulse of $(96 \pm 1)\,\%$, as shown in figure 3.10.

3.5.2 On-chip microwave

The microwave for the on-chip CPW is generated by an Agilent E8257D generator, whose output power is amplified and then stabilized with the help of an external detector and the generator's internal PI-controller. The AM input of the generator is used for amplitude control. We measure a relative long-term drift of the output power of $< 5 \times 10^{-4}$ peak-to-peak. No drifts of the CPW transmissivity were detected.

The amplitude stability of the on-chip microwave is of great importance: a fluctuating near-field potential leads to fluctuating level shifts of the clock states and thus to phase noise. Indeed, we suspect amplitude fluctuations of the near-field and position fluctuations of the atoms in this near-field to be the main source of phase noise in our experiment, leading to a reduced

[6] Oscilloquartz OCXO 8607-BM

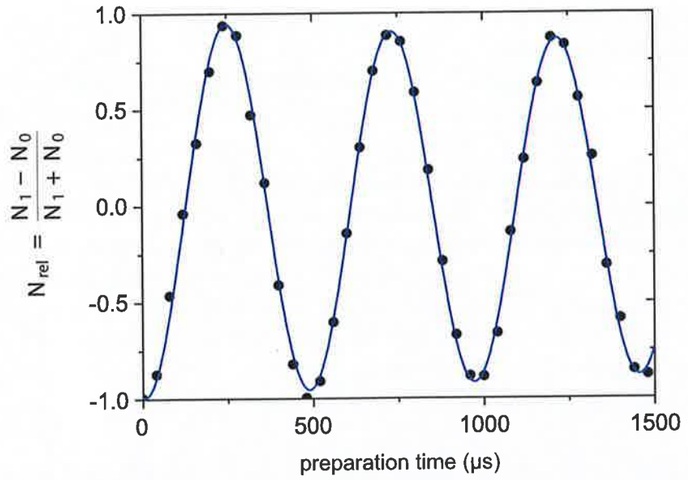

Figure 3.10: Rabi oscillations. Resonant Rabi oscillations of the relative atom number $N_{rel} = (N_1 - N_0)/(N_1 + N_0)$, recorded by varying the duration of the state preparation pulse. The fidelity of a π-pulse is $(96 \pm 1)\,\%$. The decay with a time constant of 15 ms is due to spatial gradients in Ω near the structured metallic chip surface which imposes boundary conditions on the electromagnetic field.

squeezing performance (see section 4.4). For future experiments, we will therefore employ an improved amplitude stabilization using an external PI-controller and variable attenuator.

3.6 Experiment control

The BEC production and subsequent experiments on spin squeezing are complicated sequences, involving many steps. Lasers have to be switched on and off as well as modulated in intensity and frequency, while currents and magnetic fields need to be adjusted, and radiofrequency and microwave generators programmed and triggered. About 35 analog and 25 digital control channels are needed to run the experiment in its present state. We control the experiment with a desktop computer which is equipped with National Instruments (NI) analog and digital output cards[7]. In total, 52 analog and 48 digital channels are available with a time resolution of $10\,\mu$s. For some

[7] 2×PCI-6733, 1×PCI-6723, 1×PCIe-6259

experimental parameters, nanosecond time resolution is achieved by using a digital delay generator[8], which is triggered by the experiment control. The sequence can be stopped and synchronized to the power line phase at any stage to minimize the effect of residual 50 Hz modulation on currents and magnetic fields. We use *Goodtime*, a program written by Jakob Reichel, to control the NI hardware and program external devices (e. g. frequency generators) via GPIB. It also communicates with a second computer which runs an application to control and read out the cameras. This software, called *Matcam*, is written in *Matlab* and was developed by Pascal Böhi [45].

3.7 Imaging

A crucial ingredient for our experiments on spin squeezing is an imaging system with high atom number resolution. The standard quantum limit for our typical BECs ($N = 1250$) is only $\Delta S_z^{SQL} = \sqrt{N}/2 = 17.7$, which means we need to detect the relative atom number $S_z = (N_1 - N_0)/2$ with a significantly better resolution to be able to detect spin squeezing. On the other hand, we prepare states with $0 \leq N_{0,1} \leq N$, i. e. we need to detect relatively large atom numbers, which requires a highly dynamical imaging method. Absorption imaging fulfills both requirements and allows large atom numbers to be detected with high resolution. It is fundamentally limited by the photon shot noise of the imaging laser. In the following, I describe the basic principles of absorption imaging, how to calculate atom numbers from the camera images, and derive the optimal parameters for low noise imaging. I then describe our hardware including calibration measurements and image analysis.

3.7.1 Absorption imaging

If an atomic cloud is illuminated by a laser beam of resonant light, it scatters some of it and thus casts a shadow in the beam which can be detected by a camera. Knowing the scattering cross sections of the atoms, the atom number in the cloud can be calculated from the amount of light absorbed from the beam.

According to the Beer-Lambert law [111], light traveling along the z-direction and passing through a thin sheet of atoms with thickness dz is absorbed, such that the light intensity is decreased by a small fraction

$$\frac{dI}{I} = -n(z)\sigma(I)dz, \tag{3.1}$$

[8] SRS DG535

where $n(z)$ is the number of atoms per unit volume with intensity dependent scattering cross section $\sigma(I)$. To determine the atom number per area of an atom cloud extended along the z-direction, we integrate equation (3.1) to get

$$\frac{dN}{dA} = \int n(z)dz = -\int_{I_0}^{I_1} \frac{1}{I\sigma(I)} dI, \tag{3.2}$$

where I_0 (I_1) is the intensity of the light before (after) passing through the atoms. We apply a magnetic quantization field B_{img} and image the atoms on the $|F = 2, m_F = -2\rangle \leftrightarrow |F' = 3, m'_F = -3\rangle$ cycling transition (the frequency of the imaging light is adjusted, such that it drives the transition resonantly at B_{img}). We can thus model the absorption as for a two-level atom with the cross section

$$\sigma(I) = \frac{\sigma_0}{1 + I/I_{\text{sat}}}. \tag{3.3}$$

Here, $\sigma_0 = \frac{3\lambda^2}{2\pi} = 2.9 \times 10^{-13}\,\text{m}^2$ is the resonant cross section and $I_{\text{sat}} = \frac{\hbar\omega\Gamma}{2\sigma_0} = 1.67\,\text{mW/cm}^2$ the saturation intensity for the cycling transition [50]. We thus get

$$\frac{dN}{dA} = -\int_{I_0}^{I_1} \frac{1 + I/I_{\text{sat}}}{\sigma_0 I} dI = \frac{1}{\sigma_0} \ln\left(\frac{I_0}{I_1}\right) + \frac{1}{\sigma_0 I_{\text{sat}}}(I_0 - I_1). \tag{3.4}$$

Figure 3.11 shows the dependence of the two terms in equation (3.4) on the imaging intensity I_0. For small intensities $I_0 \ll I_{\text{sat}}$ saturation effects can be neglected and the first term dominates the sum. For large intensities $I_0 \gg I_{\text{sat}}$ the atoms are completely saturated and each atom scatters the same amount of light. The atom number is then simply proportional to the total scattered light. For $I_0 = I_{\text{sat}}$ both terms contribute equally.

In the experiment, the atoms are in the $F = 2$ manifold, but not necessarily in the $m_F = -2$ sublevel before detection. They thus need to be pumped to the cycling transition with the first few photons of the imaging beam. A Monte-Carlo simulation, assuming perfect σ^- polarization of the imaging beam, shows that for $B_{\text{img}} = 2\,\text{G}$, an atom in state $|F = 2, m_F = 1\rangle$ scatters an average of 5.3 photons and needs $1.6\,\mu s$ (for $I = I_{\text{sat}}$) until it reaches the cycling transition. An atom in state $|F = 2, m_F = 0\rangle$ needs $1.0\,\mu s$ and in state $|F = 2, m_F = -1\rangle$ only $0.5\,\mu s$. The main reason for this difference lies in the different matrix elements of the transitions and not in the different detunings due to the magnetic Zeeman shift, as one might expect at first.

We take this effect and the possibility of an imperfectly polarized imaging beam, as well as the Doppler shift due to photon recoil (see below) into account by replacing σ_0 and I_{sat} with effective values $\sigma_{\text{eff}} < \sigma_0$ and $I_{\text{eff}} > I_{\text{sat}}$

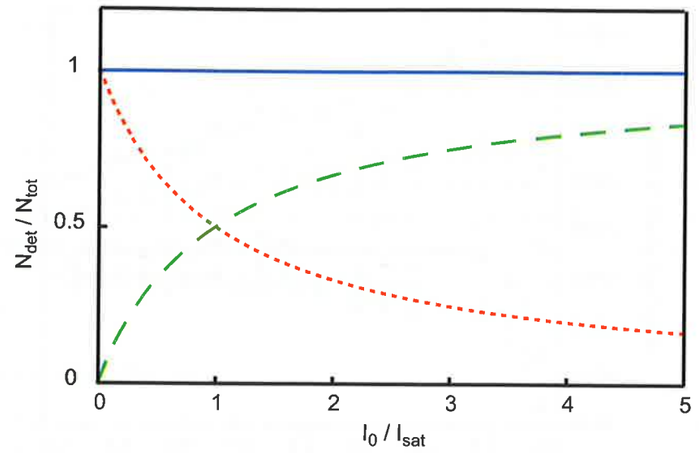

Figure 3.11: Detected atom number as function of imaging intensity I_0. The three curves correspond to the fraction of detected atoms as a function of imaging intensity if the atom number is calculated using the complete formula (3.4) (solid blue), only the first term (dotted red) or only the second term (dashed green).

[112]. The second term in (3.4) is not affected by this change since $\sigma_{\text{eff}} I_{\text{eff}} = \sigma_0 I_{\text{sat}} = \hbar\omega\Gamma/2 = const$, where ω is the frequency of the imaging light and Γ the natural line width of the D_2 line. To determine σ_{eff}, we thus repeatedly prepare atom clouds with the same atom number, measure N for different imaging intensities, and adjust σ_{eff} such that the atom number is independent of the imaging intensity. For example, if we measure smaller atom numbers for low imaging intensities than for high intensities, we know that the first term in (3.4) is too small and therefore σ_{eff} is too large.

Figure 3.12 shows measurements of an optically thin thermal cloud for imaging intensities between $I = 0.2\,I_{\text{sat}}$ and $4\,I_{\text{sat}}$, analyzed with different values for σ_{eff}. In our experiments we typically measure $\sigma_{\text{eff}} = 0.9\,\sigma_0$. As can be seen from figure 3.12, this method gives good results, but should only be trusted to determine the atom number with an accuracy of about $\sim 10\,\%$. A more accurate method to calibrate the actual atom number is using the quantum projection noise, as will be described in section 3.7.5.

Optimal imaging parameters

The only parameters entering equation (3.4) afflicted by noise are the imaging intensities before (I_0) and after the atom cloud (I_1). In practice, we take

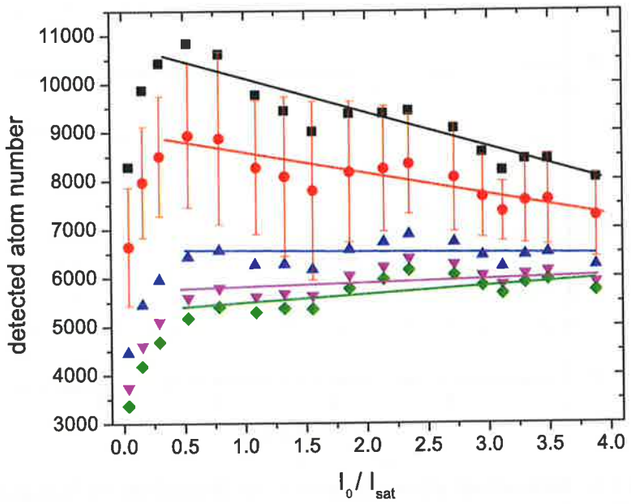

Figure 3.12: Detected atom number as a function of imaging intensity for different effective scattering lengths. The same images of an optically thin thermal cloud are analyzed with different values for σ_{eff}. $\frac{\sigma_{\text{eff}}}{\sigma_0} = 1$ (green), 0.9 (violet), 0.75 (blue), 0.5 (red), and 0.4 (black). Each data point is an average over 9 experimental runs. The error bars on all but the red data are omitted for clarity but they are of comparable size. The large error is due to fluctuations in the atom number preparation which were exceptionally high at the day of this measurement because of high frequency noise on the main power line. The solid lines are guides to the eye. For imaging intensities $I < 0.5\, I_{\text{sat}}$ the number of detected photons and thus the image quality becomes poor for our imaging pulse duration of $\tau = 40\,\mu$s and the high magnification $M \approx 10$. The steep drop in detected atom number might partly be due to pumping effects, although it cannot be quantitatively explained by them.

two images, one with atoms present to determine I_1, and a second when the atoms have fallen out of the field of view to determine I_0. The two intensities fluctuate due to photon shot noise with $\Delta I^2 \propto I$. Thus, the variance of the atom number is

$$\Delta\left(\frac{dN}{dA}\right)^2 \propto \frac{1}{I_0} + \frac{1}{I_1} + \frac{4}{I_{\text{eff}}} + \frac{I_0 + I_1}{I_{\text{eff}}^2}, \tag{3.5}$$

where I_0 and I_1 correspond to the mean values. This variance is minimized for $I_0 \cdot I_1 = I_{\text{eff}}^2$. Calling $t = I_1/I_0$ the average transmittance this indicates an

optimal imaging intensity of $I_0^{\text{opt}} = I_{\text{eff}}/\sqrt{t}$. For optically thin atom clouds ($f \approx 1$) the optimal intensity is I_{eff}; the thicker the cloud, the higher the optimal intensity. In our experiments with small condensates $t \approx 0.6$ and we typically use $I_0 = I_{\text{eff}} = 1.1\, I_{\text{sat}}$.

For this analysis we have assumed that σ_{eff} and the cloud's size are constant during the imaging pulse and independent of the imaging intensity. This is not strictly true, since the scattering of photons leads to a Doppler shift and an atom diffusion which increases the cloud size. However, I will show in the next section that these effects are negligible for our imaging parameters.

Photon recoil effects

During the imaging pulse the atoms scatter many photons. This leads to an acceleration

$$a(t) = \dot{v}(t) = v_{\text{rec}} R_{\text{sc}}(t) \tag{3.6}$$

of the atoms toward the camera, with the recoil velocity $v_{\text{rec}} = h/(m\lambda) = 5.9\,\text{mm/s}$ and the photon scattering rate

$$R_{\text{sc}}(t) = \frac{\Gamma}{2} \frac{I_0/I_{\text{eff}}}{1 + (I_0/I_{\text{eff}}) + 4(\delta(t)/\Gamma)^2}. \tag{3.7}$$

Here, $\delta(t)$ is the detuning of the imaging light, which again depends on the velocity as $\delta(t) = \delta_0 - v(t)/\lambda$ because of the Doppler shift experienced by the accelerated atoms. δ_0 is the detuning for atoms at rest and should be chosen slightly positive (blue-detuned) to compensate the Doppler effect. Solving the differential equation (3.6), one finds that, during our imaging pulse duration $\tau = 40\,\mu$s and for all imaging intensities I_0, the acceleration is well approximated as constant. For $I_0 = 1.1\, I_{\text{sat}}$ and $\delta_0 = 2\pi \times 1.5\,\text{MHz}$, the atoms scatter 385 photons and are pushed 45 μm toward the camera. At the end of the imaging pulse, the absorption line is Doppler shifted by $v(\tau)/\lambda = 2.9\,\text{MHz}$.

The effective scattering cross section

$$\sigma_{\text{eff}}(t) = \sigma_{\text{eff},0} \frac{1 + (I_0/I_{\text{sat}})}{1 + (I_0/I_{\text{eff}}) + 4(\delta(t)/\Gamma)^2} \tag{3.8}$$

changes during the imaging pulse, as $\delta(t)$ changes. $\sigma_{\text{eff},0}$ corresponds to the effective scattering cross section at $\delta = 0$, smaller than σ_0 due to pumping effects and imperfect imaging beam polarization (see above). Using higher imaging intensities, the atoms scatter more light, are accelerated stronger, and gather a higher velocity during the imaging pulse, which leads to a

stronger Doppler shift. One would therefore at first expect that $\bar{\sigma}_{\text{eff}}$, averaged over the time of the imaging pulse, decreases with increasing imaging intensity. However, it turns out that the intensity broadening of the absorption line compensates this effect almost completely. For $\delta_0 = 2\pi \times 1.5\,\text{MHz}$, one achieves $0.9\,\sigma_{\text{eff},0} < \bar{\sigma}_{\text{eff}} < \sigma_{\text{eff},0}$ for all imaging intensities.

Besides pushing the atoms toward the camera, the photon scattering leads also to a random walk of each atom due to the random momentum kicks. An atom is thus displaced on average by $\Delta r_{\text{rms}} = \frac{v_{\text{rec}}}{3}\sqrt{\frac{\Gamma\tau^3}{2}}$ [113], which leads to a blurring of the image. For our experimental parameters, $\Delta r_{\text{rms}} = 2.2\,\mu\text{m}$. The image blurring as well as the translation of the atoms in the line of sight are tolerable since the camera's optical resolution is $4.4\,\mu\text{m}$ and the Rayleigh range $z_R \approx 80\,\mu\text{m}$ (see section 3.7.3).

3.7.2 State-selective imaging

As previously described, we use the $F = 2 \leftrightarrow F' = 3$ transition to image the atoms. If we only shine in light of the corresponding frequency, we image only atoms in $F = 2$, in particular in state $|1\rangle$. If we shine in repumping light on the $F = 1 \leftrightarrow F' = 2$ transition shortly before or during the imaging light, we can also detect atoms in the $F = 1$ manifold, i. e. we detect atoms in both $|0\rangle$ and $|1\rangle$.

To state-selectively image atoms in either state [114] we use three images: we take the first image with solely the $F = 2 \leftrightarrow F' = 3$ light, such that only atoms in state $|1\rangle$ are detected. We then wait for 1.7 ms, during which the previously imaged atoms drift out of the focus of the camera by approximately 4 mm due to their recoil acquired during imaging. Because the depth of field of the camera is only a few tens of micrometers ($z_R \approx 80\,\mu\text{m}$) they are invisible on subsequent images. The second image is taken after an additional repumping light pulse of duration $20\,\mu\text{s}$ has transfered all remaining atoms in $F = 2$. The atoms in state $|1\rangle$ have been 'blown away' by the first imaging pulse and we detect only atoms in state $|0\rangle$. Finally, after waiting another 1.7 ms during which all atoms fall out of the field of view, we take a third image which serves as a reference for both previous images to determine I_0 for each pixel. Figure 3.13 shows the resulting state-selective images of a BEC in a superposition of states $|0\rangle$ and $|1\rangle$.

By recording Rabi or Ramsey oscillations (see figure 3.14), we find that the detection efficiency for state $|1\rangle$ is typically a factor $p_d = 0.9$ lower than for state $|0\rangle$. A possible explanation is that atoms in state $|1\rangle$ need to be pumped further to the cycling transition at the beginning of the imaging pulse than atoms in state $|0\rangle$. We determine the detection efficiency once

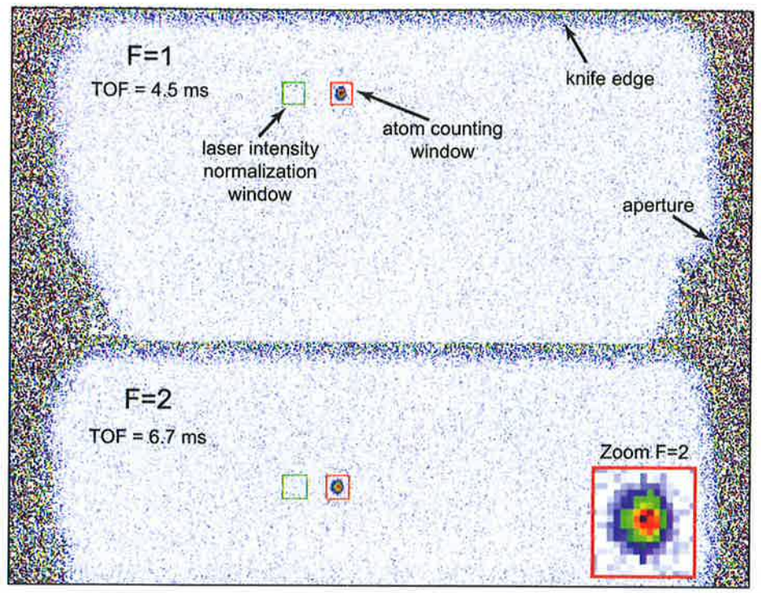

Figure 3.13: State-selective imaging. State-selective false-color images of a BEC in a superposition of states $|0\rangle$ and $|1\rangle$. The images are taken with a delay of 1.7 ms, the reference image is taken another 1.7 ms after the second. The imaging region is bounded by the aperture on the sides and the knife edge at the top. The FWHM diameters of the imaged atom clouds are 15 μm in the vertical and 10 μm in the horizontal direction, both larger than the optical resolution of our imaging system of 4 μm. The maximum optical densities in the cloud centers for 600 atoms in each state is $\text{OD} = -\ln(t) \approx 0.5$. The red boxes show typical integration windows for determining N_0 and N_1. The green boxes are used to correct for fluctuating laser intensity between the three images.

every day and multiply N_1 by $1/p_d$ before continuing with the analysis.

3.7.3 Imaging hardware

A schematic of our imaging hardware is shown in figure 3.15. The imaging light is brought from the optical table to the glass cell via an optical fiber. An aperture is used to extract the central part of the Gaussian beam profile. The aperture is then imaged without magnification onto the plane of the atoms. This guarantees an even illumination of the atoms and prevents unwanted

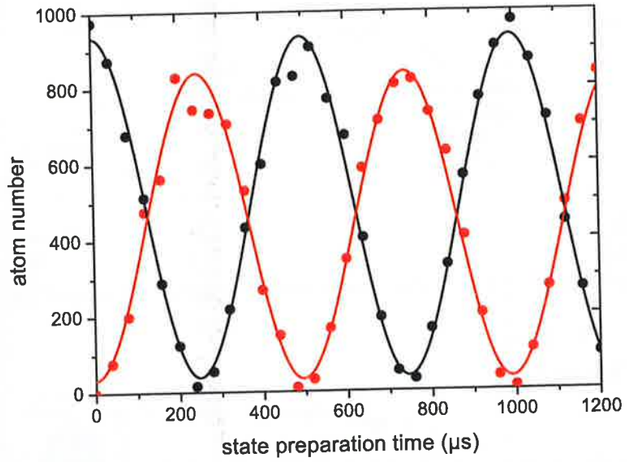

Figure 3.14: Determining the detectivity of the atomic states. Rabi oscillation between the two clock states. Shown is the detected atom number in state $|0\rangle$ (black) and $|1\rangle$ (red) as a function of preparation pulse length. From the fits we determine that for this measurement the detection efficiency of state $|1\rangle$ was a factor $p_d = 0.9$ lower than that of state $|0\rangle$.

reflections in the tube of the camera objective, as well as diffraction on the chip surface. Omitting the lens would cause strong concentric modulation of the imaging light intensity due to diffraction on the aperture. The originally linearly polarized light coming out of the fiber is left hand polarized by a quarter wave plate in order to drive the σ^- imaging transition. However, since the light from the fiber is not perfectly linearly polarized, some imaging light can also drive the π or σ^+ transitions, which is the reason why $\sigma_{\text{eff}} < \sigma_0$. In future setups, a polarizer before the quarter wave plate will guaranty a purer polarization and thus a larger σ_{eff}.

The camera objective consists of two lenses, placed at a distance of their focal length from the atoms and the CCD chip, respectively. The front lens is a diffraction limited Melles Griot laser doublet[9] with a focal length of 40 mm and a numerical aperture of NA= 0.32. The second lens is an achromat[10] with a focal length of 400 mm. The theoretical magnification M is thus

[9]Melles Griot 06 LAI 005/076 Laser Doublet
[10]Thorlabs AC254-400-B Near Infrared Achromatic Doublet

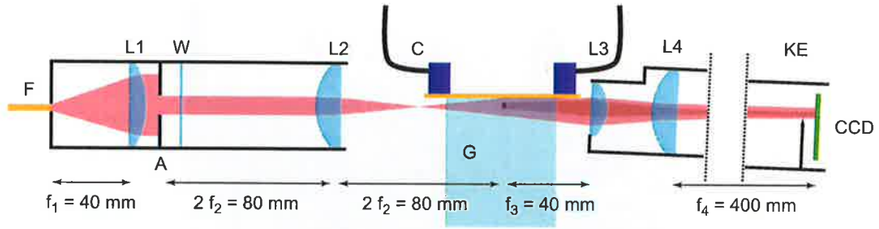

Figure 3.15: Schematic drawing of our imaging setup. The linearly polarized laser light is brought to the experiment through an optical fiber F, collimated with a lens $L1$, cut with an aperture A and circularly polarized with a $\lambda/4$-wave plate W. The aperture is imaged with lens $L2$ onto the plane of the atoms in the glass cell G to reduce fringes due to diffraction. The atoms are imaged with an objective consisting of the lenses $L3$ and $L4$. The objective is tilted very slightly upward (exaggerated in the schematic) so that the part of the CCD not covered by the knife edge KE is exposed.

10. With the help of an 1951 USAF optical calibration target we measure $M = 10.17$. Because of this high magnification, the optical properties of the first lens are much more critical for good optical resolution than those of the second. According to the Rayleigh criterion [111], the objective would in theory allow a resolution of 1.5 μm, but in practice the atom chip surface, which clips the imaging beam, limits the numerical aperture and the glass wall of the vacuum chamber causes aberrations. We measure a resolution better than 228 lp/mm, or 4.4 μm (see figure 3.16).

If parts of the imaging system vibrate, the two images taken to determine the atom number will not be perfectly aligned on the camera CCD chip. Although we try to illuminate the atoms as evenly as possible, residual modulation of the imaging intensity over the image cannot be avoided. These modulations then cause artificial modulations in space in the atom number. It is therefore crucial for a good imaging quality to mount the camera as rigidly as possible and minimize the time between the two images. It also turned out to be indispensable to secure the objective close to its front lens by clamping it to a sturdy post.

Our camera is an Andor Ikon-M back illuminated deep depletion CCD with a quantum efficiency of $q = 0.9$ at 780 nm. We use it in a fast frame transfer (FFT) mode, where only the top third of the pixels is illuminated and repeatedly shifted down for storing the first two images. To make sure that the 'storage area' of the CCD is not exposed, we cover it with a knife edge, placed as close as possible to the chip, which in turn is covered with a

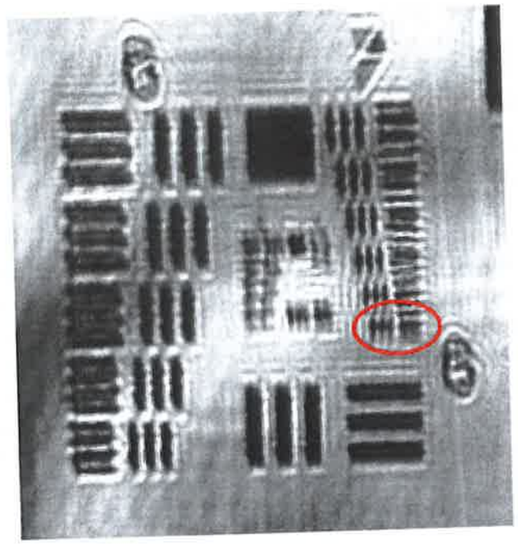

Figure 3.16: Imaging resolution, measured with an 1951 USAF optical calibration target. The group indicated by the red circle consists of three lines, each 2.2 μm wide and spaced by 2.2 μm (228 lp/mm) and can still be resolved by the objective. Reflections of the laser light used to image the target on the glass substrate result in double images (especially pronounced at the number 7 in the top right corner). The circular intensity modulation of the imaging light (centered around the lower right corner) is due to diffraction of the laser light on the aperture, since this image was taken before we introduced the lens L2 (see figure 3.15).

sheet of black cardboard to reduce reflections from it. The reason for using the FFT mode is that shifting a region of the CCD can be done with a high speed of 6 μs/line whereas the readout of the whole image (1024×1024 pixels) takes about a second due to the slow A/D conversion. The FFT mode enables us to image both atomic states plus a reference image within one single experimental cycle and thus determine the total and relative atom number for each shot. This allows us to take out the fluctuations of N in determining S_z.

3.7.4 Image analysis

So far, I have derived all expressions with the physical meaningful imaging light intensity I. The camera measures counts per pixel k, which can be

translated into intensity as

$$I = \frac{\hbar\omega k}{qgA_{\mathrm{px}}\tau}, \tag{3.9}$$

where $q = 0.9$ is the quantum efficiency of the camera, $g = 1.1$ the gain of the camera amplifier, and $A_{\mathrm{px}} = (1.28\,\mu\mathrm{m})^2$ is the area of a camera pixel in the plane of the atoms (including magnification). Thus, I_{sat} corresponds to 4300 counts. Even if no imaging light is falling onto the CCD, the camera has a dark count rate due to ambient stray light and the camera electronics. We minimize the stray light by closing all holes in the μ-metal shield with black tape and switching off the pressure gauge. The camera chip is cooled to -80°C and the remaining dark count rate is very constant over time (shot to shot fluctuation ≈ 9 counts r. m. s. on 4350 dark-counts, dominated by an electronic offset). It is therefore sufficient to take a *dark image* once every day, for which we run a usual experimental sequence but omit the imaging pulses.

The number of atoms per pixel can then be calculated as

$$\frac{N}{A_{px}} = \frac{1}{\sigma_{\mathrm{eff}}}\ln\left(\frac{k_0 - k_d}{k_1 - k_d}\right) + \frac{2}{qgA_{px}\Gamma\tau}(k_0 - k_1), \tag{3.10}$$

where k_0, k_1, and k_d are the counts per pixel for the reference image, the image with atoms, and the dark image, respectively.

To calculate the total number of atoms in an atomic cloud, we define a rectangular area, called the *image area*, in which the atoms per pixel are summed up. Since the variance of the imaging noise due to photon shot noise is proportional to this area, it should be chosen as small as possible while covering the entire region where atoms are present. We usually use an image area of 30 μm $\times$ 30 μm for our small condensates (see figure 3.13). To take a possible fluctuation of the imaging laser intensity from the image with atoms to the reference image into account, we define a second area which contains no atoms and use it to normalize the counts (see figure 3.13). To measure the noise in the image area, we place a third area of same size close to the atoms, or use the image area itself while blocking one of the MOT beams and thus not trapping any atoms. We typically measure a noise of $\Delta N_{j,\mathrm{im}} \approx 10$ atoms r. m. s. between different experimental cycles. Calculating the expected shot noise from the observed imaging light intensity gives similar results.

Detecting both states within one shot allows us to eliminate fluctuations in the atom number preparation from our analysis. We first discard shots where the total atom number differs by more than 150 atoms from the mean atom number. We then define for each shot corrected atom numbers as

$$N_{j,\mathrm{corr}} = \frac{N_j}{N_0 + N_1}\left(\overline{N}_0 + \overline{N}_1\right) = \frac{N_j}{N_0 + N_1}\overline{N}, \tag{3.11}$$

where the mean is taken over all shots (which were not discarded) in an experimental run. The corrected z-component of the collective spin is then

$$S_{z,\mathrm{corr}} = \frac{N_{1,\mathrm{corr}} - N_{0,\mathrm{corr}}}{2} = \frac{N_1 - N_0}{N_0 + N_1}\frac{\overline{N}}{2}. \tag{3.12}$$

The imaging noise contribution on the two atom numbers is independent whereas the projection noise is correlated. We can calculate the additional noise in S_z due to imaging noise as

$$\Delta S^2_{z,\mathrm{im}} = \frac{1}{\overline{N}^2}\left(\overline{N}_0^2 \Delta N^2_{1,\mathrm{im}} + \overline{N}_1^2 \Delta N^2_{0,\mathrm{im}}\right). \tag{3.13}$$

In the case of equal atom numbers $\overline{N}_0 = \overline{N}_1 = \overline{N}/2$, $\Delta S_{z,\mathrm{im}}$ is thus a factor of $\sqrt{2}$ smaller, compared to the imaging noise in the individual atom numbers $\Delta N_{j,\mathrm{im}}$. From now on, the experimentally measured noise in S_z is defined as

$$\Delta S_z^2 \equiv \Delta S^2_{z,\mathrm{corr}} - \Delta S^2_{z,\mathrm{im}}, \tag{3.14}$$

i. e. corrected for atom number fluctuations and imaging noise. This value can be compared directly with the theoretical prediction. For a summary of the processing applied to the raw atom numbers, see appendix C.

3.7.5 Atom number calibration using projection noise

For our experiments, it is crucial to know the total atom number $N = N_0 + N_1$ accurately. Introducing an effective scattering cross section σ_{eff}, as described in section 3.7.1, provides a first calibration of our imaging system, but it can suffer from systematics, e. g. due to a dependence of the pumping efficiency on the imaging intensity.

An independent test of the atom number calibration can be obtained by observing the scaling of projection noise with the total atom number for a coherent spin state. As shown in section 2.2.2, the variance in the z-component of the collective spin $S_z = (N_1 - N_0)/2$ scales linearly with N for such a state, $\Delta S_z^2 = N/4$. Figure 3.17 shows ΔS_z^2, measured directly after a $\frac{\pi}{2}$-pulse as a function of N. The constant offset due to imaging noise is subtracted as described in the previous section. The error bars are calculated as $\Delta(\Delta S_\theta^2) = \sqrt{2/M}\Delta S_\theta^2$, where M is the number of measurements for each total atom number N [115]. The observed linear behavior confirms that projection noise $\Delta S_z^2 \propto N$ dominates over technical noise which generally scales as $\Delta S_z^2 \propto N^2$. A linear fit to the data in Fig. 3.17 yields a slope of 0.22 ± 0.01. This agrees with the theoretically expected slope of 1/4 to better than 15 %. The difference lies within the error of our atom number

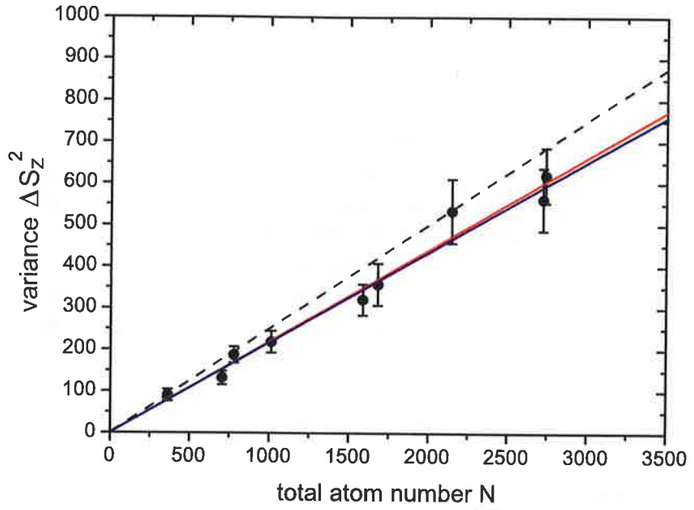

Figure 3.17: Projection noise as a function of atom number. A measurement of the variance ΔS_z^2 directly after a $\frac{\pi}{2}$-pulse is shown as a function of total atom number N, where N is independently calibrated using σ_{eff}. The dashed line shows the expected linear scaling with a slope of 1/4, the blue line is a linear fit to the data which yields a slope of 0.22 ± 0.01. The red line is a quadratic fit with $\Delta S_z^2 = aN + bN^2$. It yields $a = 0.22 \pm 0.02$ and $b = (0.06 \pm 1) \times 10^{-5}$, confirming the linear scaling expected for projection noise.

calibration using σ_{eff}. As the dependence of ΔS_z^2 on N can be very accurately determined from Fig. 3.17, we use it to calibrate the total atom number by rescaling N so that the slope of the linear fit is 1/4.

3.8 Experimental sequence

An experimental cycle consists of several MOT phases, where atoms are loaded from the background gas and pre-cooled, a molasses phase for sub-Doppler cooling the atoms, an optical pumping phase to bring the atoms into state $|0\rangle$, several magnetic traps in which the atoms are evaporatively cooled and condensed, and finally the experiment trap. A cycle takes about 12 seconds. Most of this time is used for the BEC preparation and the actual experiment lasts only the last few tens of milliseconds.

MOT phase

We load ^{87}Rb atoms from the background gas with a MOT utilizing the copper U-wire in the water cooled copper block behind the chip ($I = 48\,\mathrm{A}$) and a magnetic field in the y-direction ($B_y = 7.7\,G$). Fields in the x and z direction are used to position the MOT where the corrugation of the gold mirror is least perturbing. The magnetic quadrupole minimum is about 3 mm from the chip surface. The cooling lasers are red-detuned by $2\,\Gamma$ and we typically load $6 - 8 \times 10^6$ atoms within 7 s.

We briefly turn off the lasers while switching from the copper wire to a U-wire on the base chip ($I = 9.2\,\mathrm{A}$) and then reduce this current within 15 ms to 2.8 A to bring the atoms closer to the chip surface. During this ramp, we also increase the detuning to $14\,\Gamma$ and decrease B_y to 3.3 G. The atoms are now 400 μm from the chip surface.

Molasses phase

We then switch off all currents and magnetic fields, keep the laser detuning at $14\,\Gamma$, and reduce the laser powers to about half of their maximum. For an efficient sub-Doppler cooling, it is crucial that the laser beam power is balanced between the counter propagating beams and that all magnetic fields at the position of the atoms are compensated to zero. We achieve the latter by performing a Hanle type spectroscopy, where we use the $F = 2 \leftrightarrow F' = 2$ transition for imaging [116]. After typically 3 ms, the atoms reach a temperature below 10 μK.

Optical pumping

After the molasses, the atoms are distributed in the $F = 2$ manifold and we optically pump them into the magnetically trappable state $|0\rangle$. For this, we first switch off all lasers and switch on a quantization field of $B_x = 2\,\mathrm{G}$. We then switch on the two pump lasers for typically 500 μs. Both lasers are σ^- polarized and reduce the m_F quantum number of the atoms. The 2-2 pumper transfers the atoms to the $F = 1$ manifold while the 1-1 pumper brings them into the correct Zeeman sublevel $|1, -1\rangle$. During this process, the temperature of the atoms is increased by $2 - 3\,\mu$K.

Magnetic Ioffe traps

We now turn off all lasers and capture the atoms in a Ioffe-Pritchard trap, using the Z-shaped wire indicated in figure 3.2 ($I_z = 2.65\,\mathrm{A}$) and a field in the y-direction ($B_y = 12\,\mathrm{G}$). A good test for the overlap of this trap with

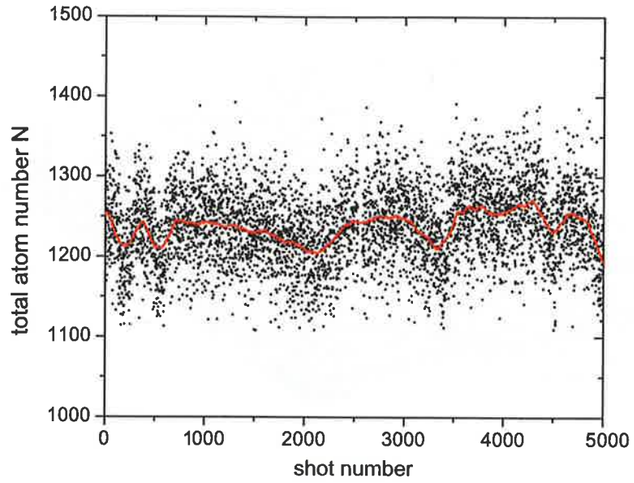

Figure 3.18: Total atom number N for 5000 subsequent measurements. A slow drift over time is observed, possibly due to drifting chip currents or magnetic fields. The red line is an adjacent average over 200 measurements to guide the eye. The mean atom number in this series of measurements is $N = 1243 \pm 47$.

the Molasses position and a successful laser cooling is provided by holding the atoms in this trap for half a second and waiting until the residual motion has damped out. We are typically left with 3.5×10^6 atoms. In the normal sequence this trap is used for only 2 ms.

We then compress the trap within 200 ms by ramping up B_y to 55 G while slightly decreasing I_z. The new trap has a distance of 76 μm from the chip surface and has a radial trapping frequency of 3.8 kHz. This tight trap enables fast thermalization rates for the first radiofrequency evaporative ramp (duration 500 ms, rf frequency ramped from 50 to 20 MHz). After this ramp, 1×10^6 atoms remain.

We decrease I_z and B_y again to relax the trap and bring it even closer to the chip surface ($d = 47\,\mu$m). Then, we ramp down the current in the Z-wire and at the same time increase the current in the so called *long Ioffe wire*. We turn on the dimple wire to 'dig' a dimple into this elongated trap. The dimple trap has again high trapping frequencies, and we carry out a second rf evaporation ramp from 19 to 1.8 MHz. All remaining atoms ($N \approx 3 \times 10^4$) have thermalized into the dimple trap and their temperature is close to, but still above, the condensation temperature T_c.

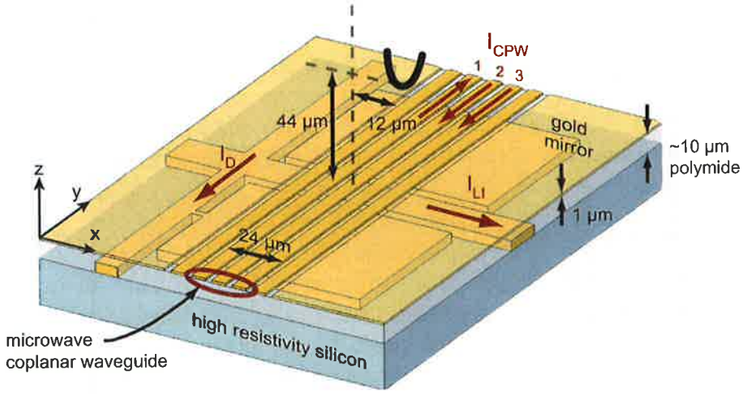

Figure 3.19: Schematic close-up of the experiment region. Static currents on the microwave CPW and on the wires on the lower science-chip layer are labeled; the arrows indicate the directions of the currents. The experimental trap has a distance of $d = 44\,\mu$m from the chip surface and is displaced in the x-direction by $12\,\mu$m with respect to the middle of the CPW.

In the next step, we smoothly replace the dimple wire current by the three CPW wire currents of 15 mA each (one current is reversed with respect to the others). The result is a slightly more relaxed trap in which we do the final evaporative ramp (rf frequency from 2 MHz to ~ 1.4 MHz) to Bose-condense the atoms. We cut into the condensate to define the atom number and end up with a small, pure BEC with typically $N = 1250 \pm 45$. Figure 3.18 shows the total atom number for 5000 subsequent measurements.

Finally, we adiabatically modify the currents in the CPW and the Long-Ioffe wire as well as the magnetic fields within 150 ms and end up with our experimental trap.

Experimental trap. This trap has trap frequencies of $(\omega_x, \omega_y, \omega_z) = 2\pi \times (109, 500, 500)$ Hz and a magnetic field in the trap center of $B_0 = 3.36$ G, close to the 'magic field' at which the magnetic moments of $|0\rangle$ and $|1\rangle$ are equal. It is located at a distance of $44\,\mu$m from the chip surface and is displaced by $12\,\mu$m in the x-direction with respect to the middle of the CPW (see figure 3.19).

For detection, after the experiment has been performed, we ramp the atoms within 30 ms into a relaxed trap, $200\,\mu$m from the chip surface. From

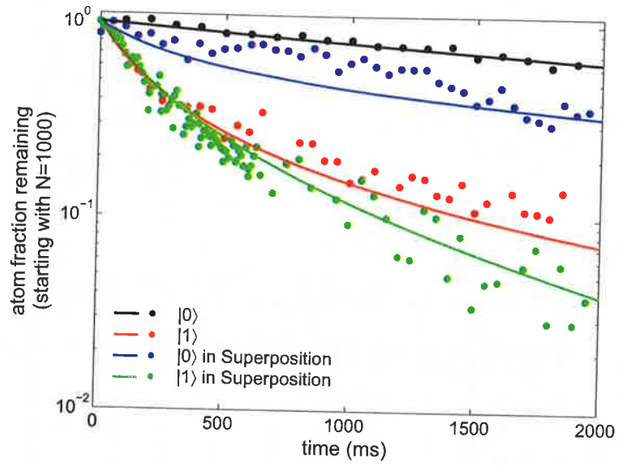

Figure 3.20: Lifetime of a BEC in our experimental trap. Experimental data (filled circles) and results from a Monte-Carlo simulation (solid lines) for a BEC initially in either state $|0\rangle$ or $|1\rangle$, or in an equal superposition of the type $\frac{1}{\sqrt{2}}(|0\rangle + |1\rangle)$.

there, the atoms fall and freely expand for 4.5 ms before we take the first image to detect state $|1\rangle$.
Table 3.1 gives an overview over all stages of the magnetic trapping sequence.

3.9 Trap lifetimes

Figure 3.20 shows a measurement of the lifetime of a BEC in the experimental trap. The losses in state $|0\rangle$ are dominated by background gas collisions whereas the losses in state $|1\rangle$ are much stronger due to two-body losses (see section 1.4.3). In a superposition, two-body inter-state collisions open an additional loss channel. We adjust the loss rates in a Monte-Carlo simulation to fit the measured data: $\gamma_{bg} = 0.2\,\mathrm{s}^{-1}$, $K_1 = 0.70 \times 10^{-13}\,\mathrm{cm}^3\mathrm{s}^{-1}$, $K_{01} = 0.50 \times 10^{-13}\,\mathrm{cm}^3\mathrm{s}^{-1}$, and $L_0 = 6 \times 10^{-30}\,\mathrm{cm}^6\mathrm{s}^{-1}$. These rates are slightly different from the literature values, possibly because we calculate them using the wrong atom density, which we calculate for our trapping parameters but do not measure independently. We use the measured rates to model losses in our spin squeezing analysis.

Step	Δt [ms]	I_Z	I_{LI} [A]	I_D	$I_{\mathrm{CPW},1}$	$I_{\mathrm{CPW},2}$ [mA]	$I_{\mathrm{CPW},3}$	B_x	B_y [G]	z_0 [μm]	f_1	f_2 [Hz]	f_3	B_0 [G]	ν_{RF} [MHz]
Z-Ioffe1	2	2.65	0	0	0	0	0	0	12	400	24	180	220	1.9	
ramp	200	↓	0	0	0	0	0	↓	↓						
Z-Ioffe2	500	2.5	0	0	0	0	0	1.4	55	76	16	3820	3870	1.9	50→17.5
ramp	10	↓	0	0	0	0	0	1.4	↓						
Z-Ioffe3	5	0.63	0	0	0	0	0	1.4	20	47	7	2120	2140	1.5	
ramp	100	↓	↓	0	0	0	0	1.4	20						
Long-Ioffe	1	0	0.63	0	0	0	0	1.4	20	53	17	2280	2320	1.6	
ramp	100	0	0.63	↓	0	0	0	↓	20						
Dimple-1	1000	0	0.63	-0.35	0	0	0	12	20	51	460	3800	3900	0.8	19→1.8
ramp	50	0	0.63	↓	↓	↓	↓	↓	20						
Dimple-2	600	0	0.63	0	15	-15	-15	2.3	20	53	200	2100	2100	1.9	2→1.4
ramp	150	0	↓	0	↓	↓	↓	↓	↓						
Exp trap	~20	0	0.13	0	2	-2	-2	3.3	5.2	44	109	500	500	3.36*	
ramp	30	0	↓	0	↓	↓	↓	↓	↓						
detection	1	0	0.55	0	-15	-15	-15	3.3	5.2	190	36	130	130	3.3	

Table 3.1: Sequence of magnetic traps. Listed is the duration Δt, the currents of the involved wires on the chip, the external magnetic fields ($B_z = 0$ for all traps), the calculated distance from the chip surface z_0, the calculated trap frequencies (in general $(f_1, f_2, f_3) \neq (f_x, f_y, f_z)$), and the calculated (measured, where marked with *) field B_0 at the center of each magnetic trap, as well as the stop frequencies of the evaporative cooling ramps ν_{RF}. The signs of the currents are chosen with respect to the coordinate system, i. e. negative currents flow in negative x- or y-direction. For wire labels, see figure 3.2 and figure 3.19.

Chapter 4

Experimental results: spin squeezing and entanglement

In this chapter, before turning to the main results of this thesis, I present a series of measurements aimed at the characterization of the microwave near-field potentials. We first demonstrate the state-selective splitting of small BECs and determine the dependence of the splitting distance on the microwave power injected into the CPW. We then analyze a dynamic splitting method, where the traps for $|0\rangle$ and $|1\rangle$ are abruptly separated and the states oscillate in the shifted potentials. We find that the atomic motion for small splitting distances is governed by mean-field effects which can be reproduced well by our simulations. A high degree of coherence is maintained during this process, which is crucial for the use of our technique in an atomic interferometer and for the generation of entangled states.

Finally, we tomographically analyze the BEC after state-selective splitting and recombination to show that the resulting multi-particle state is spin squeezed and a useful resource for quantum metrology. Following a detailed noise analysis, leading to suggestions for future improvements of our experimental technique, the Wigner function of the squeezed state is reconstructed.

4.1 State-selective splitting of a BEC

To characterize the state-selective potential we split an atomic ensemble employing various microwave powers, detunings, and splitting schemes. We start by preparing a small BEC with a few hundred atoms in our experimental trap ($f_x = 109\,\mathrm{Hz}$, $f_y = f_z = 500\,\mathrm{Hz}$, $z_0 = 44\,\mu\mathrm{m}$, see also section 3.8). At the position of this trap, the microwave near-field has a strong gradient along x and z. To split the BEC, we first apply a $\frac{\pi}{2}$-pulse to create an equal

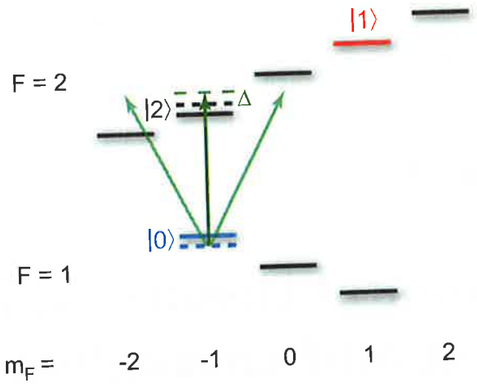

Figure 4.1: Level scheme for adiabatic and large dynamic splitting. The microwave in the CPW is blue-detuned by $\Delta \equiv \Delta_{1,-1}^{2,-1}$ from the transition $|0\rangle \leftrightarrow |F = 2, m_F = -1\rangle \equiv |2\rangle$, leading to an energy shift of states $|0\rangle$ and $|2\rangle$. The magnitude of Δ is exaggerated for clarity. State $|1\rangle$ is very weakly affected because the microwave is far detuned from all transitions connecting to this state.

superposition of the two states. We then ramp up the microwave power launched into the waveguide and subsequently image the atoms in situ, i. e. with a $TOF = 0.2\,\mathrm{ms}$. For the following experiments, the microwave is blue-detuned by $\Delta \equiv \Delta_{1,-1}^{2,-1}$ from the transition $|0\rangle \leftrightarrow |F = 2, m_F = -1\rangle \equiv |2\rangle$, where Δ is on the order of a few tens to hundreds of kHz. Since the Zeeman splitting between the m_F-sublevels is $2.3\,\mathrm{MHz} \gg \Delta/(2\pi)$, this couples mainly the states $|0\rangle$ and $|2\rangle$, which are both shifted in energy (see figure 4.1). Atoms in state $|1\rangle$ are essentially unaffected by the microwave because it is far off resonance for all transitions connecting to this state. Therefore, in a microwave intensity gradient, only the trap for state $|0\rangle$ is shifted whereas the trap for state $|1\rangle$ remains at the position of the static magnetic trap.

For our parameters $|\Omega_{\mathrm{mw}}|^2 \ll |\Delta|^2$, so that the energy shift of state $|0\rangle$ is well approximated by equation (1.10), i. e. it is proportional to the microwave power P_{mw} and inversely proportional to the detuning Δ. For quantitative calculations, we simulate the microwave near-field using the microwave current distribution found in 3.1.1 and find the resulting energy shifts by diagonalizing the full dressed-state Hamiltonian (1.7).

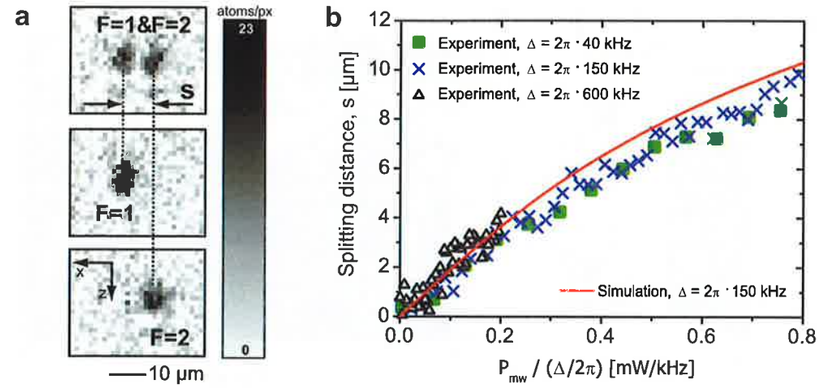

Figure 4.2: Adiabatic splitting. **a**, Absorption images of the adiabatically split BEC ($P_{\mathrm{mw}} = 120$ mW, $\Delta(\mathbf{r}_m) = 2\pi \times 150$ kHz). By imaging both hyperfine states simultaneously (top), only $F = 1$ (middle), or only $F = 2$ (bottom), the state-selectivity of the splitting is established. **b**, Measured splitting distance s as a function of P_{mw}/Δ for different values of Δ, as indicated. The solid line is the result of a simulation using the microwave current distribution found by our field-imaging method (see section 3.1.1).

4.1.1 Adiabatic splitting

In a first set of experiments, we ramp up the microwave power within 150 ms, which is slow compared to the trapping frequencies. The two states can thus adiabatically follow the change in their respective trapping potentials. We measure the resulting splitting of the two states as a function of P_{mw} and Δ. Figure 4.2 shows the in-situ images of a split condensate and the splitting distance as a function of P_{mw}/Δ. The curves lie on top of each other for different Δ, which confirms that we are in the regime $|\Omega_{\mathrm{mw}}|^2 \ll |\Delta|^2$.

The splitting is mainly due to the strong gradient of $|\Omega_R(\mathbf{r})|$ at the position of the magnetic trap $\mathbf{r}_m$, whereas the variation of $\Delta(\mathbf{r})$ is comparably weak. Although we know from the microwave field characterization and simulations that the gradients along the x and z-direction are of comparable magnitude, the cloud is almost solely split along x. This is because the trap frequency along x is five times weaker than along z which leads to a 25 times larger effect in this direction. The splitting along z is below our imaging resolution. The maximally applied $P_{\mathrm{mw}} = 120\,\mathrm{mW}$ corresponds to $\Omega_{\mathrm{mw}}(\mathbf{r}_m) = 2\pi \times 122$ kHz, which we measure independently by driving resonant Rabi oscillations with the microwave near-field. Note that for $\Delta > 0$, the repulsive microwave potential pushes state $|0\rangle$ into regions where

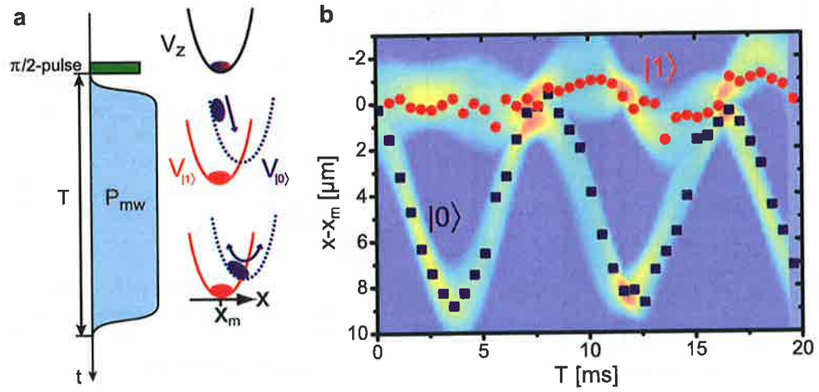

Figure 4.3: Dynamic splitting. **a**, Sequence used to record the dynamic splitting: after preparing an equal superposition of $|0\rangle$ and $|1\rangle$, the microwave power is ramped up within 50 μs, fast compared to the trap frequencies. State $|0\rangle$ starts to oscillate in its suddenly shifted trap. After a time T, we ramp down the microwave again within 50 μs and image the atoms in situ. **b**, Position of the two states as a function of time. Shown are experimental data (c.o.m. position) together with the result of a dynamical simulation of the coupled Gross-Pitaevskii equations (longitudinal density integrated along the tight confinement axes of the cylindrical trap).

$\Omega_{\mathrm{mw}}(\mathbf{r}) \ll \Omega_{\mathrm{mw}}(\mathbf{r}_m)$ so that $|\Omega_{\mathrm{mw}}|^2 \ll |\Delta|^2$ is satisfied.

Our simulation matches the experimental data well, confirming the accuracy of the field imaging method.

4.1.2 Dynamic splitting

In order to split and recombine a BEC in shorter times, comparable to the trap frequencies, we use a dynamic splitting method. For this, we ramp up the microwave within 50 μs, which is slow compared to the internal state dynamics but fast compared to the trap frequencies and thus the motion of the atoms.

Large splitting distance

For $\Delta = 2\pi \times 600\,\mathrm{kHz}$ and $P_{\mathrm{mw}} = 120\,\mathrm{mW}$, the trap for state $|0\rangle$ is shifted by $s = 4.3\,\mu\mathrm{m}$. The atoms in state $|0\rangle$ suddenly 'see' a modified potential and start oscillating in the shifted trap (figure 4.3) with the frequency of this trap

$\bar{f}_x = 116\,\mathrm{Hz}$ and with an amplitude of $2s$. After each full oscillation, the two states overlap again and due to collisions some momentum is transfered to state $|1\rangle$. Our collaborator LI Yun has simulated the atomic motion by solving the quasi-3D coupled Gross-Pitaevskii equations (rotationally symmetric traps, $f_\perp = 500\,\mathrm{Hz}$, $f_x = 116\,\mathrm{Hz}$, splitting only along x). The calculations reproduce the experimental findings very well; the results are shown in figure 4.3 b.

For the spin squeezing experiments, the distance by which the two states are separated can be much smaller, what counts is the wave function overlap. On the other hand, it is crucial to minimize the admixture of other states (with a different magnetic moment) to the clock states to keep their good coherence properties. For the experiments on spin squeezing we therefore perform a slightly different splitting sequence as described in the following.

Small splitting distance

As can be seen from equations (1.10) and (1.11), the admixture of other states to the clock states is inversely proportional to the detuning. For this reason, for the following experiments, we choose a large blue detuning $\Delta_{1,0}^{2,0} = 2\pi \times 12\,\mathrm{MHz}$ with respect to the $|F = 1, m_F = 0\rangle \leftrightarrow |F = 2, m_F = 0\rangle$ transition. Thus, the dressing is very small and the admixture is on the order of only one percent. However, as a consequence, also the achievable splitting distance between the two traps is significantly smaller. Because the microwave is blue detuned for all hyperfine transitions, both states are affected and their traps are shifted in opposite directions in the near-field gradient. Along x, the trap for state $|0\rangle$ is pushed by 0.13 μm away from the waveguide whereas the trap for state $|1\rangle$ is pulled by 0.39 μm toward the guide, resulting in a total splitting of $s = 0.52\,\mu\mathrm{m}$. For all following experiments, we use a BEC with $N = 1250$ and the splitting is much smaller than the BEC radius of 3.9 μm [85]. The shift in z-direction for both states is on the order of 0.02 μm. We have not imaged the motion of the two states in situ, but we know from simulations that for such small trap separations the trapping frequencies do not change.

In spite of the small trap splitting, due to mean field effects, the two states almost completely separate and the oscillation period of the states increases compared to $1/f_x = 9.2\,\mathrm{ms}$. Simulations by LI Yun show that the condensate is split by 3 μm and the wave function overlap λ is reduced to almost 0. On the other hand, the states overlap again by $\lambda = 90\,\%$ after

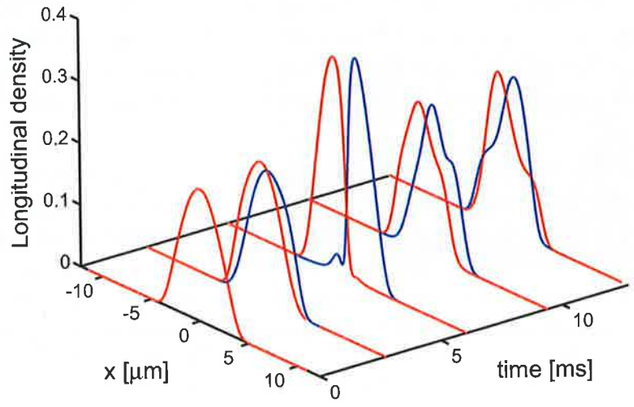

Figure 4.4: Wavefunction dynamics for small splitting distance. Longitudinal densities for the two states $|0\rangle$ (blue) and $|1\rangle$ (red) integrated along the tight confinement axes of the cylindrical traps, calculated from a dynamical simulation. The total number of atoms $N = 1250$, and the trap frequencies $f_\perp = 500\,\mathrm{Hz}$, $f_x = 109\,\mathrm{Hz}$. The displacement of the traps for state $|0\rangle$ and $|1\rangle$ are $0.13\,\mu\mathrm{m}$ and $0.39\,\mu\mathrm{m}$, respectively, leading to an asymmetric evolution of the two wave functions. Figure adapted from [117].

12.7 ms (see figures 4.4 and 4.5). Here, the density overlap is calculated as

$$\lambda = \frac{\int dr^3 |\phi_0|^2 |\phi_1|^2}{\sqrt{\int dr^3 |\phi_0|^4 \int dr^3 |\phi_1|^4}}, \tag{4.1}$$

where ϕ_0 and ϕ_1 are the states' spatial modes.

Note that the large separation is *not* a demixing effect due to the slightly different scattering lengths of the two states but predominantly due to the mean field repulsion in an asymmetric potential for states $|0\rangle$ and $|1\rangle$ itself. This can be seen from a simulation where the inter- and intra-state scattering lengths have been set equal ($a_{00}^{\mathrm{sim}} = a_{01}^{\mathrm{sim}} = a_{11}^{\mathrm{sim}} \equiv a_{00}$), and the dynamic is barely different from that shown in figure 4.4.

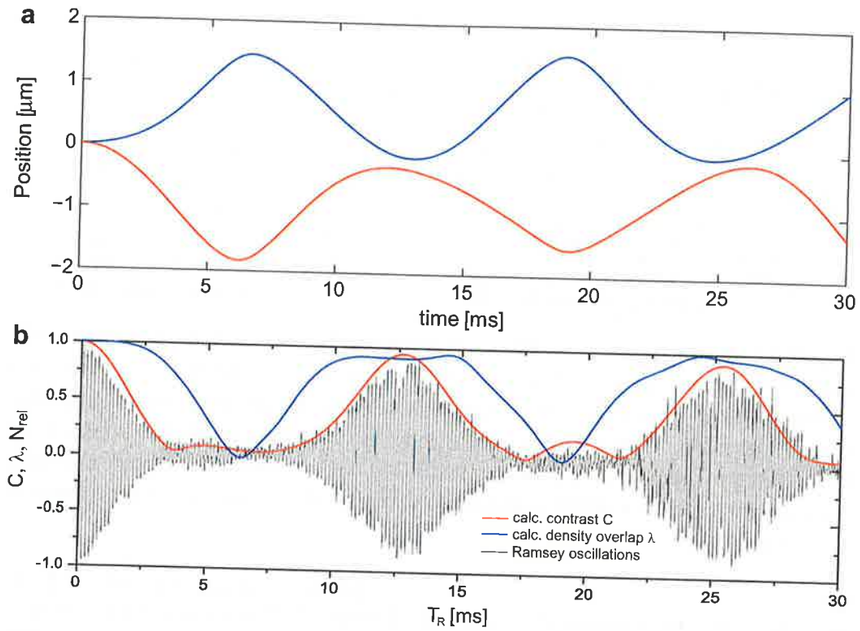

Figure 4.5: Atomic motion and contrast for small splitting distance. **a**, Simulated center of mass position of the two states (blue: $|0\rangle$, red: $|1\rangle$) in the state-selectively split potential used for the squeezing experiments, as a function of time. The slightly asymmetric splitting of the potentials results in an asymmetric oscillation. **b**, Measured Ramsey fringes in the normalized population difference N_{rel}. The splitting and recombination of the BEC modulates the fringe contrast. The simulated contrast C (red) and density overlap λ (blue) are shown for comparison.

4.2 Coherence

To test the coherence of the state-selective spitting process, we embed it in a Ramsey interferometer sequence. For this, we simply apply a second $\frac{\pi}{2}$-pulse directly after the microwave has been ramped down. Figure 4.5 b shows the measured Ramsey fringes in $N_{\mathrm{rel}} = \frac{N_1 - N_0}{N_1 + N_0}$ as a function of the time between the two pulses T_R. It also shows the calculated contrast

$$C = \frac{2 \int d^3r \hat{\Psi}_0^\dagger \hat{\Psi}_1}{\int d^3r \hat{\Psi}_0^\dagger \hat{\Psi}_0 \int d^3r \hat{\Psi}_1^\dagger \hat{\Psi}_1} \tag{4.2}$$

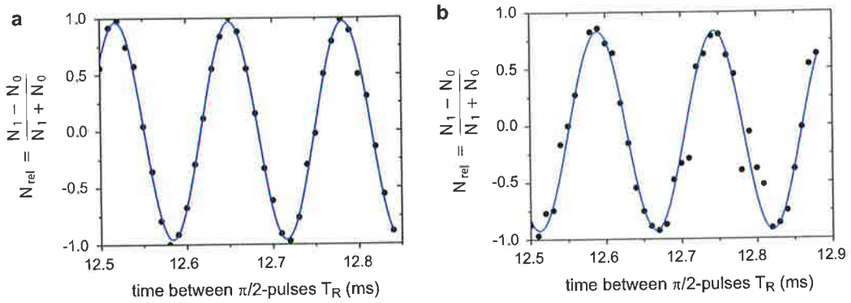

Figure 4.6: Ramsey interference fringes. Ramsey interference fringes in the relative atom number N_{rel}, recorded by varying the delay T_R between two $\frac{\pi}{2}$-pulses. **a**, Ramsey fringes in the reference sequence in a static magnetic trap. The contrast obtained from a sinusoidal fit (blue line) is $C = (96 \pm 1)\,\%$. **b**, Ramsey fringes in the squeezing sequence with state-selective splitting and recombination of the BEC, embedded between the $\frac{\pi}{2}$-pulses. The contrast is $C = (88 \pm 3)\,\%$.

and the wave function overlap λ obtained from LI Yun's simulation. In fact, since our simulations of the static magnetic traps and microwave potentials have an uncertainty on the order of 10 %, we find the exact longitudinal trap frequency and splitting distance by maximizing the agreement between calculated and measured contrast. The corresponding values ($f_x = 109\,\mathrm{Hz}$, $s = 0.52\,\mu\mathrm{m}$) quoted in this thesis are obtained in this way.

As expected, the contrast drops when the two states are separated and reappears when they overlap again. Note, however, that the revivals of the contrast are much narrower in time than the revivals of the wave function overlap. This is because the former is phase sensitive, i. e. it is also decreased when the states overlap but move with respect to each other.

Figure 4.6 shows a zoom of the first revival and for comparison Ramsey oscillations recorded with the same experimental sequence but without applying the microwave near-field and splitting the BEC (the *reference measurement*). We observe a contrast of $C = (88 \pm 3)\,\%$, smaller than in the reference because the overlap of the BEC mode functions after splitting and recombination is less than unity. The difference to the contrast of 94 % predicted by the dynamical simulation can most likely be explained by small motion in the transverse direction which is excited in the experiment but not modeled. The contrast could be increased by optimal control of the atomic motion rather than abrupt switching of the potentials, as described in [48]. The high contrast at the revival proves that the splitting is a coherent process. The Ramsey sequence used here implements an atomic interferometer with internal-state labeling of the interferometer arms.

The Ramsey oscillation frequency in the reference measurement is 7.58 kHz, dominated by the microwave level shifts during the $\frac{\pi}{2}$-pulses: the microwave and rf frequencies for the pulses are adjusted such that the drive is resonant *while the microwave is on* ($E_{\mathrm{ls}} \neq 0$, see section 1.1.4). The energy difference between the levels in the undriven system accordingly differs by $E_{\mathrm{ls}} = \hbar\,\delta_{\mathrm{ls}} \approx h \cdot 7.58\,\mathrm{kHz}$ from the local oscillator frequency, which results in the measured Ramsey oscillations. Furthermore, the oscillation frequency of the Ramsey fringes decreases to 6.47 kHz in the splitting measurements. This is because of the differential energy shift experienced by the two states in the microwave near-field potential, which is therefore $\delta_{\mathrm{ls}}^{\mathrm{cpw}}/(2\pi) \approx -1.1\,\mathrm{kHz}$. This effect can be reproduced by our simulation of the trapping potentials.

Using the method explained in [47], we can calculate the reduction of the contrast due to quantum phase spreading during the squeezing time [93] and we find that it only amounts to 2 % and is hence negligible.

4.3 Spin squeezing

While the two states are separated, $\chi \neq 0$ and the initial coherent state evolves into a squeezed spin state. To achieve a large amount of squeezing, the time of the first Ramsey revival should coincide with the best squeezing time. We estimate the latter by calculating the two-mode model spin squeezing in presence of particle losses for the stationary solution of the Gross-Pitaevskii equation, with a trap separation s [117]. This corresponds to a 'time averaged χ', since the two states overlap more in the beginning and the end of the dynamical evolution but less in the middle, compared to the stationary solution. The calculated nonlinear parameter is $\chi^{2m} = 0.49\,\mathrm{Hz}$ and the best squeezing is reached around $T_{\mathrm{best}} = 14.5\,\mathrm{ms}$, with a broad minimum and a squeezing parameter $\xi^2 < 0.1$ at the time of the revival.

4.3.1 Spin tomography

To measure the squeezing, we choose the Ramsey time T such that the Ramsey contrast is maximal and the Rabi vector and the state vector are aligned or anti-aligned (see figure 2.3). In practice, we fit the Ramsey oscillations in relative atom number at the revival with a sine curve, as in figure 4.6, and choose T where the fitted curve crosses 0 with positive (negative) slope to turn the state clockwise (anti-clockwise). We find $T = 12.706\,\mathrm{ms}$ in figure 4.6 and similarly for all squeezing measurements $T \approx 12.7\,\mathrm{ms}$. We then vary

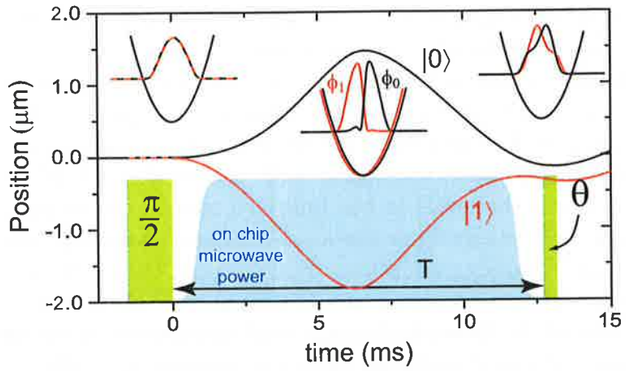

Figure 4.7: Experimental squeezing sequence. In between the pulses for internal-state manipulation (green), the state-dependent microwave potential is turned on (blue; pulse durations and microwave ramp times exaggerated for clarity). It dynamically splits and recombines the two BEC components, so that $\chi > 0$ during the time T. The simulated center-of-mass motion of the two states $|0\rangle$ (black) and $|1\rangle$ (red) is shown as a function of time. Insets: corresponding BEC mode functions ϕ_0 and ϕ_1 along the splitting direction in their respective potentials at the beginning, in the middle, and at the end of the sequence.

the duration of the second pulse to turn the state around its mean spin by different turning angles θ (see figure 4.7).

To achieve the highest possible data quality, we let the experiment run over night, when disturbances on the power line due to other activity in the building (e. g. running elevators) are reduced to a minimum and our atom number preparation is stable. To measure the squeezing for a variety of turning angles with low statistical uncertainty, we need to run the experiment for several nights. From night to night, our experimental parameters vary slightly, as detailed in table 4.1. The reason for this is that each evening, we first do a number of calibration measurements to find the correct atom number, the relative detectivity, the correct length of a $\frac{\pi}{2}$-pulse, and the Ramsey phase. It can happen that by the time we start the actual squeezing measurement, N or $\langle S_z \rangle$ are different from what we prepared in the beginning of the evening. Possible reasons for this are thermal drifts in the laser beam alignment which lead to drifts in the power in the MOT beams and thermal drifts of current sources and rf amplifiers. Since adjusting the atom number requires to redo all other calibration measurements, we usually accept a small derivation from $N = 1250$. Note however, that we do not see a significant

measurement night	$\theta_{\min}$ [°]	$\theta_{\max}$ [°]	shots per turning angle M	N	$\langle S_z \rangle$	T [ms]	$\Omega/(2\pi)$ [kHz]
05.08.09	-90	0	135	1254 ± 45	-16	12.742	2.040
24.07.09	0	22	370	1243 ± 47	64	12.643	2.025
06.08.09	22	95	73	1276 ± 45	-7	12.642	2.037
16.07.09	179	197	174	1711 ± 73	-201	12.639	2.018
21.07.09	101	130	174	1222 ± 42	-153	12.773	2.010
22.07.09	145	360	165	1473 ± 73	-142	12.691	2.015
26.08.09	0	20	590	1264 ± 63	34	12.627	2.097
24.08.09	30	360	348	1307 ± 46	26	12.627	2.071

Table 4.1: Experimental parameters for different data sets. The bottom two rows are data for the reference measurement.

dependence of the results on these effects and that for the most relevant data between $-90° < \theta < 90°$, great care was taken to prepare the correct atom number and an equal superposition.

The data is analyzed as described in section 3.7, a summary of the procedure can be found in appendix C. In short, we correct the raw atom numbers by multiplying them with the factors obtained from the imaging calibration, take out total atom number fluctuations by detecting both states within one experimental cycle, and subtract the independently measured imaging noise. In the data for $90° < \theta < 360°$ a slow drift of S_z is observed. We correct for this technical drift by subtracting a filtered data set from the respective raw data, using a second order Savitzky-Golay filter [118] over 300 shots. For comparison with theory we use $N = 1250 \pm 45$.

Figure 4.8 shows $S_z(\theta)$ for $-90° < \theta < 90°$, obtained during three measurement nights. After statistically analyzing the raw-data we get $\Delta S_\theta^2(\theta)$, which is shown in figure 4.9. Results for a squeezed state are shown in comparison with results from the reference measurement. I plot the normalized variance $\Delta_n S_\theta^2 = 4\,\Delta S_\theta^2/\langle N \rangle$ [119], so that $\Delta_n S_\theta^2 = 0\,\mathrm{dB}$ corresponds to the standard quantum limit. The error bars are calculated as $\Delta(\Delta S_\theta^2) = \sqrt{2/M}\Delta S_\theta^2$, where M is the number of measurements per turning angle [115]. Here, I use that the probability distribution of S_θ for any turning angle is approximately Gaussian for our parameters, as observed in the measured data.

In the squeezed state, the spin noise $\Delta_n S_\theta^2$ falls significantly below the standard quantum limit, reaching a minimum of $\Delta_n S_\theta^2 = (-3.7 \pm 0.4)\,\mathrm{dB}$ at $\theta_{\min} = 6°$. Together with the corresponding interference contrast of $C = (88 \pm 3)\,\%$, this results in a squeezing parameter of $\xi^2 = (-2.5 \pm 0.6)\,\mathrm{dB}$, proving that the state is a useful resource for quantum metrology and that

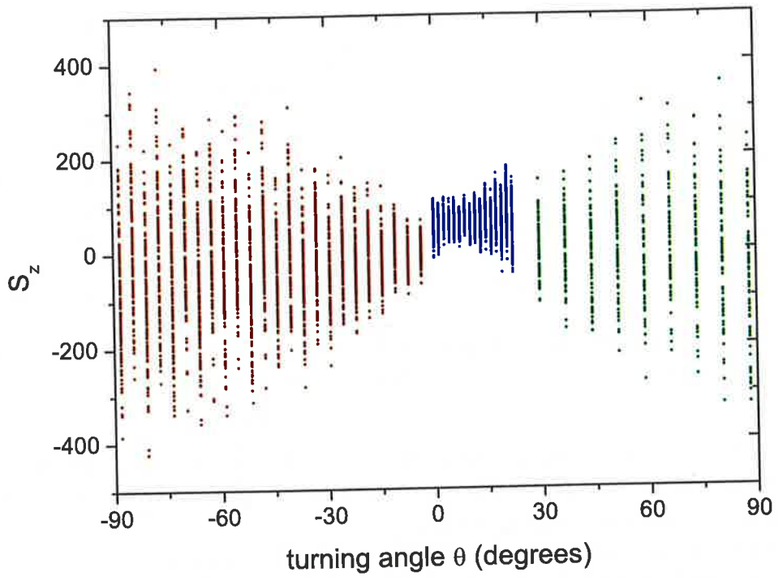

Figure 4.8: Measured S_z as a function of the turning angle θ. Shown are the measurements of three nights (red: 5.8.09, blue: 24.7.09, green: 6.8.09) for turning angles $-90° < \theta < 90°$ (compare with table 4.1).

the condensate atoms are entangled. The reference measurement, by contrast, stays above the standard quantum limit for all values of θ. This data corresponds to a state tomography and will be used in section 4.5 to reconstruct the Wigner function of our produced spin squeezed state. Note, that the amount of squeezing does not significantly depend on whether we use the atom number calibration via σ_{eff} or via shot noise (section 3.7). Also, even if we do not subtract the imaging noise, we still achieve a reduction in spin noise of $-2.3\,\text{dB}$.

The spin noise reduction obtained from Li Yun's simulations is shown along with the data. The blue line shows the expected squeezing, taking into account the motional dynamics as well as atom losses (see section 2.2.7). The maximal reduction in variance expected from the simulation is $-12.8\,\text{dB}$, significantly larger than observed. The red line, which describes our data well, additionally includes several technical noise sources which I will describe in detail in the following.

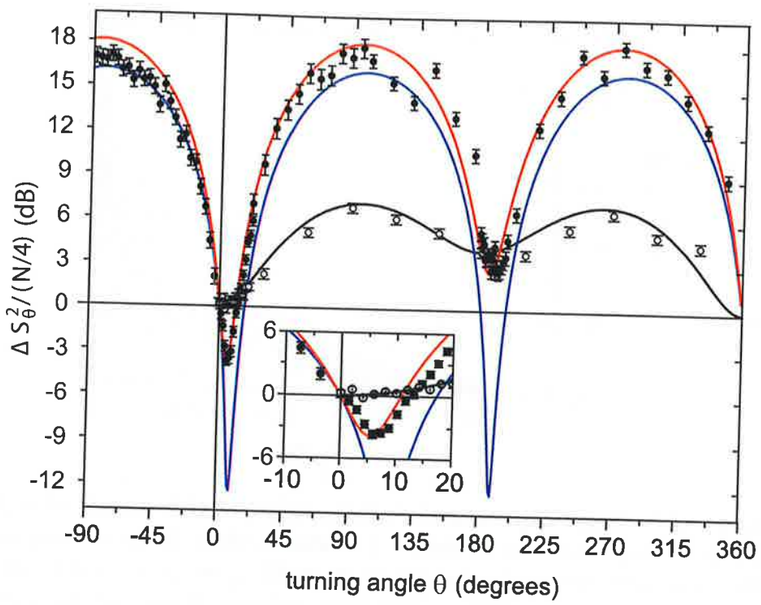

Figure 4.9: Spin noise tomography of the spin squeezed BEC. Observed spin noise for the spin-squeezed state (solid circles) and for a coherent spin state (reference measurement, open circles). The normalized variance $\Delta_n S_\theta^2 = 4\,\Delta S_\theta^2/\langle N\rangle$ is shown as a function of the turning angle θ, with statistical error bars. The error in θ lies within the plotted data points. In the squeezed state, a spin-noise reduction of $(-3.7 \pm 0.4)\,\text{dB}$ is observed for $\theta_{\text{min}} = 6°$, corresponding to $\xi^2 = (-2.5 \pm 0.6)\,\text{dB}$ of metrologically useful squeezing for our Ramsey contrast of $C = (88 \pm 3)\,\%$. Solid lines are results from the dynamical simulation. Blue: squeezed state with losses but without technical noise; red: squeezed state with losses and technical noise; black: reference measurement with losses and technical noise.

4.3.2 Multi-particle entanglement

In section 2.2.8, the method of [46] to experimentally determine the amount of entanglement of a spin squeezed state was presented. If we plot our data point $\left(\langle S_x\rangle, \Delta_n S^2_{\theta,\text{min}}\right)$ together with the limits for multi-particle entanglement calculated in [46], we see that it lies below the $S = 3/2$ line (see figure 4.10). This implies that the condensate atoms are entangled in clusters of at least 4 ± 1 particles.

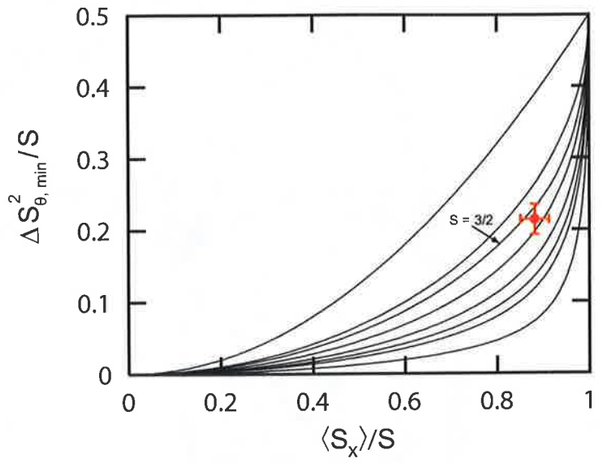

Figure 4.10: Experimental determination of the depth of entanglement. Reproduction of figure 2.6 with a data point corresponding to the measured spin noise reduction of $\Delta_n S^2_{\theta,\min} = (-3.7 \pm 0.4)\,\mathrm{dB}$ and contrast of $C = (88 \pm 3)\,\%$. The lines indicate (from top to bottom) $S = (\frac{1}{2}, 1, \frac{3}{2}, 2, 3, 4, 5, 10)$. The data point lies below the $S = \frac{3}{2}$ line, proving that the produced spin squeezed state is at least 4 ± 1 particle entangled. Figure adapted from [46].

4.4 Analysis of technical noise

Three major differences between the expected and the measured variance in S_θ become apparent in graph 4.9. First, the measured ΔS^2_θ is larger around $\theta = 180°$ than it is around $\theta = 0°$, both for the squeezing and the reference measurement. Second, the achieved squeezing at $\theta_{\min} \approx 6°$ is less than predicted and third, in the reference measurement $\Delta_n S^2_\theta > 0\,\mathrm{dB}$ for large turning angles. All of these differences can be explained by technical noise.

4.4.1 Fluctuating microwave power during pulses

The power of the microwave used for the two-photon drive fluctuates slightly from shot to shot. As a result, the microwave level shifts and thus the detuning during the pulses fluctuate. On the Bloch sphere, a detuning during the preparation pulses can be depicted by the Rabi vector not pointing perfectly on the equator but slightly above or below (see section 2.1.1). The effect is not noticeable for the first $\frac{\pi}{2}$-pulse but plays an important role for the

second. While for small turning angles (and for $\theta \sim 360°$) it is negligible, it contributes significantly to ΔS^2_θ around $\theta \sim 180°$: the additional variation of S_θ due to this effect is $\Delta S^2_\theta = [\Delta\delta_{\mathrm{ls}}/\Omega_R \cdot N/2 \cdot (1 - \cos(\theta))]^2$, where Ω_R is the two-photon Rabi frequency.

With a directional coupler directly before the microwave horn and a detector we measure a variation of the power of the microwave used for the two-photon drive from shot to shot of $\frac{\Delta P}{P} = 0.5\,\%$ r. m. s. The frequency of the Ramsey oscillations in the reference measurement is determined by the microwave level shifts during the pulses, which we can therefore estimate to be $\delta_{\mathrm{ls}}/(2\pi) = 7.6\,\mathrm{kHz}$. The level shifts are proportional to the microwave power and the detuning thus fluctuates by $\Delta\delta_{\mathrm{ls}}/(2\pi) = 5 \times 10^{-3} \cdot 7.6\,\mathrm{kHz} = 38\,\mathrm{Hz}$ r. m s. This leads to an additional variation of $\Delta S^2_\theta = 510 = 0.4\,N$ for $\theta = 180°$ which is the reason for ΔS^2_θ not reaching the SQL at $\theta = 180°$.

A second effect of the fluctuating microwave power is that the turning angle θ varies by $\frac{\Delta\theta}{\theta} = \frac{1}{2}\frac{\Delta P}{P} = 0.25\%$ r. m. s. (the factor $\frac{1}{2}$ comes from $\theta \propto \Omega_R \propto P^{1/2}$). However, from our simulations we find that this effect is negligible and in figure 4.9, the error bars of θ lie within the data points plotted.

In the future, we plan to use state $|1, 0\rangle$ as intermediate state for the two-photon transition. Since the transition $|1, 0\rangle \leftrightarrow |2, 1\rangle$ is stronger than the transition $|1, -1\rangle \leftrightarrow |2, 0\rangle$ by a factor $\sqrt{3}$, we should be able to reduce the ratio $\delta_{\mathrm{ls}}/\Omega_R$ and thus lessen the effect of the fluctuating microwave power. Additionally, one could actively stabilize the microwave power. However, keep in mind that the achievable squeezing for $\theta \approx 6°$ is not limited by this effect but by phase noise, as described in the following section.

4.4.2 Phase noise

A fluctuating phase from shot to shot between the Rabi and the state vector increases ΔS^2_θ significantly. Phase noise can be depicted as a smearing of the state along the equator of the Bloch sphere and it has the largest absolute effect for a $\frac{\pi}{2}$- and $\frac{3\pi}{2}$-pulse, since these pulses translate phase directly into population S_z. However, the squeezed state is already significantly broadened in the phase direction and the largest relative effect of phase noise is just for $\theta \sim \theta_{\min}$.

To reproduce the measured data, we have to introduce in our theory an additional technical phase noise of $\Delta\varphi = 3.2°$ for the reference measurement (black line in figure 4.9) and $\Delta\varphi = 8.2°$ for the squeezing measurement

noise source	simulated sensitivity	measured sensitivity	fluctuations (r. m. s.)	resulting phase noise $\Delta\varphi$
N (ref)			45	1.0°
B_x	0.5°/mG	< 1°/mG	0.2 mG	< 0.2°
hf generators			see text	∼ 1°
total reference				∼ 1° − 2°
N (sq)			45	1.9°
B_x		1.0°/mG	0.2 mG	0.2°
B_y	4.0°/mG	5.0°/mG	see text	see text
B_z	0.3°/mG	0.3°/mG	0.3 mG	0.1°
I_{LI}	0.15°/μA	0.18°/μA	∼ 10 μA	∼ 2°
$I_{\mathrm{CPW},1}$	1.2°/μA	1.4°/μA	< 1 μA	< 1.4°
$I_{\mathrm{CPW},2}$	0.9°/μA	1.1°/μA	< 1 μA	< 1.1°
$I_{\mathrm{CPW},3}$	0.3°/μA	0.6°/μA	< 1 μA	< 0.6°
P_{mw}	38°/mW	43°/mW	60 μW	2.6°
hf generators			see text	∼ 1°
total squeezing				> 4°

Table 4.2: Phase noise budget. Contribution of different noise sources in the experiment to total phase noise. For the reference measurement (top four rows), only fluctuations in N, fluctuations in B_x, and high frequency generator phase noise contribute. For the squeezing measurement (bottom) a variety of phase noise sources exist. The sensitivities are calculated with the help of our trap simulation and measured using the squeezing sequence with $\theta = \theta_{\mathrm{min}}$.

(red line in figure 4.9). The possible reasons for this noise are manifold since a fluctuation of the phase of either the Rabi or the state vector has the same effect, and there are many possible origins of phase fluctuations of the state. Table 4.2 lists all noise sources identified in the experiment and their contribution to the total phase noise in the reference and squeezing measurements. They are described in detail in the following.

Atom number fluctuations

As shown in section 2.2.7, for ^{87}Rb with $a_{00} \neq a_{11}$, the energy difference between the two clock states and thus the phase evolution rate depend on the total atom number. This collisional clock shift can be estimated for the reference measurement as [52]

$$\nu_{\mathrm{coll}} = \frac{\hbar}{m} n (a_{11} - a_{00}), \tag{4.3}$$

where m is the ^{87}Rb mass and n is the mean density. For our trap parameters with $N = 1250$ we calculate $n = 7.2 \times 10^{13}\,\mathrm{cm}^{-3}$ [85] and thus get $\nu_{\mathrm{coll}} = 15\,\mathrm{Hz}$. A fluctuation of the total atom number of $\Delta N = 45$ leads to a phase noise after T_R of $\Delta\varphi = 1.2°$ (note that $n \not\propto N$).

In our calculation with the modulus-phase approach, we apply an averaging of N over a normal probability distribution with $N = 1250$ and $\Delta N = 45$, where N is taken between 1100 and 1400 atoms (as it is done in the experiment by post selection). The thus calculated collisional phase noise is $\Delta\varphi = 1.0°$ for the reference measurement and $\Delta\varphi = 1.9°$ for the squeezing measurement. The fluctuations in total atom number have thus little effect on the attainable squeezing, since it is dominated by other technical phase noise. This is confirmed in the experiment where tighter (±75 atoms) or wider (±250 atoms) post selection does not change the amount of squeezing.

Local oscillator phase noise

The phase stability of the Rabi vector is determined by the stability of our microwave and radio frequency generators used for the two-photon drive. We use an Agilent E8257D microwave generator (with UNX low phase noise option) to generate a 10 MHz reference signal onto which all other generators are locked. The absolute phase noise specified for this device is $\mathcal{L} = -81\,\mathrm{dBc/Hz}$ at 100 Hz offset frequency. From this, we can calculate the phase noise after T_R to be $\Delta\varphi = 0.4°$ [120]. The radio frequency generator phase noise is specified as −65 dBc within a 30 kHz band from which we calculate $\Delta\varphi = 4 \times 10^{-4°}$. The amplifiers and switches add some more phase noise which is hard to quantify but should be on the same order. The delay generator used to time the experiment has a jitter of 100 ps, which leads to a phase noise of $\Delta\varphi = 3 \times 10^{-4°}$.

Besides the specified oscillator phase noise, also a shot-to-shot fluctuation of the 10 MHz reference signal may lead to phase noise. For our experiments, fluctuations on a timescale of a few seconds (experiment repetition rate) to a few minutes are most important, since drifts on a longer timescale can be identified in the data. The relative stability of the reference $\Delta f/f$ translates to phase noise as $\Delta\varphi = \Delta f/f \cdot f_0 T_R$, where $f_0 = 6.8\,\mathrm{GHz}$. A relative stability of $\Delta f/f = 3 \times 10^{-11}$ already results in phase noise of $\Delta\varphi = 1°$. According to the specifications of the signal generator, the temperature coefficient for the relative stability is better than $5 \times 10^{-9}/\mathrm{K}$. Thus, temperature fluctuations in the lab of only a few percent of a degree Celsius could already lead to phase noise of a few degrees. Additionally, a fluctuation of the line voltage of 10 % results in a fluctuation of the clock of less than 2×10^{-10}.

We measure the phase stability of our microwave generator by mixing

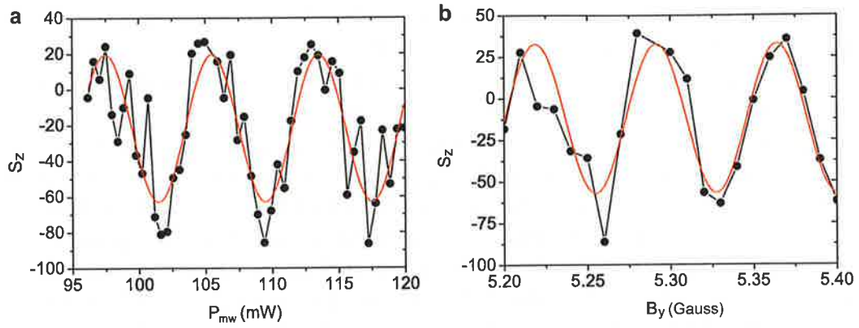

Figure 4.11: Dependence of S_z on P_{mw} and B_y. Dependence of S_z on the microwave power launched into the waveguide P_{mw} (a) and the magnetic field B_y (b) during the squeezing sequence with $\theta = 6°$. For P_{mw}, the sinusoidal fit (red) yields a phase sensitivity of $\Delta\varphi = 43°/\mathrm{mW}$ at $P_{\mathrm{mw}} = 120\,\mathrm{mW}$. For B_y the fit yields $\Delta\varphi = 5.0°/\mathrm{mG}$ at $B_{y,0} = 5.2\,\mathrm{G}$

the output of two independently running generators (both Agilent E8257D) and recording the beat signal for 500 s. The Fourier transformation of this signal has a width of 0.3 Hz (FWHM) which corresponds to a phase noise of $\Delta\varphi \approx 1°$, assuming that both generators have contributed equally in this measurement.

In conclusion, it can not be excluded that the high frequency generators and the reference clock contribute significantly to the phase noise in both the reference and the squeezing measurement. On the other hand, we have seen no improvement in either measurement when we used a state-of-the-art oven controlled quartz[1] for the 10 MHz reference.

Fluctuations of P_{mw} in the CPW

As described in section 4.2, the microwave near field induces level shifts of $\delta_{\mathrm{ls}}^{\mathrm{cpw}}/(2\pi) = 1.1\,\mathrm{kHz}$. A fluctuation of the microwave power in the waveguide is translated directly into a differential energy shift between the two states and thus phase noise. We can measure the influence of a change in P_{mw} by performing exactly the same squeezing sequence as described previously with $\theta = \theta_{\mathrm{min}} = 6°$, while systematically varying the power launched into the CPW. This is a Ramsey-type experiment, but with reduced contrast since the second pulse is not $\frac{\pi}{2}$.

The result is shown in figure 4.11 a. The phase sensitivity can simply

[1] Oscilloquartz OCXO 8607-BM

be calculated as $\frac{d\varphi}{dP_{\mathrm{mw}}} = k/(2\pi) \cdot 360°$, where k is the angular frequency of a sine curve fitted to the data. We obtain a sensitivity of $\frac{d\varphi}{dP_{\mathrm{mw}}} = 43°/\mathrm{mW}$. Independently, we measure a shot to shot fluctuation of $\Delta P_{\mathrm{mw}} = 60\,\mu\mathrm{W}$, resulting in a phase noise of $\Delta\varphi = 2.6°$.

The microwave power is currently stabilized using the microwave generator's internal P-I-controller and attenuator with an external detector (see section 3.5.2). To improve the microwave stability, we will employ a combination of temperature stabilized detector, self-built P-I-controller, and variable attenuator in future experiments.

Fluctuations of the trap position

Similarly to a change in the microwave power on the CPW, any change of the trap position in the near-field gradient leads to a differential energy shift. Thus, fluctuations of the trap position induced either by fluctuating chip wire currents, fluctuating magnetic offset fields, or simply mechanical vibrations result in phase noise.

We measure a strong dependence of the phase on the magnetic field in the y-direction $\frac{d\varphi}{dB_y} = 5.0°/\mathrm{mG}$ (see figure 4.11 b), which we can reproduce with our trap simulation. At the same time, we find a large modulation of the current running through the y-Helmholtz coils during T (see figure 4.12). The peak-to-peak amplitude of this modulation is 8.5 mG and it shows a periodicity of 100 Hz. The width of the current peaks is between one and a few milliseconds, suggesting that the modulation can resonantly excite motion of the atoms in the z-direction, since $f_z = 2500\,\mathrm{Hz}$. On the other hand, the modulation is very reproducible: the shot-to-shot fluctuation of the mean magnetic field during T_R is only 0.06 mG r. m. s. and the position and shape of the peaks is unchanged from shot to shot. It is therefore hard to quantify how much phase noise is produced by this modulation, but we believe that it is one of the main effects limiting our squeezing.

The phase is also extremely sensitive to fluctuations in the current running through the Long-Ioffe wire: $\frac{d\varphi}{dI_{\mathrm{LI}}} = 0.18°/\mu\mathrm{A}$. The shot to shot fluctuation of I_{LI} are on the order of about $10\,\mu\mathrm{A}$ [107], leading to a phase noise of $\Delta\varphi \sim 2°$.

Both, the field in the y-direction and the Long-Ioffe current affect mainly the z-position of the atoms. We will replace the current source creating B_y to get rid of the modulation and, if the need arises, it is also possible to replace the Long-Ioffe source with a current source whose maximum current output is matched to I_{LI} in the experimental trap. To lessen the effect of either noise

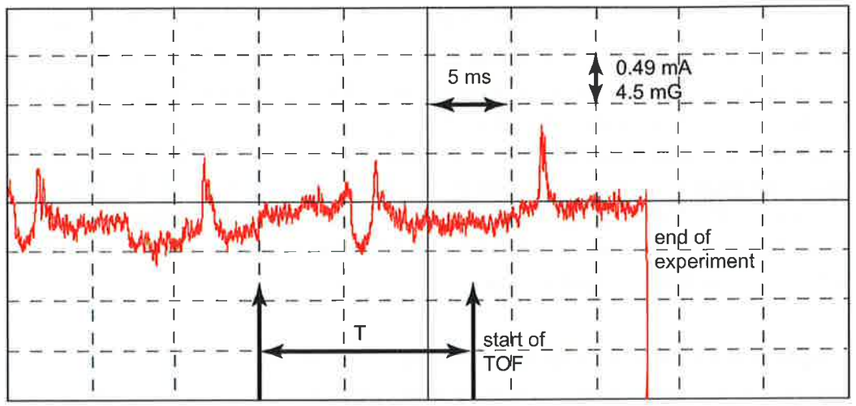

Figure 4.12: Fluctuations of B_y. Oscilloscope trace showing the modulation of the current producing B_y. The time T during which the squeezing is performed is indicated. The modulation has a peak-to-peak amplitude of 8.5 mG with spikes that are repeated at a frequency of 100 Hz.

source in future experiments, it will be essential to use an experimental trap located at a position above the CPW where the microwave near-field gradient is predominantly along the x-direction. A fluctuation of the z-position of the trap is then not translated into a fluctuation of the microwave level shifts. A positive side effect is that the state-selective splitting will then only occur in the x-direction and there will be no residual motion along z, which can lead to a diminished Ramsey contrast.

Fluctuations in the DC currents in the CPW, on the other hand, lead to fluctuations of the trap position along x and to fluctuations of B_0, and will therefore always contribute to phase noise. The sensitivities for each wire are on the order of $\frac{d\varphi}{dI_{\mathrm{cpw}}} \sim 1°/\mu\mathrm{A}$. The required currents are much lower and thus the absolute stability of the current sources $\Delta I_{\mathrm{CPW}} < 1\,\mu\mathrm{A}$ is better than that of the Long-Ioffe wire. The phase noise contribution from the three DC currents in the CPW wires combined is $\Delta\varphi < 2°$.

Very hard to quantify is the contribution of mechanical vibrations to phase noise. Our simulation shows that a position shift in the z-direction of only 10 nm results in a phase shift of $\Delta\varphi = 3.4°$. On the other hand, shot-to-shot drifts of the chip position will not result in different positions of the atoms in the microwave near-field because the trap will always be at the same position relative to the chip. Vibrations at frequencies comparable to the trap

frequencies have the largest effect, since they can resonantly excite motion of the atoms. For the experiments presented here, our setup was rigidly mounted on the optical table which in turn was not floated or vibrationally isolated in any other way. To quantify the amount of mechanical vibrations one could mount a solid state accelerometer on the back of the chip. A first step to reduce vibrations will obviously be to float the optical table, but also the cooling water running through the chip and wires leading to the chip are worth investigating.

Magnetic field noise

In the squeezing measurement, due to the microwave near field, the two clock states become dressed, which result in a differential magnetic moment and thus deteriorates their coherence properties. Phase noise can thus be caused by fluctuating magnetic fields in the laboratory. The magnetic field in the trap center of $B_0 = 3.36\,\mathrm{G}$ points in the x-direction and consequently only changes in B_x and in the CPW wire currents (see above) significantly change the amplitude of the total field felt by the atoms. We measure a sensitivity of $\frac{d\varphi}{dB_x} = 1.0°/\mathrm{mG}$ and the measured fluctuations of the magnetic field inside the μ-metal shield are $\Delta B_x = 0.2\,\mathrm{mG}$, leading to a magnetic field induced phase noise of $\Delta\varphi = 0.2°$.

In the reference measurement, because the atoms are not dressed, the phase noise due to magnetic field noise is even smaller. Using the Breit-Rabi formula (1.4) and $B_0 = 3.36\,\mathrm{G}$, we calculate a sensitivity of $0.5°/\mathrm{mG}$.

Conclusion

In conclusion, the only sources of phase noise in the reference measurement known to us are atom number fluctuations, magnetic field noise due to the quadratic Zeeman shift, and phase noise in the high frequency electronics. Although the latter is hard to quantify, the amount of noise these sources produce seems compatible with the phase noise needed to explain the data in figure 4.9.

The phase noise sources in the squeezing measurement are manifold and the largest contributors have been identified as fluctuations of the on-chip microwave power and of the trap position. By eliminating these two sources as described above, a threefold reduction of the phase noise should be feasible, greatly improving the squeezing performance.

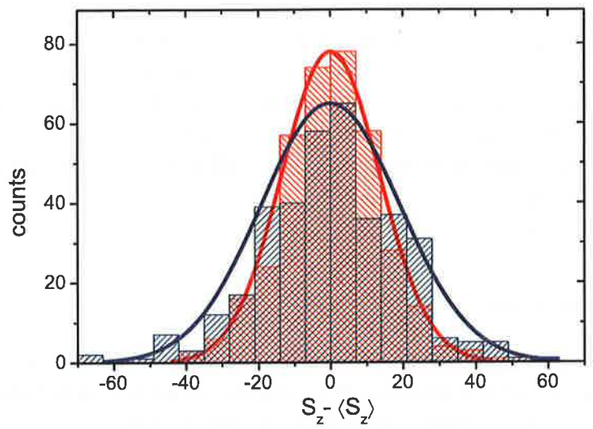

Figure 4.13: Histograms of S_θ for $\theta = 0°$ (blue) and $\theta = \theta_{\min} = 6°$ (red) shown together with fitted Gaussian distributions. The reduction of ΔS_θ^2 for $\theta_{\min}$ can be clearly seen.

4.5 Wigner function reconstruction

As described in section 2.3, the measured histograms of S_θ for angles $-90° < \theta < 90°$ are tomographic data that allow us to reconstruct the Wigner function $W(S_y, S_z)$ of the squeezed BEC, using the inverse Radon transform (equation (2.48)). The reconstruction is done on a tangent plane to the Bloch sphere, which for our case does not lead to significant distortion, since the Wigner function's extent is only about a tenth of the Bloch sphere's circumference (see figure 4.15).

Figure 4.13 shows as an example two histograms of the squeezed state for $\theta = 0°$ and $\theta = \theta_{\min} = 6°$, together with fitted Gaussian distributions. Note that for the Wigner function reconstruction, the imaging noise cannot be subtracted as it was done for figure 4.9, since the complete distributions of S_θ and not just the variances are needed. The obtained Wigner function is thus strictly speaking a convolution of the state's real Wigner function and a Gaussian distribution with a width $\Delta S_{z,\text{im}}$ given by the imaging noise (see also section 3.7).

For the reconstruction, we should ideally use a great number of high resolution probability distributions $p(S_\theta)$, requiring thousands of measurements per turning angle θ for hundreds of turning angles. In practice, we can take only a limited number of measurements (see table 4.1 and figure 4.8) at turning angles which are spaced between $1.5° < d\theta < 5°$. While the number of turning angles seems to be sufficient for an artifact-free reconstruction, we have to apply some processing of the histograms for each angle to achieve satisfactory results.

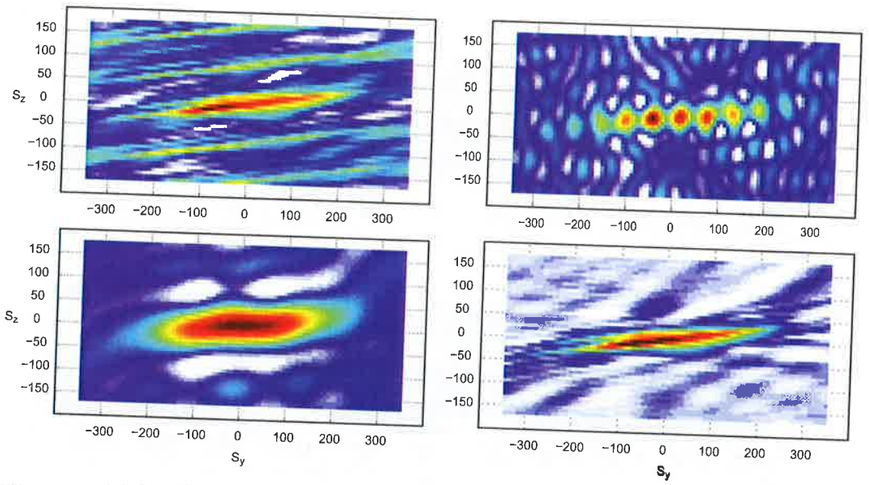

Figure 4.14: Choice of $d\eta$ and $\eta_{\max}$ for reconstruction. If the step size of the integration variable $d\eta$ is chosen too large, the Wigner function is repeated periodically (top left). If the summation boundary $\eta_{\max}$ is chosen too small, the Wigner function is artificially broadened (bottom left), if it is chosen too large, interference effects occur (top right). For comparison, the reconstruction with optimized values for $d\eta$ and $\eta_{\max}$ is shown (bottom right, for high resolution image, see figure 4.15).

First, because the data for the reconstruction was gathered in three different measurement nights, $\langle \mathbf{S} \rangle$ is not exactly the same for all turning angles. To compensate this, we center all histograms around 0, i. e. for each angle we subtract $\langle S_\theta \rangle$ from the measured data. We then 'normalize' the histogram width by multiplying the data by $\sqrt{1250/N}$ where N is the average total atom number in the corresponding measurement night. This results in a Wigner function which is centered around $[S_y, S_z] = [0, 0]$ and where a $1/\sqrt{e}$ radius smaller $\sqrt{1250}/2$ indicates squeezing.

Next, we have to choose an appropriate bin size dS_θ for the histograms. Smaller bins provide a higher resolution in S_θ while larger bins reduce the error in $p(S_\theta)$. We find a good compromise by choosing the total number of bins to be around $\sqrt{M}$, where M is the number of measurements per turning angle.

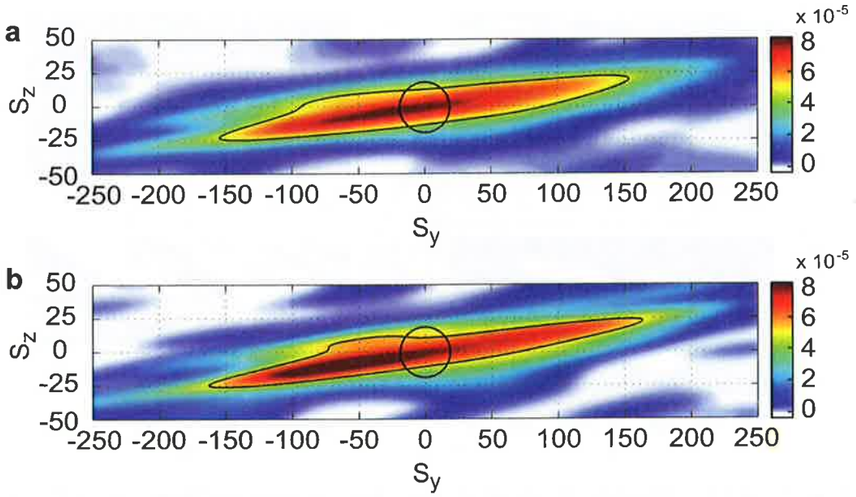

Figure 4.15: Reconstructed Wigner function using (a) the reconstruction method where each histogram bin is divided into 6 sub-bins and (b) the method where a θ-dependent $\eta_{\max}$ is used. The two contour lines indicate where the Wigner functions of our squeezed state and of an ideal coherent spin state (with the same N and with added imaging noise) have fallen to $1/\sqrt{e}$ of their maximum.

Finally, there are some technical subtleties when numerically calculating the Wigner function from our data. The integrals in equation (2.48) become discrete sums and while the values of $\theta_{\min}$, $\theta_{\max}$, $d\theta$, and dS_θ are determined by our data, the step size of the variable $d\eta$ and the summation boundaries $\eta_{\max}$ and $\eta_{\min} = -\eta_{\max}$ still have to be found. η is not independent because it is the conjugate variable of S_θ [100]. Thus, too large values for $d\eta$ will result in a periodic repetition of the Wigner function (see figure 4.14). The step size $d\eta$ should be chosen such that $d\eta \cdot S_{\max} \ll \pi$, where $S_{\max}$ is the extent of the Wigner function.

The correct summation boundaries $\eta_{\max}$ are different for each turning angle and depend on the bin size dS_θ of the corresponding histogram. While too small values artificially broaden the Wigner function along θ, interference effects occur for $\eta_{\max} \cdot dS_\theta > \pi$ (figure 4.14). In practice, this means that we cannot find an $\eta_{\max}$ which provides good enough resolution to see the squeezing along $\theta_{\min}$ and at the same time is small enough to prevent interference along $\theta \approx 90°$. There are two ways how to cope with this problem: we can decrease dS_θ in each histogram by dividing the bins into sub-bins and

determining the probabilities for each sub-bin by fitting a spline through the original histogram. We usually choose 6 sub-bins. We can then choose $\eta_{\max}$ as an effective low-pass filter, cutting off modulations of S_θ on a scale smaller than the imaging noise $\Delta S_{z,\mathrm{im}}$. This method was used in [25]. Alternatively, we execute the summation over η first and choose an appropriate $\eta_{\max}$ (and $d\eta$) for each turning angle. With this method, the low-pass filter given by $\eta_{\max}$ is dependent on the angle, but it is computationally much less demanding. In both cases, the resolution of the Wigner function is limited by dS_θ, i. e. by the atom number resolution of the imaging system.

A comparison of the two methods is shown in figure 4.15. The two contour lines indicate where the Wigner functions of our squeezed state and of an ideal coherent spin state (with the same N and with added imaging noise) have fallen to $1/\sqrt{e}$ of their maximum. Both methods reveal similar information about our squeezed state, the second method seems to bring out a little bit more detail. As expected, the spin squeezed state is squeezed along the direction $\theta_{\min}$ and anti-squeezed along the perpendicular direction. Due to losses and technical noise, it is not a minimal uncertainty state anymore; the area of the squeezed state's contour line is about 4 times that of the coherent spin state's.

Conclusion and outlook

In this thesis, I have presented experiments where we have for the first time created multi-particle entanglement on an atom chip. Our experiment uses a novel chip-based method for entanglement generation employing state-selective microwave near-field potentials. We have produced a spin squeezed state with a reduced spin noise compared to the standard quantum limit by $\Delta_n S_\theta^2 = -3.7\,\mathrm{dB}$, which is a resource that could improve an interferometric measurement by $\xi^2 = -2.5\,\mathrm{dB}$. We were able to reconstruct the Wigner function of the produced state and prove that it is at least 4-particle entangled.

Although our experiment was designed to generate entanglement between two separate BECs, using nonlinear effects, we were at first not aware that state-selective splitting of a *single* condensate could already lead to entanglement. However, when analyzing the data of our trapped atom interferometer, we found that technical noise alone seemed insufficient to explain the phase noise we were measuring. In a discussion about the original proposal, Alice Sinatra suggested that spin squeezing might occur in the current experiments and that this might be the cause of the additional noise. We only had to detect it, and we should be able to do this by simply adjusting the length of the second Ramsey pulse.

In practice, a lot of work was required before we were able to confirm the predicted squeezing and we had to learn many subtleties involved in these high-precision experiments. We kept the experimental trap but adjusted the microwave frequency to reduce the magnetic field sensitivity of the dressed states and to decrease the splitting and thus lessen influences of uncontrolled motion. We also improved the atom number resolution of our detection system and the experiment's over-all stability.

To gain a better understanding of the limitations of our method, we developed the microwave near-field imaging method and performed a detailed analysis of possible noise sources. We now have a clear idea of the next steps needed to improve the squeezing performance. First, we will exchange the current source producing B_y, isolate the experiment from mechanical vibrations, and stabilize the on-chip microwave power P_{mw} better. Probably

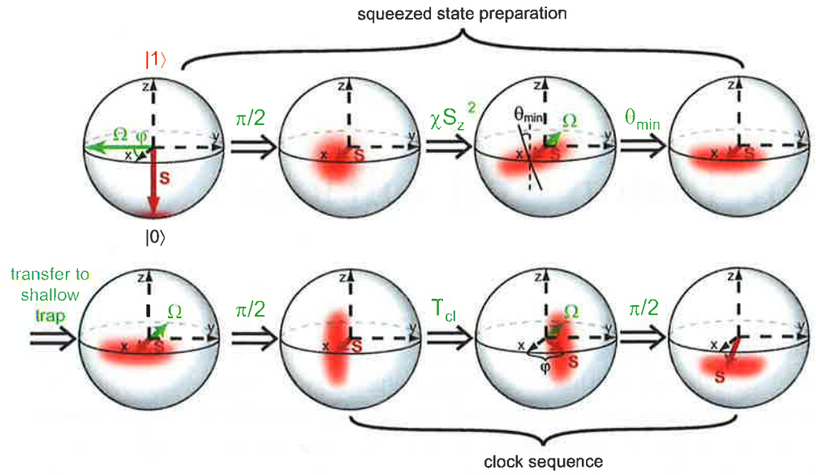

Figure 4.16: Sequence of an atomic clock using a squeezed state. The spin squeezed state is first prepared as described in this thesis and turned by θ_{min} to align the anti-squeezed axis with the equator. It is then transfered to a shallow trap to reduce phase noise during the clock interrogation time T_{cl}. The atomic clock sequence consists of two $\frac{\pi}{2}$-pulses separated in time by T_{cl}.

the most important step toward higher squeezing, however, is to shift the experimental trap to a position in the microwave near-field where no gradient along z is present. Also, to improve the squeezing as well as the reference measurement, a closer investigation of the phase noise contribution of the high frequency electronics is advisable.

While achieving larger squeezing is in itself 'only' a technical advance, the gained control over the atoms with less technical noise will be essential for the next experiments which we are planning to do with our setup.

Atomic clock beyond the SQL

A logical next experiment is to use the squeezed state in an atomic clock sequence and demonstrate the increased precision compared to using a CSS. This is technically very demanding because the state is turned such that the squeezed direction is aligned with the equator of the Bloch-sphere during the clock interrogation time T_{cl}. Thus, phase noise affects the squeezing in the clock sequence stronger by a factor $1/\sin(\theta_{\text{min}}) \approx 10$ compared to the sequence that is used to produce the squeezed state. The high sensitivity to

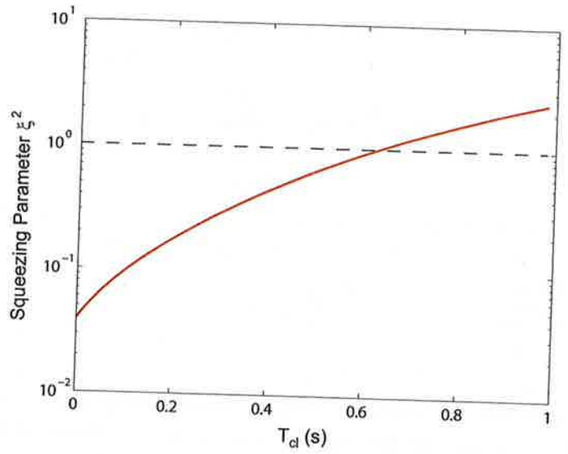

Figure 4.17: Squeezing lifetime in a clock sequence. Results of a Monte-Carlo simulation on how the squeezing evolves under particle losses and the residual nonlinearity in a shallow trap which could be used in a clock experiment. The dashed line indicates the standard quantum limit. The state remains squeezed for clock interrogation times T_{cl} of up to 0.6 s in this trap.

phase noise is the reason why in previous experiments [27, 26, 121] T_{cl} could not be increased beyond a few μs before the squeezing was lost.

Our atom-chip based setup has the advantage that we can easily transfer the squeezed state into a different trap, which is optimized for low phase noise and low losses, before applying the two $\frac{\pi}{2}$-pulses for the clock operation. Also, since no microwave near-field is applied during the clock interrogation, the main sources of technical phase noise are eliminated. The proposed sequence is shown in figure 4.16. We prepare the squeezed state as described in this thesis and turn it by θ_{min} to align the anti-squeezed direction with the equator. This makes it robust against phase noise in the subsequent transfer step. Let us for now assume that all technical fluctuations can be eliminated (corresponding to the blue curve in figure 4.9), such that the prepared state is squeezed by $\xi^2 = 4 \times 10^{-2}$.

We then transfer the atoms into a shallow trap ($f_{\text{long}} = 10\,\text{Hz}$, $f_{\text{ax}} = 50\,\text{Hz}$) with reduced atom density. Here, the atom loss rates and the sensitivity to total atom number fluctuations are greatly reduced. The residual nonlinearity in this trap is $\chi = 5 \times 10^{-5}\,\text{Hz}$, so that quantum phase spreading has a negligible effect. Phase fluctuations accumulated during the transfer

lead to a broadening of the state in the anti-squeezed direction and could at worst decrease the Ramsey contrast slightly. Note that in the experiments presented in this thesis, we are already transferring the atoms into the shallow detection trap within 30 ms and we see no difference compared to releasing the atoms directly from the experiment trap.

To start the clock, the state is rotated by applying a $\frac{\pi}{2}$-pulse, so that its squeezed axis is oriented along the equator of the Bloch sphere. After a variable clock time T_{cl}, during which the interferometer phase φ is accumulated along the squeezed direction, another $\frac{\pi}{2}$-pulse is applied to read out the clock.

Figure 4.17 shows ξ^2 as a function of T_{cl}, calculated using the Monte-Carlo method presented in 2.2.7, i. e. taking into account the residual nonlinearity and atom losses but no technical noise. The use of our squeezed state in such a trap would improve the sensitivity compared to a classical interferometer with a coherent spin state as input for T_{cl} of up to 0.6 s.

Quantum phase gate and entanglement of two BECs

The original idea behind the microwave near-field potentials was to develop a chip-based tool with which one could state-selectively manipulate and entangle atoms and then use this tool to build a quantum phase gate on an atom chip [48, 49]. The proposed gate works as follows: the two qubits are represented by two atoms in a superposition of states $|0\rangle$ and $|1\rangle$ which are trapped each in one well of a magnetic double well potential. For the gate operation, the microwave near-field is used to state selectively increase or remove the barrier separating the atoms (see figure 4.18 a). State $|0\rangle$ is shifted further out while state $|1\rangle$ starts to oscillate in the resulting single well. Only if both atoms are in the state $|1\rangle$, they collide and pick up a collisional phase shift. By tuning the trap frequency and the number of oscillations, the collisional phase can be adjusted to be π and the corresponding truth table is then that of a universal quantum gate.

An alternative scheme consists essentially of two trapped atom interferometers next to each other (figure 4.18 b). Here, the atoms collide only if the left atom is in state $|1\rangle$ and the right atom is in state $|0\rangle$.

The high accuracy of our simulations of the static traps as well as the microwave near-field has been verified in our experiments. It therefore seems relatively straight forward to implement the simulated gate potentials with our setup. However, for a gate operation as originally envisioned, single atoms instead of BECs must be used. A new chip is therefore needed, which combines a coplanar waveguide with fiber cavities developed in the group of Jakob Reichel for single atom detection and preparation [36, 71].

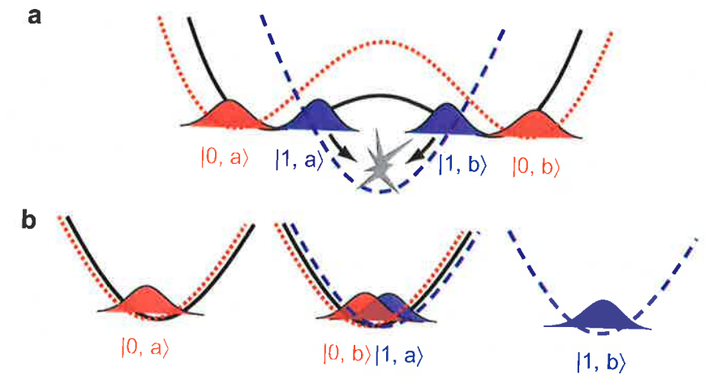

Figure 4.18: Proposed collisional phase gate. Collisional phase gate as proposed in [48] (a) and with an alternative scheme (b). The static (black) and the combined static and microwave potential (red for state $|0\rangle$, blue for state $|1\rangle$) are shown together with the qubit wave functions during the gate operation. The indices a and b label the wells from which the states originate.

With our current setup and a similar scheme, it is possible to investigate entanglement between two BECs. Although the collisional phase shift would be interesting to observe (if only as a proof-of-principle experiment for the gate operation), the mean phase shift in itself is not a signature of entanglement. However, such a signature can probably be found in the variances of combined quantities, such as $(N_1^a - N_0^b)/(N_1^a + N_0^b)$ where a and b denote the two condensates and 0 and 1 the internal states. To see the entanglement, one would thus look at the noise correlations between the spins of the two BECs.

Schrödinger cat state preparation

The experimental technique employed for the generation of spin squeezed states can also be used to generate Schrödinger cat states (see section 2.2.5 and [122]). However, for a large BEC, a separation of the two clock states for very long times would be needed (for our parameters with $N = 1250$, $\chi_{\max} = 3\,\text{Hz}$, therefore $t_{\text{rev}} = \frac{\pi}{\chi} \approx 1\,\text{s}$), and losses would unavoidably prohibit the emergence of the fragile entangled state.

For small atom numbers ($N \sim 10$) on the other hand, the atom density and thus the loss rates are greatly reduced. At the same time, χ is increased by several orders of magnitude, resulting in revival times of a few milliseconds. In principle, Schrödinger cat state preparation in small BECs seems

therefore possible with our technique. However, not only is a deterministic preparation and detection of small atom numbers needed (which could again be provided by integrated fiber cavities), but also a much better control over phase noise than for the squeezing measurements. Although technically very demanding, the successful implementation of such an experiment would certainly be a milestone in cold atom physics.

Further applications of our technique

The clock operation and the entanglement of two BECs seem to be the obvious next experiments for our setup, but there are many ideas how our technique could be used in other contexts.

A coplanar waveguide could replace the microwave horn to deliver microwave pulses for the two-photon transition. This enables a very well defined microwave field at the position of the atoms, which results in higher pulse stability over long times. Especially for a portable atomic clock on a chip [53] this would be beneficial. A possible downside could be steeper gradients across the atom cloud which would lead to inhomogeneous dephasing.

A recent proposal suggests the use of microwave radiation instead of static magnetic fields to induce a Fano-Feshbach resonance and thus tune the scattering lengths of alkali atoms [123]. The width of the resonance is proportional to the power of the microwave and for ^{87}Rb, microwave magnetic fields on the order of a few Gauss are needed to achieve practicable tuning of the scattering lengths. With our coplanar waveguide, such high microwave magnetic field strengths are easily achievable at a distance of about 10 μm from the chip. In [123], one-photon microwave transitions are investigated and the technique is thus not one-to-one applicable to our state pair. However, according to the author of the proposal [124], the theory can probably be modified to include the two-photon transition. This would open up the possibility to tune the inter-state scattering length a_{01} of our clock states for which no 'classical' Feshbach resonance is known.

The techniques developed in our group have potential applications not only in science but also in industry. A trapped atom interferometer, using microwave near-fields for internal-state labeling of the interferometer arms, is investigated for the implementation in commercial atom chip based gyroscopes [125]. Our microwave field imaging method could e. g. be employed to characterize the microwave field distribution in the interaction region of state of the art fountain clocks. Since our method can be extended to frequencies used in communication technologies, it could also help to characterize prototypes of monolithic microwave integrated circuits (MMICs), which are a key ingredient in today's communication devices.

In conclusion, the experiments presented in this thesis enable new exciting research in the fields of quantum metrology and quantum computation. Cold atom physics is indeed past the stage of purely fundamental research: entanglement generation on atom chips opens a path to real-life applications, harvesting the mysteries of quantum mechanics.

Appendix A

Fundamental constants and useful ^{87}Rb data

Fundamental constants

Planck's constant	h $\hbar = h/2\pi$	$6.626\ 068\ 96(33) \times 10^{-34}$ J s $1.054\ 571\ 628(53) \times 10^{-34}$ J s
Bohr magneton	μ_B	$9.274\ 009\ 15(23) \times 10^{-24}$ J/T $h \cdot 1.399\ 624\ 604(35)$ MHz/G
Speed of light	c	$2.997\ 924\ 58 \times 10^{8}$ m/s (exact)
Permeability of vacuum	μ_0	$4\pi \times 10^{-7}$ N/A^2 (exact)
Permittivity of vacuum	$\varepsilon_0 = (\mu_0 c^2)^{-1}$	$8.854\ 187\ 817\ldots \times 10^{-12}$ F/m
Bohr radius	a_0	$0.529\ 177\ 208\ 59(36) \times 10^{-10}$ m

General ^{87}Rb properties

Atomic mass	m	$1.443\ 160\ 648(72) \times 10^{-25}$ kg
Nuclear spin	I	3/2
Relative natural abundance		27.83(2)%

D_2 transition ($5^2S_{1/2} \leftrightarrow 5^2P_{3/2}$) optical properties

Wavelength (vacuum)	λ	780.241 209 686(13) nm
Natural line width	Γ	$38.117(11) \times 10^6\ s^{-1}$ $2\pi \cdot 6.066\ 6(18)$ MHz
Saturation intensity $\lvert F = 2, m_F = \pm 2\rangle \leftrightarrow \lvert F' = 3, m_F' = \pm 3\rangle$ cycling transition ($\sigma^{\pm}$-polarized light)	I_s	1.669 33(35) mW/cm^2

$5^2S_{1/2}$ ground state properties

Zero-field hyperfine splitting	E_{hfs} $= 2A_{\text{hfs}}$	$h \cdot 6.834\ 682\ 610\ 904\ 290(90)$ GHz
Electron spin g-factor	g_J	2.002 331 13(20)
Nuclear spin g-factor	g_I	−0.000 995 141 4(10)
Static polarizability	α_0	$h \cdot 0.0794(16)$ Hz/(V/cm)^2
S-wave scattering lengths		values from [86]
$\|1,-1\rangle - \|1,-1\rangle$	a_{00}	$100.40\,a_0 = 5.3129$ nm
$\|2,1\rangle - \|1,-1\rangle$	a_{10}	$97.66\,a_0 = 5.1679$ nm
$\|2,1\rangle - \|2,1\rangle$	a_{11}	$95.00\,a_0 = 5.0272$ nm

All values taken from [50] if no other source is specified.

Appendix B

Angular momentum matrix elements

In the Hamiltonian describing the coupling of the atom to a microwave field (section 1.1.3), we encounter the matrix elements

$$\langle 2, m_2|\boldsymbol{\epsilon}\cdot\mathbf{J}|1,m_1\rangle \equiv \langle F'=2, m_F{}'=m_2|\boldsymbol{\epsilon}\cdot\mathbf{J}|F=1,m_F=m_1\rangle, \tag{B.1}$$

where $\boldsymbol{\epsilon} = (\epsilon_x, \epsilon_y, \epsilon_z)$ is a unit polarization vector, whose components may be complex. Using $J_x = \frac{1}{2}(J_+ + J_-)$ and $J_y = -\frac{i}{2}(J_+ - J_-)$, we express $\boldsymbol{\epsilon}\cdot\mathbf{J}$ as

$$\boldsymbol{\epsilon}\cdot\mathbf{J} = \epsilon_x J_x + \epsilon_y J_y + \epsilon_z J_z = \tfrac{1}{2}(\epsilon_x - i\epsilon_y)J_+ + \tfrac{1}{2}(\epsilon_x + i\epsilon_y)J_- + \epsilon_z J_z. \tag{B.2}$$

The matrix elements $\langle 2, m_2|J_q|1,m_1\rangle$, $(q = +,-,z)$ can be calculated as described in [49]. The result is (listing only the non-vanishing elements):

$$\begin{aligned}\langle 2,2|J_+|1,1\rangle &= \sqrt{\tfrac{3}{4}}\\ \langle 2,1|J_+|1,0\rangle &= \sqrt{\tfrac{3}{8}}\\ \langle 2,0|J_+|1,-1\rangle &= \sqrt{\tfrac{1}{8}}\end{aligned} \tag{B.3}$$

$$\begin{aligned}\langle 2,0|J_-|1,1\rangle &= -\sqrt{\tfrac{1}{8}}\\ \langle 2,-1|J_-|1,0\rangle &= -\sqrt{\tfrac{3}{8}}\\ \langle 2,-2|J_-|1,-1\rangle &= -\sqrt{\tfrac{3}{4}}\end{aligned} \tag{B.4}$$

$$\begin{aligned}\langle 2,1|J_z|1,1\rangle &= -\sqrt{\tfrac{3}{16}} \\ \langle 2,0|J_z|1,0\rangle &= -\sqrt{\tfrac{1}{4}} \\ \langle 2,-1|J_z|1,-1\rangle &= -\sqrt{\tfrac{3}{16}}\end{aligned} \tag{B.5}$$

Appendix C

Data analysis recipe

In order to achieve the highest possible data quality, we process the recorded raw-data before calculating $\langle S_\theta \rangle$ and ΔS_θ^2. This is to make sure that the detected atom number is accurate and that minimal additional noise due to technical effects distort the results. The processing involves many steps, which are described throughout the main text. Here, I give a compact overview in the form of a recipe:

- Calibrate the imaging hardware. Assuming the camera's quantum efficiency and gain are known from the manufacturer's spec sheet, determine the objective resolution and magnification with the help of a USAF calibration target (see figure 3.16). The resolution should be higher than the diameter of the imaged atom clouds. Do this whenever you change the camera objective. Focus the camera on small BEC clouds.

- Measure the effective scattering cross section σ_{eff} by varying the imaging intensity I_0 and adjusting σ_{eff} such that the detected atom number is independent of I_0 (see figure 3.12). Do this whenever you change the polarization or tilt of the imaging beam or change the position where the atoms are imaged (by changing the last trap position or the TOF). From now on, use this effective scattering cross section in the image analysis.

- Determine the relative detectivity between states $|0\rangle$ and $|1\rangle$ by recording Rabi or Ramsey oscillations (see figure 3.14). Assume the detection efficiency for $|0\rangle$ is 100 % and from the sinusoidal fits deduce the detection efficiency $p_d < 1$ of state $|1\rangle$. Do this daily. The result should be the same from day to day within 10 %. From now on, multiply N_1 by $1/p_d$ to compensate the detection efficiency difference.

- Calibrate the actual atom number using quantum projection noise. For different N, measure ΔS_z^2 after a $\frac{\pi}{2}$-pulse (analyze the data using σ_{eff} and p_d). Plotting ΔS_z^2 versus N and fitting it with a straight line should result in a slope s of $1/4$ (see figure 3.17). In practice, we obtain a slope which differs by $\sim 10\,\%$ from the ideal result. This confirms that the atom number calibration obtained from σ_{eff} is already a very good estimate. If the slope is too small, the real atom number is higher than the detected one by a factor $1/(4s)$ and vice versa. Do this whenever you determine σ_{eff}. From now on, correct N_0 and N_1 accordingly.

So far, all corrections were made to achieve accurate atom numbers $N_0 = N_0^{\text{raw}}/(4s)$ and $N_1 = N_1^{\text{raw}}/(4s \cdot p_d)$, where $N_{,}^{\text{raw}}$ are the atom numbers determined using σ_{eff}.

- Now, eliminate the influence of shot-to-shot fluctuations in the total atom number by calculating (see section 3.7.3)

$$N_{j,\text{corr}} = \frac{N_j}{N_0 + N_1}\left(\overline{N}_0 + \overline{N}_1\right). \tag{C.1}$$

- Discard experimental runs where the total atom number differs significantly from the target atom number. We typically use a window of ± 150 atoms. Check that the window is small enough so that the exact choice of its size does not influence the results.

- Calculate $S_{z,\text{corr}} = (N_{1,\text{corr}} - N_{0,\text{corr}})/2$. If $S_{z,\text{corr}}$ shows a slow drift over long times, this drift must be of technical nature and can be eliminated by subtracting a filtered data set, using a second order Savitzky-Golay filter [118] over many shots.

- Subtract the imaging noise from the relative atom number noise, as described in section 3.7.3, by calculating

$$\Delta S_z^2 = \Delta S_{z,\text{corr}}^2 - \Delta S_{z,\text{im}}^2. \tag{C.2}$$

Bibliography

[1] A. H. Wilson, *The theory of electronic semi-conductors*, Proceedings of the Royal Society of London **133**, 458 (1931).

[2] A. H. Wilson, *The theory of metals. I*, Proceedings of the Royal Society of London **138**, 594 (1931).

[3] J. Bardeen, W. H. Brattain, and W. B. Shockley, in *Nobel lectures, physics 1942-1962*, Amsterdam, 1964, Elsevier publishing company.

[4] M. H. Anderson, J. R. Ensher, M. R. Matthews, C. E. Wieman, and E. A. Cornell, *Observation of Bose-Einstein Condensation in a Dilute Atomic Vapor*, Science **269**, 198 (1995).

[5] K. B. Davis, M.-O. Mewes, M. R. Andrews, N. J. van Druten, D. S. Durfee, D. M. Kurn, and W. Ketterle, *Bose-Einstein condensation in a gas of sodium atoms*, Phys. Rev. Lett. **75**, 3969 (1995).

[6] C. C. Bradley, C. A. Sackett, J. J. Tollet, and R. G. Hulet, *Evidence of Bose-Einstein condensation in an atomic gas with attractive interactions*, Phys. Rev. Lett. **75**, 1687 (1995).

[7] M. R. Andrews, C. G. Townsend, H.-J. Miesner, D. S. Durfee, D. M. Kurn, and W. Ketterle, *Oservation of the interference between two Bose-Einstein condensates*, Science **275**, 637 (1997).

[8] M. R. Matthews, P. B. Anderson, P. C. Haljan, D. S. Hall, C. E. Wieman, and E. A. Cornell, *Vortices in a Bose-Einstein Condensate*, Phys. Rev. Lett. **83**, 2498 (1997).

[9] V. Giovannetti, S. Lloyd, and L. Maccone, *Quantum-enhanced measurements: beating the Standard Quantum Limit*, Science **306**, 1330 (2004).

[10] V. Giovannetti, S. Lloyd, and L. Maccone, *Quantum metrology*, Phys. Rev. Lett. **96**, 010401 (2006).

[11] W. M. Itano, J. C. Bergquist, J. J. Bollinger, J. M. Gilligan, D. J. Heinzen, F. L. Moore, M. G. Raizen, and D. J. Wineland, *Quantum projection noise: Population fluctuations in two-level systems*, Phys. Rev. A **47**, 3354 (1993).

[12] G. Santarelli, P. Laurent, P. Lemonde, A. Clairon, A. G. Mann, S. Chang, A. N.Luiten, and C. Salomon, *Quantum projection noise in an atomic fountain: a high stability cesium frequency standard*, Phys. Rev. Lett. **82**, 4619 (1999).

[13] M. Kitagawa and M. Ueda, *Squeezed spin states*, Phys. Rev. A **47**, 5138 (1993).

[14] M. O. Scully and M. S. Zubairy, *Quantum Optics*, Cambridge University Press, Cambridge, U.K., 1997.

[15] D. J. Wineland, J. J. Bollinger, W. M. Itano, and D. J. Heinzen, *Squeezed atomic states and projection noise in spectroscopy*, Phys. Rev. A **50**, 67 (1994).

[16] A. Sørensen, L.-M. Duan, J. I. Cirac, and P. Zoller, *Many-particle entanglement with Bose-Einstein condensates*, Nature **409**, 63 (2001).

[17] J. Hald, J. L. Sørensen, C. Schori, and E. S. Polzik, *Spin squeezed atoms: a macroscopic entangled ensemble created by light*, Phys. Rev. Lett. **83**, 1319 (1999).

[18] A. Kuzmich, L. Mandel, and N. P. Bigelow, *Generation of Spin Squeezing via Continuous Quantum Nondemolition Measurement*, Phys. Rev. Lett. **85**, 1594 (2000).

[19] B. Julsgaard, A. Kozhekin, and E. S. Polzik, *Experimental long-lived entanglement of two macroscopic objects*, Nature **413**, 400 (2001).

[20] C. Orzel, A. K. Tuchman, M. L. Fenselau, M. Yasuda, and M. A. Kasevich, *Squeezed states in a Bose-Einstein condensate*, Science **291**, 2386 (2001).

[21] F. Gerbier, S. Fölling, A. Widera, O. Mandel, and I. Bloch, *Probing number squeezing of ultracold atoms across the superfluid-Mott insulator transition*, Phys. Rev. Lett. **96** (2006).

[22] T. Fernholz, H. Krauter, K. Jensen, J. F. Sherson, A. Sørensen, and E. S. Polzik, *Spin squeezing of atomic ensembles via nuclear-electronic spin entanglement*, Phys. Rev. Lett. **101** (2008).

[23] J. Appel, P. J. Windpassinger, D. Oblak, U. B. Hoff, N. Kjærgaard, and E. S. Polzik, *Mesoscopic atomic entanglement for precision measurements beyond the standard quantum limit*, Proceedings of the National Academy of Sciences **106**, 10960 (2009).

[24] M. H. Schleier-Smith, I. D. Leroux, and V. Vuletić, *States of an ensemble of two-level atoms with reduced quantum uncertainty*, Phys. Rev. Lett. **104**, 073604 (2010).

[25] M. F. Riedel, P. Böhi, Y. Li, T. W. Hänsch, A. Sinatra, and P. Treutlein, *Atom-chip-based generation of multi-particle entanglement for quantum metrology*, Nature **464**, 1170 (2010).

[26] C. Gross, T. Zibold, E. Nicklas, J. Estève, and M. K. Oberthaler, *Nonlinear atom interferometer surpasses classical precision limit*, Nature **464**, 1165 (2010).

[27] I. D. Leroux, M. H. Schleier-Smith, and V. Vuletić, *Orientation-dependent entanglement lifetime in a squeezd atomic clock*, Phys. Rev. Lett. **104**, 250801 (2010).

[28] J. Reichel, W. Hänsel, P. Hommelhoff, and T. W. Hänsch, *Applications of integrated magnetic microtraps*, Appl. Phys. B **72**, 81 (2001).

[29] R. Folman, P. Krüger, J. Schmiedmayer, J. Denschlag, and C. Henkel, *Microscopic atom optics: from wires to an atom chip*, Adv. At. Mol. Opt. Phys. **48**, 263 (2002).

[30] J. Reichel, *Microchip traps and Bose-Einstein condensation*, Appl. Phys. B **74**, 469 (2002).

[31] J. Fortágh and C. Zimmermann, *Magnetic microtraps for ultracold atoms*, Rev. Mod. Phys. **79**, 235 (2007).

[32] A. Vogel, M. Schmidt, K. Sengstock, K. Bongs, W. Lewoczko, T. Schuldt, A. Peters, T. van Zoest, W. Ertmer, E. Rasel, T. Steinmetz, J. Reichel, T. Könemann, W. Brinkmann, W. Göklü, C. Lämmerzahl, H. J. Dittus, G. Nandi, W. P. Schleich, and R. Walser, *Bose-Einstein condensates in microgravity*, Appl. Phys. B **84**, 663 (2006).

[33] D. M. Farkas, K. M. Hudek, E. A. Salim, S. R. Segal, M. B. Squires, and D. Z. Anderson, *A compact, transportable, microchip-based system for high repetition rate production of Bose-Einstein condensates*, Appl. Phys. Lett. **96**, 093102 (2010).

[34] www.coldquanta.com.

[35] S. Hofferberth, I. Lesanovsky, B. Fischer, T. Schumm, and J. Schmiedmayer, *Non-equilibrium coherence dynamics in one-dimensional Bose gases*, Nature **449**, 324 (2007).

[36] Y. Colombe, T. Steinmetz, G. Dubois, F. Linke, D. Hunger, and J. Reichel, *Strong atom-field coupling for Bose-Einstein condensates in an optical cavity on a chip*, Nature **450**, 272 (2007).

[37] Y. Lin, I. Teper, C. Chin, and V. Vuletić, *Impact of the Casimir-Polder potential and Johnson noise on Bose-Einstein condensate stability near surfaces*, Phys. Rev. Lett. **92**, 050404 (2004).

[38] S. Aigner, L. Pietra, Y. Japha, O. Entin-Wohlman, T. David, R. Salem, R. Folman, and J. Schmiedmayer, *Long-range order in electronic transport through disordered metal films*, Science **319**, 1226 (2008).

[39] D. Hunger, S. Camerer, T. W. Hänsch, D. König, P. Kotthaus, J. Reichel, and P. Treutlein, *Resonant coupling of a Bose-Einstein condensate to a micromechanical oscillator*, Phys. Rev. Lett. **104**, 143002 (2010).

[40] P. Treutlein, P. Hommelhoff, T. Steinmetz, T. W. Hänsch, and J. Reichel, *Coherence in microchip traps*, Phys. Rev. Lett. **92**, 203005 (2004).

[41] C. Deutsch, F. Ramirez, C. Lacroûte, F. Reinhard, T. Schneider, J.-N. Fuchs, F. Piéchon, F. Laloë, J. Reichel, and P. Rosenbusch, *Spin self-rephasing and very long coherence times in a trapped atomic ensemble*, Phys. Rev. Lett. **105**, 020401 (2010).

[42] Y.-J. Wang, D. Z. Anderson, V. M. Bright, E. A. Cornell, Q. Diot, T. Kishimoto, M. Prentiss, R. A. Saravanan, S. R. Segal, and S. Wu, *Atom Michelson interferometer on a chip using a Bose-Einstein condensate*, Phys. Rev. Lett. **94**, 090405 (2005).

[43] T. Schumm, S. Hofferberth, L. M. Andersson, S. Wildermuth, S. Groth, I. Bar-Joseph, J. Schmiedmayer, and P. Krüger, *Matter-wave interferometry in a double well on an atom chip*, Nat. Phys. **1**, 57 (2005).

[44] P. Böhi, M. F. Riedel, J. Hoffrogge, J. Reichel, T. W. Hänsch, and P. Treutlein, *Coherent manipulation of Bose-Einstein condensates with state-dependent microwave potentials on an atom chip*, Nat. Phys. **5**, 592 (2009).

[45] P. Böhi, *Coherent manipulation of ultracold atoms with microwave near-fields*, PhD thesis, Ludwig-Maximilians-Universität München and Max-Planck-Institut für Quantenoptik, 2010.

[46] A. Sørensen and K. Mølmer, *Entanglement and extreme spin squeezing*, Phys. Rev. Lett. **86**, 4431 (2001).

[47] Y. Li, P. Treutlein, J. Reichel, and A. Sinatra, *Spin squeezing in a bimodal condensate: spatial dynamics and particle losses*, Eur. Phys. J. B **68**, 365 (2009).

[48] P. Treutlein, T. W. Hänsch, J. Reichel, A. Negretti, M. A. Cirone, and T. Calarco, *Microwave potentials and optimal control for robust quantum gates on an atom chip*, Phys. Rev. A **74**, 022312 (2006).

[49] P. Treutlein, *Coherent manipulation of ultracold atoms on atom chips*, PhD thesis, Ludwig-Maximilians-Universität München and Max-Planck-Institut für Quantenoptik, 2008, published as MPQ report 321.

[50] D. A. Steck, *Rubidium 87 D Line Data*, http://steck.us/alkalidata/ , version 2.1.2 (2009).

[51] G. Breit and I. I. Rabi, *Measurement of Nuclear Spin*, Phys. Rev. **38**, 2082 (1931).

[52] D. M. Harber, H. J. Lewandowski, J. M. McGuirk, and E. A. Cornell, *Effect of cold collisions on spin coherence and resonance shifts in a magnetically trapped ultracold gas*, Phys. Rev. A **66**, 053616 (2002).

[53] P. Rosenbusch, *Magnetically trapped atoms for compact atomic clocks*, Appl. Phys. B **95**, 227 (2009).

[54] N. V. Vitanov, T. Halfmann, B. W. Shore, and K. Bergmann, *Laser-induced population transfer by adiabatic passage techniques*, Appl. Phys. B **52**, 763 (2001).

[55] T. Gentile, B. Hughey, D. Kleppner, and T. Ducas, *Experimental study of one- and two-photon Rabi oscillations*, Phys. Rev. A **40**, 5103 (1989).

[56] H. J. Metcalf and P. van der Straten, *Cooling and trapping of neutral atoms*, Phys. Rep. **244**, 203 (1994).

[57] C. S. Adams and E. Riis, *Laser cooling and trapping of neutral atoms*, Prog. Quant. Electr. **21**, 1 (1997).

[58] C. D. J. Sinclair, E. A. Curtis, I. Llorente Garcia, J. A. Retter, B. V. Hall, S. Eriksson, B. E. Sauer, and E. A. Hinds, *Bose-Einstein condensation on a permanent-magnet atom chip*, Phys. Rev. A **72**, 031603 (2005).

[59] B. V. Hall, S. Whitlock, F. Scharnberg, P. Hannaford, and A. Sidorov, *A permanent magnetic film atom chip for Bose-Einstein condensation*, J. Phys. B: At. Mol. Opt. Phys. **39**, 27 (2006).

[60] S. Whitlock, R. Gerritsma, T. Fernholz, and R. J. C. Spreeuw, *Two-dimensional array of microtraps with atomic shift register on a chip*, New J. Phys. **11**, 023021 (2009).

[61] T. Mukai, C. Hufnagel, A. Kasper, T. Meno, A. Tsukada, K. Semba, and F. Shimizu, *Persistent supercurrent atom chip*, Phys. Rev. Lett. **98**, 260407 (2007).

[62] J. J. P. van Es, P. Wicke, A. H. van Amerogen, C. Rétif, S. Whitlock, and N. J. Druten, *Box traps on an atom chip for one-dimensional quantum gases*, J. Phys. B: At. Mol. Opt. Phys. **43**, 155002 (2010).

[63] S. Wildermuth, S. Hofferberth, I. Lesanovsky, S. Groth, P. Krüger, J. Schmiedmayer, and I. Bar-Joseph, *Sensing electric and magnetic fields with Bose-Einstein condensates*, Appl. Phys. Lett. **88**, 264103 (2006).

[64] P. Böhi, M. F. Riedel, T. W. Hänsch, and P. Treutlein, *Imaging of microwave fields using ultracold atoms*, Appl. Phys. Lett. **97**, 051101 (2010).

[65] J. Fortágh, H. Ott, S. Kraft, A. Günther, and C. Zimmermann, *Surface effects in magnetic microtraps*, Phys. Rev. A **66**, 041604 (2002).

[66] Y. Shin, C. Sanner, G.-B. Jo, T. A. Pasquini, M. Saba, W. Ketterle, D. E. Pritchard, M. Vengalattore, and M. Prentiss, *Interference of Bose-Einstein condensates split with an atom chip*, Phys. Rev. A **72**, 021604 (2005).

[67] W. Hänsel, J. Reichel, P. Hommelhoff, and T. W. Hänsch, *Magnetic conveyor belt for transporting and merging trapped atom clouds*, Phys. Rev. Lett. **86**, 608 (2001).

[68] P. Hommelhoff, W. Hänsel, T. Steinmetz, T. W. Hänsch, and J. Reichel, *Transporting, splitting and merging of atomic ensembles in a chip trap*, New J. Phys. **7**, 3 (2005).

[69] D. Cassettari, B. Hessmo, R. Folman, T. Maier, and J. Schmiedmayer, *Beam splitter for guided atoms*, Phys. Rev. Lett. **85**, 5483 (2000).

[70] K. Maussang, G. Edward, T. Schneider, P. Treutlein, Y. Li, A. Sinatra, R. Long, J. Estève, and J. Reichel, *Enhanced and reduced atom number fluctuations in a BEC splitter*, Phys. Rev. Lett. **105**, 080403 (2010).

[71] R. Gehr, J. Volz, G. Dubois, T. Steinmetz, Y. Colombe, B. L. Lev, R. Long, J. Estève, and J. Reichel, *Cavity-based single atom preparation and high-fidelity hyperfine state readout*, Phys. Rev. Lett. **104** (2010).

[72] W. Hänsel, *Magnetische Mikrofallen für Rubidiumatome*, PhD thesis, Ludwig-Maximilians-Universität München and Max-Planck-Institut für Quantenoptik, 2001, published as MPQ report 263.

[73] D. E. Pritchard, *Cooling neutral atoms in a magnetic trap for precision spectroscopy*, Phys. Rev. Lett. **51**, 1336 (1983).

[74] O. Mandel, M. Greiner, A. Widera, T. Rom, T. W. Hänsch, and I. Bloch, *Controlled collisions for multiparticle entanglement of optically trapped atoms*, Nature **425**, 937 (2003).

[75] C. C. Agosta, I. F. Silvera, H. T. C. Stoof, and B. J. Verhaar, *Trapping of neutral atoms with resonant microwave radiation*, Phys. Rev. Lett. **62**, 2361 (1989).

[76] R. J. C. Spreeuw, C. Gerz, L. S. Goldner, W. D. Phillips, S. L. Rolston, C. I. Westbrook, M. W. Reynolds, and I. F. Silvera, *Demonstration of neutral atom trapping with microwaves*, Phys. Rev. Lett. **72**, 3162 (1994).

[77] S. Hofferberth, I. Lesanovsky, B. Fischer, J. Verdu, and J. Schmiedmayer, *Radiofrequency-dressed-state potentials for neutral atoms*, Nat. Phys. **2**, 710 (2006).

[78] A. Einstein, *Quantentheorie des einatomigen idealen Gases. Zweite Abhandlung*, Sitzber. Kgl. Preuss. Akad. Wiss. , 1925:3 (1925).

[79] A. J. Dalfovo, S. Giorgini, L. P. Pitaevskii, and S. Stringari, *Theory of Bose-Einstein condensation in trapped gases*, Rev. Mod. Phys. **71**, 463 (1999).

[80] W. Ketterle, D. S. Durfee, and D. M. Stamper-Kurn, *Making, probing and understanding Bose-Einstein condensates*, in *Bose-Einstein*

condensation in atomic gases, Proceedings of the International School of Physics "Enrico Fermi", Course CXL, edited by M. Inguscio, S. Stringari, and C. E. Wieman, pages 67–176, Amsterdam, 1999, IOS Press.

[81] A. J. Leggett, *Bose-Einstein condensation in the alkali gases: some fundamental concepts*, Rev. Mod. Phys. **73**, 307 (2001).

[82] C. J. Pethick and H. Smith, *Bose-Einstein condensation in dilute gases*, Cambridge University Press, Cambridge, 2002.

[83] W. Ketterle and N. J. van Druten, *Bose-Einstein condensation of a finite number of particles trapped in one or three dimensions*, Phys. Rev. A **54**, 656 (1996).

[84] D. S. Petrov, G. V. Shlyapnikov, and J. T. M. Walraven, *Regimes of quantum degeneracy in trapped 1D Gases*, Phys. Rev. Lett. **85**, 3745 (2000).

[85] A. Muñoz Mateo and V. Delgado, *Ground-state properties of trapped Bose-Einstein condensates: extension of the Thomas-Fermi approximation*, Phys. Rev. A **75**, 063610 (2007).

[86] K. M. Mertes, J. W. Merrill, R. Carretero-González, D. J. Frantzeskakis, P. G. Kevrekidis, and D. S. Hall, *Nonequilibrium dynamics and superfluid ring excitations in binary Bose-Einstein condensates*, Phys. Rev. Lett. **99**, 190402 (2007).

[87] D. S. Hall, M. R. Matthews, J. R. Ensher, C. E. Wieman, and E. A. Cornell, *Dynamics of component separation in a binary mixture of Bose-Einstein condensates*, Phys. Rev. Lett. **81**, 1539 (1998).

[88] D. M. Brink and C. V. Sukumar, *Majorana spin-flip transitions in a magnetic trap*, Phys. Rev. A **74**, 035401 (2006).

[89] E. Majorana, *Atomi orientati in campo magnetico variabile*, Nuovo Cimento **9**, 43 (1932).

[90] E. A. Burt, R. W. Ghrist, C. J. Myatt, M. J. Holland, E. A. Cornell, and C. E. Wieman, *Coherence, correlations, and collisions: what one learns about Bose-Einstein condensates from their decay*, Phys. Rev. Lett. **79**, 337 (1997).

[91] A. D. Cronin, J. Schmiedmayer, and D. E. Pritchard, *Optics and interferometry with atoms and molecules*, Rev. Mod. Phys. **81**, 1051 (2009).

[92] N. F. Ramsey, *Molecular Beams*, Clarendon Press, Oxford, 1956.

[93] M. Lewenstein and L. You, *Quantum phase diffusion of a Bose-Einstein condensate*, Phys. Rev. Lett. **77**, 3489 (1996).

[94] Y. Li, Y. Castin, and A. Sinatra, *Optimum spin squeezing in Bose-Einstein condensates with particle losses*, Phys. Rev. Lett. **100**, 210401 (2008).

[95] K. Mølmer, Y. Castin, and J. Dalibard, *Monte Carlo wave-function method in quantum optics*, J. Opt. Soc. Am. B **10**, 524 (1993).

[96] A. Sinatra, Y. Castin, and E. Witkowska, *Nondiffusive phase spreading of a Bose-Einstein condensate at finite temperature*, Phys. Rev. A **75**, 033616 (2007).

[97] Y. Castin and J. Dalibard, *Relative phase of two Bose-Einstein condensates*, Phys. Rev. A **55**, 4330 (1997).

[98] E. Wigner, *On the quantum correction for thermodynamic equilibrium*, Phys. Rev. **40**, 749 (1932).

[99] W. P. Schleich, *Quantum optics in phase space*, Wiley-VCH, Berlin, 2001.

[100] K. Vogel and H. Risken, *Determination of quasiprobability distributions in terms of probability distributions for the rotated quadrature phase*, Phys. Rev. A **40**, 2847 (1989).

[101] J. Radon, *Über die Bestimmung von Funktionen durch ihre Integralwerte längs gewisser Mannigfaltigkeiten*, Berichte Sächsische Akademie der Wissenschaften **29**, 262 (1917).

[102] G. Breitenbach, S. Schiller, and J. Mlynek, *Measurement of the quantum states of squeezed light*, Nature **387**, 471 (1997).

[103] J. Dowling, G. Agarwal, and W. Schleich, *Wigner distribution of a general angular-momentum state: applications to a collection of two-level atoms*, Phys. Rev. A **49**, 4101 (1994).

[104] U. Leonhardt, *Quantum-state tomography and discrete Wigner function*, Phys. Rev. Lett. **74**, 4101 (1995).

[105] B. Frieden and B. Soffer, *Lagrangians of physics and the game of Fisher-information transfer*, Phys. Rev. E **52**, 2274 (1995).

[106] L. Pezzé and A. Smerzi, *Entanglement, nonlinear dynamics, and the Heisenberg limit*, Phys. Rev. Lett. **102**, 100401 (2009).

[107] J. Hoffrogge, *Mikrowellenpotentiale auf Atomchips*, Diploma thesis, Ludwig-Maximilians-Universität München, 2008.

[108] L. Ricci, M. Weidemüller, T. Esslinger, A. Hemmerich, C. Zimmerman, V. Vuletic, W. König, and T. W. Hänsch, *A compact grating-stabilized diode laser system for atomic physics*, Optics Communications **117**, 541 (1994).

[109] W. Demtröder, *Laserspektroskopie*, Springer, Heidelberg, 1991.

[110] J. Reichel, W. Hänsel, and T. W. Hänsch, *Atomic micromanipulation with magnetic surface traps*, Phys. Rev. Lett. **83**, 3398 (1999).

[111] W. Demtröder, *Experimentalphysik*, volume 2, Springer, Heidelberg, 2nd edition, 2002.

[112] G. Reinaudi, T. Lahaye, Z. Wang, and D. Guéry-Odelin, *Strong saturation absorption imaging of dense clouds of ultracold atoms*, Opt. Lett. **32**, 3143 (2007).

[113] M. A. Joffe, W. Ketterle, A. Martina, and D. E. Pritchard, *Transverse cooling and deflection of an atomic beam inside a Zeeman slower*, J. Opt. Soc. Am. B **10**, 2257 (1993).

[114] M. R. Matthews, D. S. Hall, D. S. Jin, J. R. Ensher, C. E. Wieman, E. A. Cornell, F. Dalfovo, C. Minniti, and S. Stringari, *Dynamical response of a Bose-Einstein condensate to a discontinuous change in internal state*, Phys. Rev. Lett. **81**, 243 (1998).

[115] C. Rose and M. D. Smith, *Mathematical statistics with Mathematica*, Springer, New York, 2002.

[116] F. Renzoni, S. Cartaleva, G. Alzetta, and E. Arimondo, *Enhanced absorption Hanle effect in the connfguration of crossed laser beam and magnetic field*, Phys. Rev. A **63**, 065401 (2001).

[117] Y. Li, *Spin squeezing in Bose-Einstein Condensates*, PhD thesis, Université Pierre et Marie Curie, 2010.

[118] A. Savitzky and M. Golay, *Smoothing and differentiation of data by simplified least squares procedures*, Analytical Chemistry **36**, 1627 (1964).

[119] A. S. P. Hyllus, A. Pezzé, *Entanglement and sensitivity in precision measurements with states of a fluctuating number of particles*, arXiv:1003.0649 (2010).

[120] D. Ham, W. Andress, and D. Ricketts, *Phase noise in oscillators*, International Workshop on SiP/SoC Integration of MEMS and Passive Components with RF-ICs, available at http://www.usl.chiba-u.ac.jp/ ken/Symp2004/PDF/1C3.pdf (2004).

[121] A. Louchet-Chauvet, J. Appel, J. J. Renema, D. Oblack, N. Kjaergaard, and E. S. Polzik, *Entanglement-assisted atomic clock beyond the projection noise limit*, New Journal of Physics **12**, 065032 (2010).

[122] A. Micheli, D. Jaksch, C. I. Cirac, and P. Zoller, *Many-particle entanglement in two-component Bose-Einstein condensates*, Phys. Rev. A **67**, 013607 (2003).

[123] D. Papoular, G. Shlyapnikow, and J. Dalibard, *Microwave-induced Fano-Feshbach resonances*, Phys. Rev. A **81**, 041603 (2010).

[124] private communication with David Papoular, 2010.

[125] www.trt.thalesgroup.com/cats/.

Den Mitgliedern der Treutlein-Gruppe, die die Experimente in der Schweiz weiterführen werden, bin ich verbunden und freue mich auf eine gute Zusammenarbeit mit Caspar Ockeloen, Roman Schmied, Andreas Jöckel und Maria Korppi.

Herzlichst danke ich all meinen Freunden, die meine Zeit in München zu einer großartigen Erfahrung gemacht haben, allen voran meiner lieben Freundin Frauke Schäfer.

Beenden möchte ich diese Arbeit, wie ich sie angefangen habe. Meinen Eltern sage ich großen Dank. Ihr wart jederzeit für mich da, habt mich immer verstanden und in allem unterstützt, was ich in meinem bisherigen Leben angefasst habe.